

NON-RECIPROCAL TRANSMISSION AND NON-HERMITIAN QUANTUM SENSING USING DEFECTIVE OPERATORS

A Thesis Submitted

in Partial Fulfilment of the Requirements

for the Degree of

DOCTOR OF PHILOSOPHY

by

Chetan Waghela

(2016PHZ0009)



DEPARTMENT OF PHYSICS

INDIAN INSTITUTE OF TECHNOLOGY ROPAR

July, 2023

Chetan Waghela: *NON-RECIPROCAL TRANSMISSION AND NON-HERMITIAN QUANTUM SENSING USING DEFECTIVE OPERATORS*

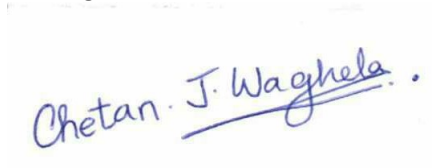
Copyright ©2023, Indian Institute of Technology Ropar
All Rights Reserved

*Dedicated to my grandfather, who valued education despite his illiteracy and inspired the
same in me.*

Declaration of Originality

I hereby declare that the work which is being presented in the thesis entitled **NON-RECIPROCAL TRANSMISSION AND NON-HERMITIAN QUANTUM SENSING USING DEFECTIVE OPERATORS** has been solely authored by me. It presents the result of my own independent investigation/research conducted during the time period from January 2017 to July 2023 under the supervision of Dr. Shubhrangshu Dasgupta, Associate Professor, Department of Physics, IIT Ropar. To the best of my knowledge, it is an original work, both in terms of research content and narrative, and has not been submitted or accepted elsewhere, in part or in full, for the award of any degree, diploma, fellowship, associateship, or similar title of any university or institution. Further, due credit has been attributed to the relevant state-of-the-art and collaborations (if any) with appropriate citations and acknowledgments, in line with established ethical norms and practices. I also declare that any idea/data/fact/source stated in my thesis has not been fabricated/ falsified/ misrepresented. All the principles of academic honesty and integrity have been followed. I fully understand that if the thesis is found to be unoriginal, fabricated, or plagiarized, the Institute reserves the right to withdraw the thesis from its archive and revoke the associated Degree conferred. Additionally, the Institute also reserves the right to appraise all concerned sections of society of the matter for their information and necessary action (if any). If accepted, I hereby consent for my thesis to be available online in the Institute's Open Access repository, inter-library loan, and the title & abstract to be made available to outside organizations.

Signature:



Name: Chetan Waghela

Entry Number: 2016PHZ0009

Program: PhD

Department: Department of Physics

Indian Institute of Technology Ropar

Rupnagar, Punjab 140001.

Date: 21-07-2023

Acknowledgement

It has been a long journey from a child who eagerly awaited bedtime to ponder over the meaning of life and other questions he could think of at that age, to the final stages of his Ph.D. Embracing curiosity and knowledge, this journey has shaped me in profound ways.

There have been numerous people who have positively contributed to this journey, naming all of them would fill pages. Firstly, I would like to acknowledge my grandfather and wife for their sacrifice, constant support and understanding.

As a person who was uneducated and worked as a sweeper, my grandfather witnessed harsh realities of life. He also realized the importance of education which he could not achieve. The financial and emotional support encouraged me to pursue my academic goals without any compromise. Hence, I dedicate this thesis to him.

My wife has been a constant support throughout the journey and has never once discouraged me from pursuing my goals. In fact, she has always brought relief and support during intense times. I truly thank her for what she is. I also thank my parents for their understanding. I thank my little sister for being there for me during my absence at home.

I want to thank my supervisor, Dr. Shubhrangshu Dasgupta for his patience with me. I am aware of the mistakes and hurdles faced during this journey and I truly thank him for his guidance and belief in me. I also express my gratitude towards my DC members Dr. Asoka Biswas, Dr. G Sankara Raju Kosuru, Dr. Shankhadeep Chakraborty, and Chairperson, Prof. P. K. Raina. I also express gratitude towards our H.O.D., Dr. Rakesh Kumar. I thank Anshu and the entire staff and lab assistants at IIT Ropar, Department of Physics.

The friends and colleagues at IIT Ropar have truly been constant support. I truly acknowledge Shivang for being a friend with whom I can share my interests, hobbies and importantly concerns. I cannot forget the intense discussions on politics, technology and history with Devender. I am thankful for academic advice from Anil. Friendly gestures and care from Karun, Kanhaiya, Kanika, Riya and Karunava. I thank Bijoy, Rohit and Sharmishta for feeding me Assamese dishes and the discussions on their work during the cooking sessions. I also thank all the friends for taking care of me during my accident. Atul and Pehchaan Ek Safar team for taking positive action for the community around Ropar and involving me in their endeavor. I also would like to acknowledge Jatin and Ratnakaran for keeping the spirits up during the final stage of the Ph.D and for their best wishes for me. Lastly but not the least I thank all the group members Chayan, Nancy, Manju, Parkhi, Shilpi and wish the best for their academic endeavors.

I acknowledge CSIR for the financial support and IIT Ropar for providing me opportunity to pursue Ph.D.

Certificate

This is to certify that the thesis entitled **NON-RECIPROCAL TRANSMISSION AND NON-HERMITIAN QUANTUM SENSING USING DEFECTIVE OPERATORS**, submitted by **Chetan Waghela (2016PHZ0009)** for the award of the degree of **Doctor of Philosophy** of Indian Institute of Technology Ropar, is a record of bonafide research work carried out under my (our) guidance and supervision. To the best of my knowledge and belief, the work presented in this thesis is original and has not been submitted, either in part or full, for the award of any other degree, diploma, fellowship, associateship or similar title of any university or institution.

In my (our) opinion, the thesis has reached the standard fulfilling the requirements of the regulations relating to the Degree.



Signature of the Supervisor(s)
Name(s): Dr. Shubhrangshu Dasgupta
Department(s): Department of Physics
Indian Institute of Technology Ropar
Rupnagar, Punjab 140001
Date: 21-07-2023

Lay Summary

Mathematics has been an integral part of physics, to the extent that many great physicists including Dr. Feynman has emphasized to "Shut up and calculate !". According to their worldview, we need to focus on the importance of the mathematical calculations and predictions, rather than getting too caught up in philosophical or conceptual debates. Having said this, similar to mathematical theories, physical theories also rely on "postulates". Postulates in short are assumptions on which a theory relies. When certain postulates are changed or modified it can reveal new possible physics and ideas which of course need to stand the test of empirical evidence. Once the empirical evidence is attained the change in postulates can be considered to be fruitful.

In the light of our discussion in previous paragraph. Quantum mechanics and many physical theories rely on the assumption that physical operators need to be Hermitian and unitary. Over the years this assumption has been unchallenged and modifications of these postulates have been unexplored. In this thesis we explore the modifications of this postulate and consider a special class of non-Hermitian and non-unitary physical operators also called as defective physical operators.

We intend to learn the physics, demonstrations and applications of such defective operators through our study. We considered two different cases, that involve such operators. In the first case, we have considered a defective Hamiltonian and discussed in details, how this can help to enhance the precision of a quantum sensor. In the second case, a so-called optomechanical system exhibit non-reciprocal behavior, thanks to a defective scattering matrix. This happens at a single frequency of the input field. We have shown how to achieve tunability of this non-reciprocity.

Abstract

Operators play a crucial role in the field of physics, especially in quantum mechanics and optics, serving as mathematical tools for describing transformations and physical quantities. While normal operators (i.e., Hermitian and unitary operators) have received significant attention, less is known about non-normal operators that may emerge in various physical systems and effects. Defective operators are a particular type of non-normal operator characterized by their non-diagonalizability. Recently, research has revealed the occurrence of defective operators in systems with complete non-reciprocity of light and degeneracy of eigenvalues and eigenvectors of Hamiltonian. These systems have important applications, such as the isolation of light and quantum sensing. This thesis aims to investigate the physics and applications of systems where defective operators arise.

Keywords: non-reciprocity; non-unitarity; isolation; quantum sensing; exceptional points; non-diagonalizable, quantum Fisher information; IBM Q Experience

List of Publications

Journal

Waghela, Chetan, and Shubhrangshu Dasgupta. "Optomechanical isolation with tunable center frequency." *Journal of Physics B: Atomic, Molecular and Optical Physics* 54.17 (2021): 175502.

Waghela, Chetan, and Shubhrangshu Dasgupta. "Simulation of exceptional-point systems on quantum computers for quantum sensing." *arXiv preprint arXiv:2304.12181* (2023). (submitted)

Contents

Declaration	iv
Acknowledgement	v
Certificate	vi
Lay Summary	vii
Abstract	viii
List of Publications	ix
List of Symbols	xix
1 Introduction	1
1.1 Hermitian matrices	1
1.1.1 Algebraic and Geometric multiplicity	4
1.2 Non-Hermitian diagonalizable matrices	7
1.3 Non-Hermitian non-diagonalizable (Defective) matrices	9
1.4 Outline of the Thesis	16
2 Non-Reciprocity and Isolation	19
2.1 Lorentz Reciprocity Theorem	20
2.2 Scattering matrix	22
2.3 LRT using Scattering matrix	23
2.4 Faraday Isolator	25
2.5 Time-reversibility, Non-Reciprocity and Unitarity	26
2.5.1 Non-Reciprocity and Thermodynamics	27
2.6 Applications of non-reciprocity of light	28
2.7 Optomechanical Non-Reciprocity	28
2.7.1 Cavity Optomechanics	29
2.7.2 Generic Optomechanical Isolator	32
2.7.3 OM non-reciprocity and Anti-resonance	38
2.7.4 Issues plaguing OM non-reciprocity	41
2.8 Conclusion	41

3	Non-Hermitian Quantum Sensing	43
3.1	Exceptional point sensing	44
3.2	Metrics for measuring sensor performance	46
3.2.1	Sensitivity	46
3.2.2	Signal-to-noise ratio	47
3.2.3	Quantum Fisher Information	47
3.3	Concerns with EP sensing	49
3.4	QFI for non-Hermitian Hamiltonians	51
3.4.1	Calculating QFI for non-Hermitian Hamiltonians	51
3.4.2	Quantum Fisher Information around EP	51
3.4.3	Why Puiseux series expansion ?	53
3.5	Experimental demonstrations	54
3.6	Conclusion	55
4	Isolation Frequency Tunable Optomechanical Isolator	57
4.1	Requirements for Tunable OM isolator	59
4.2	Tunable model with Quadratic Coupling	63
4.3	Non-Reciprocity and control of isolation frequency	64
4.4	Phase difference in optomechanical couplings	68
4.5	Conclusion	71
5	Simulation of Exceptional Point Sensors on Quantum Computer	73
5.1	Simulating non-unitary dynamics	75
5.2	Gate based Quantum Computing	78
5.3	Simulating EP sensing dynamics	79
5.3.1	Single EP	79
5.3.2	Multiple EP	81
5.4	Noise models on EP sensors	82
5.5	Understanding the simulation from perspective of standard quantum formalisms	86
5.6	Limitations of ancilla-based method for quantum sensing	88
5.7	Conclusion	89
6	Future Work and Conclusion	91
6.1	Future Work	91
6.1.1	Optomechanical Isolators	91
6.1.2	Non-Hermitian quantum sensors	91
6.2	Conclusion of thesis	92
7	Appendix	95
7.1	Code sample for simulating an exceptional point on IBM Q Experience Quantum Lab	95
7.2	Code sample for understanding impact of noise on QFI at exceptional points on IBM Q Experience Quantum Lab	98

List of Figures

1.1	A mind-map showcasing the properties of Hermitian operators.	2
1.2	A mind-map showcasing the properties of non-Hermitian diagonalizable operators.	8
1.3	A mind-map showcasing the properties of non-Hermitian non-diagonalizable operators.	10
2.1	A schematic diagram of Faraday isolator. The black lines represent the polarization orientation of the electromagnetic field. The red solid (blue dotted) line represents forward (backward) direction of light. The diagram showcases that light transmits in forward direction, but not in backward direction. . . .	21
2.2	Schematic diagram showcasing a 1-d scattering process with the incoming and outgoing waves and directions from a device or a material	23
2.3	A general form of optical circuit, with boundary surface Ω	24
2.4	Schematic diagram of an optomechanical setup. It contains an input laser driving of frequency ω (or ω_d). There is a partially reflective fixed mirror and a movable, completely reflective mirror. We call it as mechanical oscillator, which has a mass m , natural frequency ω_m and dissipative constant γ_m . The length of the cavity is L and the displacement of the moving mirror from its equilibrium position is x	30
2.5	Schematic diagram of membrane in the middle setup for optomechanical isolation. The physical setup consists of a cavity optomechanical system with linear optomechanical coupling, along with a time-harmonic mechanical drive for the membrane. The $a_{in,1}$ is the annihilation operator of the probe or input field entering into the cavity coupling to its i th mode. The other notations are explained after the Equation 2.40.	33
2.6	Plot for the scattering probabilities (T) with respect to normalized input frequency ω/γ for various θ . T_{12} (blue), T_{21} (red), (a) $\theta = 0$, (b) $\theta = \pi/2$, (c) $\theta = \pi$ and (d) $\theta = 3\pi/2$. The other parameters chosen are $J = G_1 = G_2 = \gamma_1/2 = \gamma_2/2 = \gamma_b/2 = \gamma/2$ and $\omega_m = \Delta'_1 = \Delta'_2 = \Delta = 10\gamma$. Plots (b) and (d) showcase the isolation feature in opposite directions. Moreover, it is to be noted the isolation occurs exactly at the signal frequency $\omega = 10\gamma$, which is the mechanical oscillators natural frequency (ω_m). This means that the isolation frequency of the isolator is fixed according to the natural frequency of the mechanical oscillator.	37

2.7	A schematic diagram of a coupled pendulum with driving forces $F_1 \cos(\omega_{d1}t + \phi_1)$ and $F_2 \cos(\omega_{d2}t + \phi_2)$	38
2.8	Plots (a) , (c) , (e) on the left panel represent the variation of magnitudes of the $\alpha_{i,ss}$ with respect to Δ for various combinations of ϕ_1 and ϕ_2 . Plots (b) , (d) , (f) on the right panel represent the phases (argument) of the $\alpha_{i,ss}$ with respect to Δ , corresponding to the same combinations of values of ϕ_1 and ϕ_2 . The other parameters chosen are $\gamma_1 = \gamma_2 = \gamma$, $F_1 = F_2 = \gamma$, and $g = \gamma/2$. . .	40
3.1	A schematic diagram of a two level system exhibiting energy degeneracy. When an external perturbation is applied, the degeneracy is generally broken. . . .	45
3.2	Plot of the ratio between the splitting for a perturbed exceptional point system and that for a perturbed Hermitian system, with respect to the perturbation strength ϵ	46
3.3	Difference between precision and accuracy.	48
4.1	A schematic diagram of the OM isolator. This depicts that OM isolator acts as Bandpass filter for an input from right to left direction and Band stop in another. The arrows depict input and output on both sides. The plots represent transmission (T) v/s frequency of the input (ω). The center frequency of both processes should be same and we call it isolation frequency. It is to be noted that filters are resonant systems and hence OM isolator is also a resonant system.	58
4.2	Variation of scattering probabilities T_{12} and T_{21} with the normalized input frequency ω/γ for (a) $\theta = 0$, (b) $\theta = \pi/2$, (c) $\theta = \pi$, and (d) $\theta = 3\pi/2$. The other parameters chosen are $J = G_{11} = G_{21} = \gamma_{a1}/2 = \gamma_{a2}/2 = \gamma_{b1}/8 = \gamma/2$ and $\Delta''_{b1} = \Delta''_{a1} = \Delta''_{a2} = \Delta = 10\gamma$. Clearly, with suitable choice of θ , one can achieve non-reciprocity of in either direction, i.e., either $T_{12} = 0$ or $T_{21} = 0$. .	60
4.3	Complete profile of T v/s signal frequency ω and modified Optomechanical coupling phase θ . (a) $T_{a1 \rightarrow a2}$ for $ G_{11} = G_{21} = \gamma_{a1}/4 = \gamma_{a2}/4 = \gamma_{b1}/4 = \gamma/4$. (b) $T_{a2 \rightarrow a1}$ for $ G_{11} = G_{21} = \gamma_{a1}/4 = \gamma_{a2}/4 = \gamma_{b1}/4 = \gamma/4$. (c) $T_{a1 \rightarrow a2}$ for $ G_{11} = G_{21} = \gamma_{a1}/2 = \gamma_{a2}/2 = \gamma_{b1}/8 = \gamma/2$. (d) $T_{a2 \rightarrow a1}$ for $ G_{11} = G_{21} = \gamma_{a1}/2 = \gamma_{a2}/2 = \gamma_{b1}/8 = \gamma/2$. Black dotted line depicts $\omega = 10\gamma$. Red (Blue) line depicts $\theta = \pi/2$ ($3\pi/2$). Here, (a) and (b) profiles are as observed in [1], however it is to be noted that the parameters are different in this case. . . .	61
4.4	Plot for the scattering probabilities (T) with respect to normalized input frequency ω/γ for various θ . $\theta = 0$ (blue), $\theta = \pi/2$ (red), $\theta = \pi$ (black) and $\theta = 3\pi/2$ (green). The figure (a) depicts the scattering probability from the optical mode a_1 to a_2 , $T_{a1 \rightarrow a2}$, and (b) depicts the scattering probability from the optical mode a_2 to a_1 , $T_{a2 \rightarrow a1}$. The other parameters chosen are $J = G_1 = G_2 = \gamma_1/2 = \gamma_2/2 = \gamma_b/8 = \gamma/2$ and $\Delta'_b = \Delta'_1 = \Delta'_2 = \Delta = 10\gamma$. Red and green curves in both subfigures showcase the non reciprocity. It is to be noticed when one is equal to 1 at 10γ the other is approximately 0 at 10γ	65

- 4.5 Plot of Scattering probability T with respect to ω/γ for various Δ . $\Delta = 8\gamma$ (Blue), $\Delta = 10\gamma$ (Red) and $\Delta = 12\gamma$ (Black). (a) Depicts the scattering probability from optical mode a_1 to a_2 , $T_{a1 \rightarrow a2}$ and (b) Depicts the scattering probability from optical mode a_2 to a_1 , $T_{a2 \rightarrow a1}$. The other parameters chosen are $J = |G_1| = |G_2| = \gamma_1/2 = \gamma_2/2 = \gamma_b/8 = \gamma/2$, $\theta = \pi/2$ and $\Delta''_b = \Delta''_1 = \Delta''_2 = \Delta$. The reader is advised to compare same colors. It demonstrates that the device is frequency-tunable. 69
- 4.6 Variation of absolute difference of scattering probabilities $|T_{21} - T_{12}|$ with respect to γ_b/γ . The other parameters chosen are $J = |G_1| = |G_2| = \gamma_1/2 = \gamma_2/2 = \gamma/2$, $\theta = \pi/2$ or $3\pi/2$ and $\omega = \Delta''_b = \Delta''_1 = \Delta''_2 = \Delta$. Note that these are the parameters which are the requirement for isolation as depicted in Fig. 4.4. Maximum isolation occurs at $\gamma_b/\gamma = 4$ 70
- 5.1 (a) The circuit diagram for simulating non-unitary evolution. We decompose the non-unitary transformation using SVD transform into $U\Sigma V^\dagger$. Then using the procedure as mentioned in the text, we apply the operations on the input state $|\xi, 0\rangle$ to obtain $|\psi\rangle$. This is followed by a post-selection protocol applied on the output using "Repeat until success" (RUS) method. Here we discard all measurements results which project the ancilla in the state $|1\rangle$, and repeat the procedure till we get the ancilla to be in the state $|0\rangle$. This collapses the state to $\frac{1}{N}|\phi, 0\rangle$ which contains the required state due to non-unitary evolution. On the right hand side, we schematically represent the non-unitary gate. Note that 'cr' in the circuit refers to classical register. (b) The circuit diagram for the SWAP test to measure fidelity between two states i.e. $F = \frac{1}{|\mathcal{N}_1\mathcal{N}_2|^2} |\langle\phi_2|\phi_1\rangle|^2$. We can consider $\frac{1}{\mathcal{N}_1}|\phi_1\rangle$ and $\frac{1}{\mathcal{N}_2}|\phi_2\rangle$ to be the states as given in Eq. 5.10. The circuit between the dashed vertical barriers represents SWAP test. We specifically mention \mathcal{N} in denominator to show that non-unitary circuits un-normalize input states and we need to consider normalization of such output states. 77
- 5.2 The variation of $\log(QFI_\gamma)$ with respect to γ for the Hamiltonian NH_1 (5.12). The QFI_γ diverges at the EP, which appears at $\gamma = 0.5$. Blue curve represents theoretical plot and red dots indicate simulation values at various γ values. 80
- 5.3 The variation of $\log(QFI)$ with respect to γ for the Hamiltonian NH_2 (5.15). The QFI diverges at the EP, which appears at $\gamma = 0$ when $g = |\epsilon|/2$. Blue curve represents theoretical plot and red dots indicate simulation values at various γ values. 81
- 5.4 The variation of $\log(QFI)$ with respect to γ for the Hamiltonian NH_3 (5.16). The QFI diverges at the EP, which appears at $\gamma = 0.05a$, where the integer a varies from 8 to 12. Blue curve represents theoretical plot and red dots indicate simulation results or various values of γ 82
- 5.5 The variation of $\max[\log(QFI)]$ at EP with respect to the amplitude damping parameter b (a) for NH_1 and (b) for NH_2 83

5.6	The variation of $\max[\log(QFI)]$ with respect to p for different Pauli errors for NH_1 . (a) Bit-Flip error: $p_1 = p, p_2 = 0, p_3 = 0$. (b) Bit-Phase-Flip error: $p_1 = 0, p_2 = p, p_3 = 0$. (c) Phase flip error: $p_1 = 0, p_2 = 0, p_3 = p$. (d) All errors with equal probability: $p_1 = p_2 = p_3 = p/3$	84
5.7	The variation of $\max[\log(QFI)]$ with respect to p for different Pauli errors for NH_2 . (a) Bit-Flip error: $p_1 = p, p_2 = 0, p_3 = 0$. (b) Bit-Phase-Flip error: $p_1 = 0, p_2 = p, p_3 = 0$. (c) Phase flip error: $p_1 = 0, p_2 = 0, p_3 = p$. (d) All errors with equal probability: $p_1 = p_2 = p_3 = p/3$	85
5.8	A three level system used to describe the relation between the non-unitary dynamics discussed in the thesis to the Lindbladian formalism. The effective hamiltonian of the two level sub-system (involving $ e\rangle$ and $ f\rangle$) is given by Eq.5.20. In the Lindblad formalism the evolution of the density state of the sub-system is given by Eq. 5.23.	86

List of Tables

2.1	Definition of each element of the scattering matrix.	23
4.1	Table listing the experiments (E) and theoretical proposals for the experiment (TP) which could be useful to achieve the physical system depicted in this article. Q stands for quadratic coupling, MD stands for mechanical driving, RD stands for reversed dissipation.	71

List of Symbols

$\langle|$: right eigenvector

$|\psi^J\rangle$: Generalized eigenvector satisfying $(A - \lambda I)^k |\psi\rangle = 0$ for $k > 1$.

$| \rangle$: left eigenvector

λ : Symbol for eigenvalues

$Algmul(\lambda)$: Algebraic multiplicity of eigenvalue λ

$Geomul(\lambda)$: Geometric multiplicity of eigenvalue λ

H: Symbol for Hermitian operator

LRT: Lorentz Reciprocity Theorem

NHD: Non-Hermitian diagonalizable matrices

NHND: Non-Hermitian non-diagonalizable matrices (Defective)

QCRB: Quantum Cramer Rao Bound

QFI: Quantum Fisher Information

S: Scattering matrix

Chapter 1

Introduction

Mathematics plays a fundamental role in governing physics. It provides a precise and rigorous language for formulating physical laws, describing natural phenomena, making predictions, and understanding the underlying principles that govern the universe.

Usually interesting avenues arise when concepts in mathematics are applied to unexplored areas in physics. One largely unexplored area in physics is the phenomenon where defective (non-diagonalizable) operators arise. In this thesis we are interested in exploring physics and applications of such systems.

In this chapter we will introduce several properties and definitions related to the subject. We will prove several theorems and lemmas, too. In section 1.1 we will discuss the Hermitian operators and their mathematical properties. Later we will discuss Non-Hermitian matrices. The discussion is divided into two sections section 1.2 and section 1.3. We finally conclude the chapter, with an outline of this thesis.

1.1 Hermitian matrices

Definition 1.1.1. Hermitian operators are defined as following the relation, $H = H^\dagger$. Here, † represents complex conjugation and transposition. The combined operation is also sometimes known as "Hermitian conjugation" [2].

Let us understand the properties of Hermitian operators. Figure 1.1 provides a mind-map of the properties and relations of Hermitian operators. We will provide proof of every property mentioned in the mind-map. The mind-map has several types of connections/arrows. The color and type of arrow represents the type of relation as given below:

- black double arrows represent 'iff' condition
- red single arrow represent 'if' condition
- green arrows represent 'types of'

This representation will be used throughout the thesis.

Theorem 1.1.1. *All eigenvalues of a Hermitian operator (λ) are always real, i.e $\lambda = \lambda^*$. The inverse is not true.*

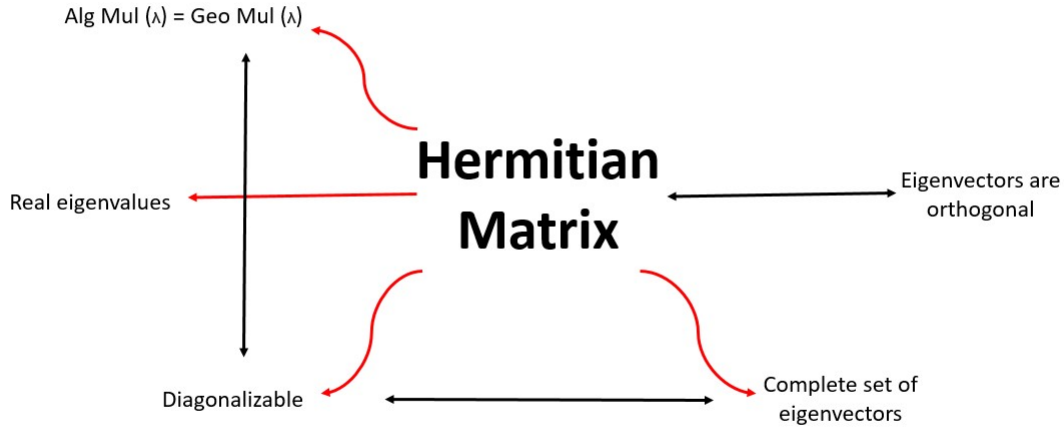


Figure 1.1: A mind-map showcasing the properties of Hermitian operators.

Proof. Consider a Hermitian operator following the eigenvalue equation

$$H |\psi_i\rangle = \lambda_i |\psi_i\rangle , \quad (1.1)$$

such that $H = H^\dagger$. Here $|\psi_i\rangle$ are the eigenvectors corresponding to eigenvalues λ_i . Taking transpose conjugate on both sides of Equation 1.1 we get $\langle\psi_i| H = \lambda_i^* \langle\psi_i|$, we have used the fact that H is Hermitian. Multiplying by $|\psi_i\rangle$ from right we get after some manipulations

$$(\lambda_i - \lambda_i^*) \langle\psi_i|\psi_i\rangle = 0 . \quad (1.2)$$

Since, $|\psi_i\rangle$ is non-zero, $\lambda_i = \lambda_i^*$, i.e., λ is real.

Note, the inverse, i.e. all matrices with real eigenvalues are Hermitian, is not true. It can be proved by an example. For example, consider, a non-Hermitian matrix

$$\begin{pmatrix} 3 & 1 \\ 2 & 4 \end{pmatrix} . \quad (1.3)$$

It has real eigenvalues 5 and 2, which completes our proof of the theorem stated above, This property is depicted in Figure 1.1. \square

It must be reminded here that, in quantum mechanics, the use of Hermitian operators is essential for describing physical observables and calculating the outcomes of measurements in experiments. The real eigenvalues of Hermitian operators and their ortho-normal eigenvectors are crucial properties that make them an indispensable tool for studying and understanding quantum systems.

Theorem 1.1.2. *The eigenvectors of Hermitian matrix are orthogonal.*

Proof. Consider a Hermitian matrix H . All Hermitian matrices are normal, [2], i.e., $HH^\dagger = H^\dagger H$. However, according to Schur decomposition any square matrix [3],

$$H = QTQ^{-1}, \quad (1.4)$$

where Q is a unitary matrix and T is an upper-triangular matrix. Now, according the property of normality we have

$$HH^\dagger = QTT^\dagger Q^\dagger \text{ and } H^\dagger H = QT^\dagger T Q^\dagger, \quad (1.5)$$

Therefore $TT^\dagger = T^\dagger T$, due to normality of H and by comparison. Now, as T is upper triangular T^\dagger is lower triangular, which implies from the previous derivation that T is a diagonal matrix.

The eigenvectors of a diagonal matrix are orthogonal; hence, the same property is followed by eigenvectors of T as it is a diagonal matrix. Mathematically, the eigenvectors $|\phi\rangle$ of T follow

$$\langle \phi_i | \phi_j \rangle = \delta_{ij}. \quad (1.6)$$

We have considered these vectors $|\phi\rangle$ to be normalized. Here δ_{ij} denotes the kronecker delta function. According to Equation 1.4, the eigenvectors of T are related to eigenvectors of H by a similarity transformation

$$Q|\phi\rangle = |\psi\rangle. \quad (1.7)$$

Now, it remains to explore the orthogonality property. We can also deduce from Equation 1.4 that

$$H^\dagger = Q^{-1\dagger} T^\dagger Q^\dagger = QT^\dagger Q^{-1} = QTQ^{-1}. \quad (1.8)$$

As the matrix H is Hermitian, it has real eigenvalues and it leads to $T = T^\dagger$. Hence, if $|\xi\rangle$ are eigenvectors of H^\dagger , then $Q|\phi\rangle = |\xi\rangle$, implying

$$\langle \phi | Q^\dagger = \langle \xi |. \quad (1.9)$$

Now, using Equation 1.7 and Equation 1.9 we see that

$$\langle \phi_i Q^\dagger | Q \phi_j \rangle = \langle \phi_i | \phi_j \rangle = \delta_{ij} = \langle \xi_i | \psi_j \rangle, \quad (1.10)$$

where we used the fact that Q is unitary and used the relation Equation 1.6. Now, as the matrix is Hermitian $H = H^\dagger$, their eigenvectors have to be the same, $|\xi\rangle = |\psi\rangle$, and therefore

$$\langle \psi_i | \psi_j \rangle = \delta_{ij}. \quad (1.11)$$

Note that the above relation applies to the special case $H = H^\dagger$, i.e. the matrix being Hermitian. For a non-Hermitian matrix, "bi-orthogonality" applies and it will be discussed later. Check Figure 1.1. \square

1.1.1 Algebraic and Geometric multiplicity

Definition 1.1.2. A matrix (A) is known as diagonalizable if it can be transformed by a similarity transformation ($S^{-1}AS = D$) into a diagonal matrix (D) with the diagonal entries as the eigenvalues of the original matrix itself, i.e. the diagonal matrix $D = \text{diag}(\lambda_1, \lambda_2, \dots, \lambda_n)$ where λ_i are eigenvalues of the matrix. If no such transformation exists, then it is known as non-diagonalizable or "defective".

Before we go further we need to define what is algebraic and geometric multiplicity. They are essential quantities to know if a matrix is diagonalizable (Def. 1.1.2) or not.

Definition 1.1.3. A matrix has associated eigenvectors ($|\psi\rangle$) which follow the rule $A|\psi\rangle = \lambda|\psi\rangle$. We can create a set of eigenvectors of a matrix. If each eigenvector of a matrix is linearly independent of each other i.e. the size of the set is equal to the dimension of the matrix, then the set is known as complete set of eigenvectors.

Definition 1.1.4. Algebraic multiplicity of an eigenvalue of a matrix, denoted as $Algmul(\lambda)$, is the number of times the eigenvalue repeats itself. In short it is the degeneracy of the eigenvalue.

Example 1.1.1. $A = \begin{pmatrix} 2+i & 0 & 0 \\ 0 & 2+i & 0 \\ 0 & 0 & 2 \end{pmatrix}$ There are two distinct eigenvalues of the above matrix. $\lambda_1 = 2+i$ and $\lambda_2 = 2$. $Algmul(\lambda_1) = 2$ and $Algmul(\lambda_2) = 1$.

The sum of all the algebraic multiplicities of all the eigenvalues of the matrix is equal to the dimension of the matrix.

Definition 1.1.5. Geometric multiplicity of an eigenvalue is the number of linearly independent eigenvectors of a particular eigenvalue. It is denoted by $Geomul(\lambda)$. Let us define it as degeneracy of eigenvectors as preferred by physicists.

It is not hard to realize that if the sum of all the geometric multiplicities of all the eigenvalues is less than the dimension of the matrix, then the set of eigenvectors of the matrix is not complete according to Def. 1.1.3. Hence, the idea of geometric multiplicity is intimately connected to the idea of complete set of eigenvectors. Moreover, a matrix is diagonalizable iff it has complete set of eigenvectors. Hence, a defective matrix has incomplete set of eigenvectors. We will show this by proof in following sections.

For example, for the matrix

$$A = \begin{pmatrix} 3 & 2 \\ 0 & 3 \end{pmatrix}, \quad (1.12)$$

there are two eigenvalues of A and both are equal to 3, and the linearly independent eigenvector corresponding to the same eigenvalue is $(1, 0)^T$. No other linearly independent eigenvectors exist. Therefore $Algmul(3) = 2$ and $Geomul(3) = 1$. It can also be seen that a complete set of eigenvectors does not exist as sum of all the geometric multiplicities is equal to 1 and dimension of the matrix is 2. Moreover, this matrix cannot be diagonalized ever, as we mentioned earlier that a matrix with incomplete set of eigenvectors cannot be diagonalized.

Theorem 1.1.3. *Prove that $Algmul(\lambda) \geq Geomul(\lambda)$ for a given eigenvalue λ of a matrix A .*

Proof. Let us try to prove the following in unconventional and easier way. The conventional proof can be found at [4].

We first prove that distinct eigenvalues have linearly independent eigenvectors (Note: the reverse is not true). We then show how for a 2x2 matrix the $Algmul(\lambda) \geq Geomul(\lambda)$ using the previous result.

Suppose $|\psi_1\rangle$ and $|\psi_2\rangle$ correspond to distinct eigenvalues λ_1 and λ_2 . To show that $|\psi_1\rangle$ and $|\psi_2\rangle$ are always linearly independent we need to show that

$$a_1 |\psi_1\rangle + a_2 |\psi_1\rangle = \mathbf{0} , \quad (1.13)$$

only when $a_1 = a_2 = 0$.

Applying the matrix A on both sides of Equation 1.13, we get

$$a_1 A |\psi_1\rangle + a_2 A |\psi_1\rangle = A \mathbf{0} = a_1 \lambda_1 |\psi_1\rangle + a_2 \lambda_2 |\psi_1\rangle = \mathbf{0} , \quad (1.14)$$

and if we multiply λ_1 to Equation 1.13, then

$$a_1 \lambda_1 |\psi_1\rangle + a_2 \lambda_1 |\psi_1\rangle = \mathbf{0} . \quad (1.15)$$

Taking difference between Equation 1.14 and Equation 1.15, we get

$$a_2 (\lambda_2 - \lambda_1) |\psi_2\rangle = \mathbf{0} . \quad (1.16)$$

Since the eigenvalues are distinct and $|\psi_2\rangle$ is not a zero vector, $a_2 = 0$. Using this in Equation 1.13 we see that $a_1 = 0$, too. Hence, $|\psi_1\rangle$ and $|\psi_2\rangle$ are linearly independent. We can use induction to prove the same for higher dimensions.

Having understood this let us consider a 2x2 matrix. For such a matrix several cases arise with respect to the eigenvalues.

- $\lambda_1 \neq \lambda_2$

As all the eigenvalues are distinct the eigenvectors $|\psi_1\rangle$ and $|\psi_2\rangle$ are linearly independent as proven earlier. Therefore $Algmul(\lambda_i) = Geomul(\lambda_i) = 1$.

- $\lambda_1 = \lambda_2 = \lambda$

In this case two cases arise:

1. $|\psi_1\rangle$ and $|\psi_2\rangle$ are linearly independent and $Algmul(\lambda) = Geomul(\lambda) = 2$.
2. $|\psi_1\rangle$ and $|\psi_2\rangle$ are not linearly independent and $Algmul(\lambda) = 2$ and $Geomul(\lambda) = 1$.

We can see that in all the above cases, the algebraic multiplicity of an eigenvalue is always greater than its geometric multiplicity. This derivation can be generalized to higher dimensions. \square

It is also important to notice that there is no degeneracy of eigenvectors without the degeneracy of the eigenvalues. We can also colloquially say that at such degeneracies eigenvalues and eigenvectors "coalesce". These kind of degeneracies are known as "Exceptional points" or "Non-Hermitian degeneracies" in physics literature [5, 6, 7].

Theorem 1.1.4. *A matrix is diagonalizable iff it has complete set of eigenvectors.*

Proof. First let us prove that a diagonalizable matrix has a complete set of eigenvectors. Suppose A is a diagonalizable matrix. Then there exists a transformation $S^{-1}AS = D$, where D is the matrix as defined earlier. We will first prove that $S = [|\psi_1\rangle, |\psi_2\rangle \dots |\psi_n\rangle]$, where $|\psi_i\rangle$ are eigenvectors of A and n is dimension of the matrix, so as we get the transformation as above.

Consider the transformation

$$AS = A[|\psi_1\rangle, |\psi_2\rangle \dots |\psi_n\rangle] = [\lambda_1 |\psi_1\rangle, \lambda_2 |\psi_2\rangle \dots \lambda_n |\psi_n\rangle] = SD, \quad (1.17)$$

where $D = \text{diag}(\lambda_1, \lambda_2, \dots, \lambda_n)$.

Hence, $S^{-1}AS$ transformation does the trick to achieve the diagonalization to matrix D . Now, suppose the set is not complete in that case one of the columns of S will be a zero vector. Hence, the matrix S will not be invertible as it will be a singular matrix. Hence, a diagonalizable matrix has a complete set of eigenvectors.

Now we will prove the converse i.e. a matrix which has complete set of eigenvectors is diagonalizable.

Assume a matrix A has a complete set of eigenvectors $|\psi_1\rangle, |\psi_2\rangle \dots |\psi_n\rangle$ (n is the dimension of the matrix). Then $A|\psi_1\rangle = \lambda_1 |\psi_1\rangle$, $A|\psi_2\rangle = \lambda_2 |\psi_2\rangle \dots A|\psi_n\rangle = \lambda_n |\psi_n\rangle$. If we create a matrix $S = [|\psi_1\rangle, |\psi_2\rangle \dots |\psi_n\rangle]$, then we can show that $AS = SD$ using the relation above, such that $D = \text{diag}(\lambda_1, \lambda_2, \dots, \lambda_n)$. Hence, the converse is also true. \square

Theorem 1.1.5. *A Hermitian matrix H is always diagonalizable ($S^{-1}HS = D$ where $D = \text{diag}(\lambda_1 \dots \lambda_n)$) and all its eigenvalues λ have $\text{Algmul}(\lambda) = \text{Geomul}(\lambda)$. Moreover the similarity transformation for diagonalization is unitary i.e. $S^\dagger = S^{-1}$*

Proof. In Theorem 1.1.3, we already proved that for distinct eigenvalues for a general matrix the eigenvectors are linearly independent. Now consider non-distinct eigenvalues of the matrix H , let us denote them as $|\psi_1\rangle$ and $|\psi_2\rangle$. Let us prove that they are linearly independent for a Hermitian matrix. By definition, two vectors are linearly independent if

$$a_1 |\psi_1\rangle + a_2 |\psi_2\rangle = \mathbf{0}. \quad (1.18)$$

iff $a_1 = a_2 = 0$.

Taking inner product with $\langle\psi_1|$ from left on Equation 1.18, we get $a_1 \langle\psi_1|\psi_1\rangle + a_2 \langle\psi_1|\psi_2\rangle = 0$. Using the orthogonality property Theorem 1.1.2, we get $a_1 \langle\psi_1|\psi_1\rangle = 0$, this is only possible if $a_1 = 0$. Substituting the value back in Equation 1.18 we get a_2 . Hence, the eigenvectors of non-distinct eigenvectors of a Hermitian matrix H are all linearly independent. Hence, we can see that both distinct and non-distinct eigenvalues of a Hermitian matrix has linearly independent set of eigenvectors. Hence, the following properties hold true for Hermitian matrices:

- A complete set of eigenvectors exist for a Hermitian matrix H .
- As a complete set of eigenvectors exist for H it is always diagonalizable according to Theorem 1.1.4
- $Algmul(\lambda) = Geomul(\lambda)$ for all eigenvalue as a complete set of eigenvectors exist. Note, the reverse of this statement is not true as there is no proof that only Hermitian matrices have linearly independent eigenvectors.

These relations are equivalent and are as shown by black arrow in Figure 1.1. □

Example 1.1.2. In conjunction to our statement earlier that even non-Hermitian matrices can sometimes be diagonalizable, consider an example of a non-Hermitian matrix as given in Equation 1.3. The matrix is clearly diagonalizable, with the similarity transformation matrix being $S = \begin{pmatrix} -1 & 1 \\ 1 & 2 \end{pmatrix}$. We can also check that the elements of S are given as

$$(|\psi_1\rangle) \quad (|\psi_2\rangle) \quad \cdot \quad \cdot \quad \cdot \quad (|\psi_n\rangle) , \quad (1.19)$$

where $|\psi_i\rangle$ are eigenvectors of H and 'n' is the dimension of the matrix.

1.2 Non-Hermitian diagonalizable matrices

As we derived earlier, all Hermitian matrices are diagonalizable. Hence a defective matrix cannot be Hermitian. All Hermitian matrices also possess a complete set of eigenvectors according to Theorem 1.1.4. The set of non-Hermitian matrices can hence be divided into two types, a) Diagonalizable (NHD), possessing a complete set of eigenvectors and b) Defective or Non-diagonalizable (NHND), not possessing a complete set of eigenvectors. This is depicted by green arrows in Figure 1.2. Let us understand the properties of diagonalizable non-Hermitian matrices in this section. The details of the derivations and definitions can be found in the standard textbooks [8, 9, 10].

It can be seen from Figure 1.2 that NHD matrices can be divided into two types, one having real eigenvalues and other having complex eigenvalues. We perform such a classification because much attention has been paid to such operators with real eigenvalues in recent decades by physicists [11, 12, 13, 14].

We will first prove that the eigenvalues of non-Hermitian matrices in general are complex conjugates of each other.

Theorem 1.2.1. Consider a matrix NH s.t. $NH \neq NH^\dagger$ i.e. it is non-Hermitian. Let λ and λ' be eigenvalues of NH and NH^\dagger respectively, then $\lambda' = \lambda^*$.

Proof. We know from given information that

$$NH |\psi_i\rangle = \lambda_i |\psi_i\rangle , \quad (1.20)$$

$$NH^\dagger |\xi_i\rangle = \lambda' |\xi_i\rangle , \quad (1.21)$$

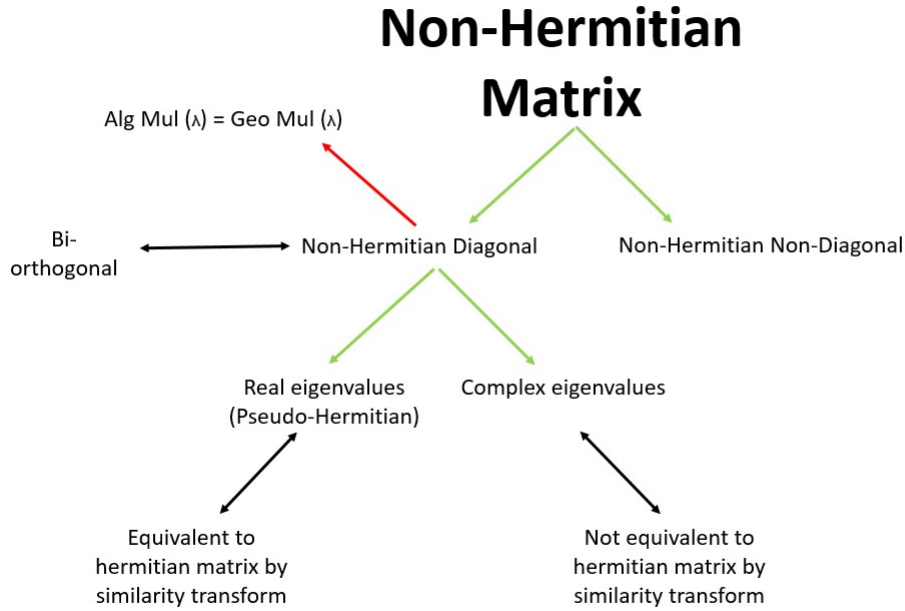


Figure 1.2: A mind-map showcasing the properties of non-Hermitian diagonalizable operators.

where $|\psi_i\rangle$ and $|\xi_i\rangle$ are the eigenvectors of NH and NH^\dagger respectively. Taking conjugate transpose of Equation 1.20 and then multiplying by $|\xi_i\rangle$ from right we get

$$\langle \psi_i | NH^\dagger | \xi_i \rangle = \lambda_i^* \langle \psi_i | \xi_i \rangle . \quad (1.22)$$

Using Equation 1.21, we get

$$\langle \psi_i | \xi_i \rangle \lambda_i' = \lambda_i^* \langle \psi_i | \xi_i \rangle . \quad (1.23)$$

Hence, by cancelling $\langle \psi_i | \xi_i \rangle$ from both sides, we get

$$\lambda_i = \lambda_i'^* . \quad (1.24)$$

This proves our theorem, and it applies to any non-Hermitian matrix, irrespective of it being diagonalizable or not. \square

One important property of NHD matrices is that the eigenvectors follow the criterion of bi-orthogonality. Let us understand what is bi-orthogonality and how it differs from orthogonality.

Theorem 1.2.2. *If a non-Hermitian matrix NH has eigenvectors $|\psi_i\rangle$ and its Hermitian conjugate matrix, $NH^\dagger \neq NH$ has eigenvectors $|\xi_i\rangle$ then the following rule is obeyed, $\langle \xi_i | \psi_j \rangle = \delta_{ij}$ (Note: We consider the eigenvectors to be normalized). This is known as bi-orthogonality (or bi-orthonormality).*

Proof. As the matrix NH is diagonalizable it has complete set of eigenvectors. Let us consider a matrix X which diagonalizes NH :

$$NH = XDX^{-1} . \quad (1.25)$$

where X follows Equation 1.19. Here D is a diagonal matrix with diagonal entries being eigenvalues (λ) of NH . Consider that Y diagonalizes NH^\dagger .

$$NH^\dagger = YD^*Y^{-1} . \quad (1.26)$$

where Y follows Equation 1.19 with $|\psi_i\rangle$ being replaced by $|\xi_i\rangle$. Here D^* is a diagonal matrix with diagonal entries being eigenvalues (λ^*) of NH^\dagger , according to Theorem 1.2.1. However if we take Hermitian conjugate of Equation 1.25 we get

$$NH^\dagger = X^{-1\dagger} D^* X^\dagger . \quad (1.27)$$

Comparing Equation 1.26 and Equation 1.27 we see that

$$X^\dagger = Y^{-1} . \quad (1.28)$$

Therefore, $Y^\dagger X = X^{-1} X = I$, where I is an identity matrix. However, as the elements of X and Y are nothing but eigenvectors of NH and NH^\dagger , respectively, according to Equation 1.19, we proved that

$$\langle \xi_i | \psi_j \rangle = \delta_{ij} . \quad (1.29)$$

This proves our theorem, considering the eigenvectors are normalized. The theorem applies irrespective of NHD matrix having complete set of real eigenvalues or not. \square

Example 1.2.1.

$$NH = \begin{pmatrix} 2 & 1 \\ 3 & 4 \end{pmatrix} . \quad (1.30)$$

This matrix has eigenvalues $\lambda_1 = 5$ and $\lambda_2 = 1$ with corresponding eigenvectors $|\psi_1\rangle = (1, 3)^T$ and $|\psi_2\rangle = (-1, 1)^T$. Its Hermitian conjugate has eigenvalues $\lambda'_1 = 5$ and $\lambda'_2 = 1$ with eigenvectors $|\xi_1\rangle = (1, 1)^T$ and $|\xi_2\rangle = (-3, 1)^T$. The normalization constant for both vectors is $\frac{1}{2}$. The bi-orthogonality can be easily verified, i.e. $\langle \xi_i | \psi_j \rangle = \delta_{ij}$. Also, note that $\langle \psi_i | \psi_j \rangle \neq \delta_{ij}$. This property is depicted in Figure 1.2.

Theorem 1.2.3. A NHD matrix has $Algmul(\lambda) = Geomul(\lambda)$ for all the eigenvalues λ .

Proof. A NHD matrix has a complete set of eigenvectors by defn. Hence, according to the same arguments in Theorem 1.1.3, the statement in the theorem is correct. \square

1.3 Non-Hermitian non-diagonalizable (Defective) matrices

The mind map of properties of non-diagonalizable matrices is depicted in Figure 1.3. As all Hermitian matrices are diagonalizable, all non-diagonalizable matrices are by default non-Hermitian. As discussed in subsection 1.1.1, a non-diagonalizable matrix has $Algmul(\lambda) > Geomul(\lambda)$.

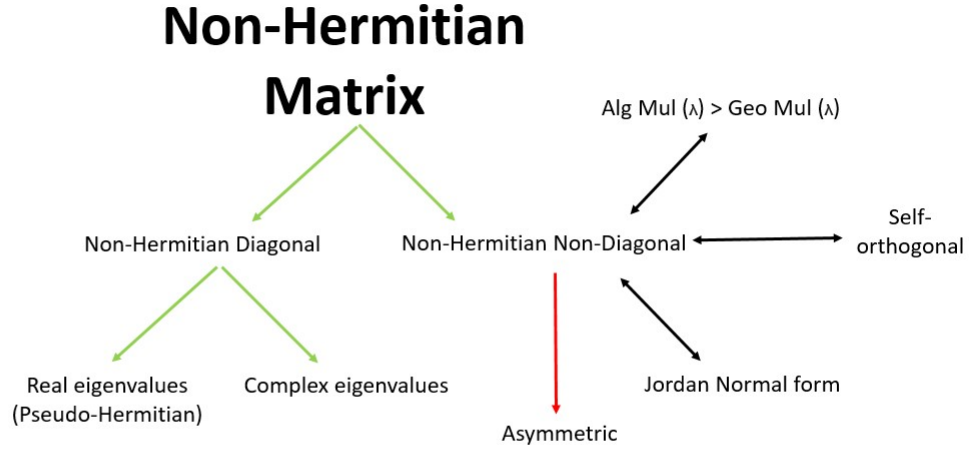


Figure 1.3: A mind-map showcasing the properties of non-Hermitian non-diagonalizable operators.

Definition 1.3.1. An order $(Or(A, \lambda))$ of defectiveness of an eigenvalue λ of a matrix A is the value of $[Algmul(\lambda) - Geomul(\lambda)] + 1$ of the "defective eigenvalue" λ .

Example 1.3.1. Consider a defective matrix of

$$NH = \begin{pmatrix} 3 & 1 & 0 & 0 \\ 0 & 3 & 1 & 0 \\ 0 & 0 & 3 & 0 \\ 0 & 0 & 0 & 3 \end{pmatrix}. \quad (1.31)$$

It has all eigenvalues $\lambda = 3$. Hence, $Algmul(\lambda = 3) = 4$ and there are 2 independent eigenvectors possible, $(0, 0, 0, 1)^T$ and $(1, 0, 0, 0)^T$, hence $Geomul(\lambda = 3) = 2$. Hence the order of defectiveness in the eigenvalue according to our defn above is $Or(\lambda, NH) = 3$ or third order. We will restrict ourselves to 2x2 matrices henceforth, for derivations.

- For a 2×2 defective matrix the highest order of defectiveness of the eigenvalue that can be reached is 2.
- For a 2×2 matrix there is only one eigenvalue (λ) and it is defective. This leads to $Algmul(\lambda) = 2$ and $Geomul(\lambda) = 1$, for any 2×2 defective matrix. We mention this specifically because for higher dimension matrices, some eigenvalues can be defective while others need not be as can be checked in 1.3.1.

General results for higher order defectiveness will be provided without proof.

Before we proceed we need to understand the concept of generalized eigenvectors. As already discussed this in subsection 1.1.1, defective matrices are defective because they do not possess a complete set of eigenvectors, i.e. the number of ordinary eigenvectors is less than the dimensions of the matrix. Specifically, generalized eigenvectors are a set of vectors that are used in combination with eigenvectors to create a basis for a matrix A that is defective, or does not have enough eigenvectors to form a basis on its own. Hence, the generalized eigenvectors are used to complete the basis. These eigenvectors are not unique and there can be several different choices of such eigenvectors that can be used to form a basis.

For example, suppose that a 2×2 matrix A which has one distinct eigenvalue with only one corresponding eigenvector. In this case, the matrix A is defective, since it does not have enough eigenvectors to form a basis on its own. To construct a basis, we can use the eigenvector and a corresponding generalized eigenvector. Let us define it formally.

Definition 1.3.2. A generalized eigenvector of a 2×2 matrix NH is a nonzero vector $|\psi^J\rangle$ that satisfies the equation $(NH - \lambda I)|\psi^J\rangle = |\psi\rangle$. Here λ is degenerate eigenvalue and $|\psi\rangle$ is its ordinary eigenvector.

Hence, we can write the equations

$$NH|\psi\rangle = \lambda|\psi\rangle, \quad (1.32)$$

$$NH|\psi^J\rangle = \lambda|\psi^J\rangle + |\psi\rangle \quad (1.33)$$

or

$$(NH - \lambda I)|\psi\rangle = 0, \quad (1.34)$$

$$(NH - \lambda I)^2|\psi^J\rangle = 0. \quad (1.35)$$

The Equation 1.35 can be derived as follows. According to the Equation 1.33, $|\psi\rangle = (NH - \lambda I)|\psi^J\rangle$. Substituting it in the Equation 1.34 we get $(NH - \lambda I)[(NH - \lambda I)|\psi^J\rangle] = 0 = (NH - \lambda I)^2|\psi^J\rangle$, which is nothing but the Equation 1.35. Note $|\psi^J\rangle$ is not an eigenvector of NH .

The generalized eigenvectors of an eigenvalue of a matrix are linearly independent from all other eigenvectors of the matrix. Let us prove this result for a 2×2 matrix for simplification.

Theorem 1.3.1. Consider a 2×2 matrix NH with the defective eigenvalue λ . The ordinary eigenvector $|\psi\rangle$ and generalized eigenvector $|\psi^J\rangle$ of this matrix are linearly independent of each other.

Proof. Two vectors $|\psi^J\rangle$ and $|\psi\rangle$ are linearly independent only when they follow the equation:

$$c_1|\psi\rangle + c_2|\psi^J\rangle = 0, \quad (1.36)$$

iff $c_1 = c_2 = 0$. To check the linear independence, let us consider Equation 1.36. After multiplying it by NH from left, we get

$$c_1NH|\psi\rangle + c_2NH|\psi^J\rangle = c_1\lambda|\psi\rangle + c_2(\lambda|\psi^J\rangle + |\psi\rangle) = c_1(\lambda + 1)|\psi\rangle + \lambda|\psi^J\rangle = 0. \quad (1.37)$$

In the above, we used the Equation 1.32 and Equation 1.33. If we multiply Equation 1.36 by λ , we get

$$c_1 \lambda |\psi\rangle + c_2 \lambda |\psi^J\rangle = 0. \quad (1.38)$$

Taking the difference between Equation 1.37 and Equation 1.38 we get $c_1 |\psi\rangle = 0$, which is only possible if $c_1 = 0$. Now substituting $c_1 = 0$ in Equation 1.36 we get $c_2 |\psi^J\rangle = 0$ which is only possible when $c_2 = 0$. Hence, Equation 1.36 is only satisfied when both $c_1 = c_2 = 0$ which proves our claim of linear independence by definition. \square

Theorem 1.3.2. *Consider a defective 2×2 matrix NH . Consider a 2×2 matrix $S = [|\psi\rangle, |\psi^J\rangle]$, where $|\psi\rangle$ and $|\psi^J\rangle$ are ordinary eigenvector and generalized eigenvector, respectively of eigenvalue λ . Then in general*

$$NH = SJS^{-1}, \quad (1.39)$$

where

$$J = \begin{pmatrix} \lambda & 1 \\ 0 & \lambda \end{pmatrix}. \quad (1.40)$$

Proof. Multiplying $(NH - \lambda I)$ with S from left we have

$$(NH - \lambda I)S = (NH - \lambda I)[|\psi\rangle, |\psi^J\rangle] = [0, |\psi\rangle] = S[0, e_1] = SJ'. \quad (1.41)$$

We used the relations Equation 1.33 and $e_1 = (1, 0)^T$ (as $Se_1 = |\psi\rangle$). We define $[0, e_1] = J'$. From the above relation we can see that

$$NHS = S(J' - \lambda I) = SJ, \quad (1.42)$$

where $J = \begin{pmatrix} \lambda & 1 \\ 0 & \lambda \end{pmatrix}$. Hence we easily can check that Equation 1.39 is in fact correct. \square

Moreover, this theorem applies in general for higher dimensional matrices and more complex degeneracies. Namely, in general we can state that the best we can do with diagonalizing a defective matrix is convert it into direct sums of Jordan block matrices of the type 'J' above. This has been mentioned in Figure 1.3.

Definition 1.3.3. A matrix J which has all diagonal entries equal and to a particular number and at least one supradiagonal entries being '1', is known as a Jordan block matrix. All other entries of the matrix are 0.

Example 1.3.2. $J = \begin{pmatrix} 3 & 1 & 0 \\ 0 & 3 & 0 \\ 0 & 0 & 3 \end{pmatrix}$ is a type of Jordan block matrix as defined above.

Now we discuss one of the main results of the section, i.e. "self-orthogonality". When a matrix is defective the eigenvectors follow the rule of "self-orthogonality" rather than "bi-orthogonality" or "orthogonality".

Theorem 1.3.3. *Consider a 2×2 matrix NH with eigenvector $|\psi\rangle$ and with generalized eigenvector $|\psi^J\rangle$. Consider $|\xi\rangle$ as eigenvector of NH^\dagger and $|\xi^J\rangle$ as generalized eigenvector. Then*

$$\langle \xi | \psi \rangle = \langle \xi^J | \psi^J \rangle = 0, \quad (1.43)$$

and

$$\langle \xi | \psi^J \rangle = \langle \xi^J | \psi \rangle = 1 \quad (1.44)$$

(considering eigenvectors are normalized accordingly). These properties are known as "self-orthogonality".

Notice how they are different from the rules of "bi-orthogonality", Equation 1.29.

Proof. In previous theorem Theorem 1.3.2 we saw that for a defective matrix NH , $NH = SJS^{-1}$, where $J = \begin{pmatrix} \lambda & 1 \\ 0 & \lambda \end{pmatrix}$ is the Jordan block matrix and $S = [|\psi\rangle, |\psi^J\rangle]$. Now for the Hermitian conjugate of NH ,

$$NH^\dagger = S'J'S'^{-1}, \quad S' = [|\xi^J\rangle, |\xi\rangle], \quad (1.45)$$

where $|\xi\rangle$ and $|\xi^J\rangle$ are ordinary and generalized eigenvectors of NH^\dagger for eigenvalue λ . Notice the arrangement of the vectors with respect to that in S . In such an arrangement J' is a lower triangular matrix rather than upper: $J' = \begin{pmatrix} \lambda^* & 0 \\ 1 & \lambda^* \end{pmatrix}$. Moreover, the eigenvalues of NH^\dagger are λ^* due to the Theorem 1.2.1. Also notice

$$J' = J^\dagger. \quad (1.46)$$

Taking Hermitian conjugate of Equation 1.39 we have

$$NH^\dagger = (S^{-1})^\dagger J^\dagger S^\dagger. \quad (1.47)$$

Comparing Equation 1.45 and Equation 1.47 and using Equation 1.46, we get

$$S^\dagger = S'^{-1}, \quad (1.48)$$

and $S^\dagger S' = I = [|\psi\rangle, |\psi^J\rangle] \cdot [|\xi^J\rangle, |\xi\rangle]$, with I as the identity matrix. Hence, we see that $\langle \psi | \xi^J \rangle = \langle \psi^J | \xi \rangle = 1$ and $\langle \psi | \xi \rangle = \langle \psi^J | \xi^J \rangle = 0$. Taking complex conjugates of the above relations, we prove our claim in the theorem.

This can be seen in the mindmap Figure 1.3.

□

Definition 1.3.4. A generalized eigenvector of rank ' k ' of a matrix A is a nonzero vector $|\psi\rangle$ that satisfies the equation $(A - \lambda I)^k |\psi\rangle = 0$, where λ is an eigenvalue of A , and k is a positive integer. In other words, a generalized eigenvector is a vector that, when raised to the power of k and multiplied by $(A - \lambda I)$, yields the zero vector. When $k = 1$, the generalized eigenvector is the same as the usual eigenvector. Let us denote them with a suffix ' J ' on top for any generalized eigenvector with $k > 1$. The number of such generalized eigenvectors that exist is equal to the $Or(A, \lambda)$ of the eigenvalue λ .

The generalized eigenvectors follow the equation

$$(A - \lambda I) |\psi\rangle = 0, \quad (1.49)$$

$$(A - \lambda I)^2 |\psi_1^J\rangle = 0, \quad (1.50)$$

$$\vdots$$

$$(A - \lambda I)^k |\psi_{k-1}^J\rangle = 0. \quad (1.51)$$

We can also check (compare $(A - \lambda I) |\psi\rangle = 0 = (A - \lambda I)^2 |\psi_1^J\rangle$) that the generalized eigenvectors of eigenvalue λ follow the equations below:

$$A |\psi\rangle = \lambda |\psi\rangle, \quad (1.52)$$

$$A |\psi_1^J\rangle = \lambda |\psi_1^J\rangle + |\psi\rangle, \quad (1.53)$$

$$\vdots$$

$$A |\psi_{k-1}^J\rangle = \lambda |\psi_{k-1}^J\rangle + |\psi_{k-2}^J\rangle. \quad (1.54)$$

Example 1.3.3. Consider the matrix

$$A = \begin{pmatrix} 1 & 3 & 0 \\ 0 & 1 & 2 \\ 0 & 0 & 1 \end{pmatrix}. \quad (1.55)$$

This matrix is defective with eigenvalue $\lambda = 1$ and eigenvector $|\psi\rangle = (1, 0, 0)^T$. It can be seen the eigenvector $|\psi\rangle$ easily fits in the definition of "generalized eigenvector" with $k = 1$.

The eigenvector $|\psi_1^J\rangle = (0, 1, 0)^T$ follows the equation $(A - \lambda I)^2 |\psi_1^J\rangle = 0$. We can check that, $(A - \lambda I) |\psi_1^J\rangle \neq 0$. Hence $|\psi_1^J\rangle$ is a generalized eigenvector of rank $k = 2$ for the eigenvalue $\lambda = 1$. Similarly $|\psi_2^J\rangle = (0, 0, 1)^T$ can be found satisfying, $(A - \lambda I)^3 |\psi_2^J\rangle = 0$. We can check that, $(A - \lambda I)^2 |\psi_2^J\rangle \neq 0$. Therefore, $|\psi_2^J\rangle$ is a generalized eigenvector of rank $k = 3$ for the eigenvalue $\lambda = 1$.

Theorem 1.3.4. Suppose $|\psi_k^J\rangle$ is a rank k generalized eigenvector corresponding to λ , such that $k > 1$. Then $(A - \lambda I) |\psi_k^J\rangle$ is a rank $k - 1$ generalized eigenvector.

Proof. As $|\psi_k^J\rangle$ is a rank k generalized eigenvector corresponding to λ , s.t. $k > 1$. We have $(A - \lambda I)^k |\psi_k^J\rangle = 0$, we can manipulate the equation to $(A - \lambda I)^{k-1} [(A - \lambda I) |\psi_k^J\rangle] = 0$, we can easily check that the vector $(A - \lambda I) |\psi_k^J\rangle = |\psi_{k-1}^J\rangle$ satisfies the equation for a rank $k - 1$ generalized eigenvector. Hence, $(A - \lambda I) |\psi_k^J\rangle$ is a rank $k - 1$ generalized eigenvector. \square

A defective matrix follows "self-orthogonality", unlike "bi-orthogonality" and "orthogonality" for other types of matrices.

Theorem 1.3.5. If $|\psi_k\rangle$ are eigenvectors of NHND matrix NH and $|\xi_k\rangle$ are eigenvectors of its Hermitian conjugate for the defective eigenvalue λ_k , then $\langle \xi_k | \psi_k \rangle = 0$, instead of being non-zero as in the case of bi-orthogonality. This is known as "self-orthogonality".

Proof. Consider a 2×2 matrix which is NHD. It has two eigenvalues λ_i and two eigenvectors $|\psi_i\rangle$ ($i = 1, 2$) where they follow the bi-orthogonality relation Equation 1.29. Now as discussed in Theorem 1.1.3 as a matrix becomes non-diagonalizable (NHND) the eigenvalues and eigenvectors both coalesce.

We see that $\lambda_1 = \lambda_2 = \lambda$ and $|\psi_1\rangle = |\psi_2\rangle = |\psi\rangle$ and vice-versa for its Hermitian conjugate with eigenvectors $|\xi_i\rangle$. According to the bi-orthogonality rule, for the matrix away from such degeneracy, $\langle \xi_1 | \psi_2 \rangle = \langle \xi_2 | \psi_1 \rangle = 0$ and $\langle \xi_1 | \psi_1 \rangle = \langle \xi_2 | \psi_2 \rangle = c$ (considering the eigenvectors are not normalized). However, due to coalescence at degeneracy, the above relations can only be satisfied if $c = 0$. This gives $\langle \xi | \psi \rangle = 0$.

Hence for any 2×2 matrix at EP degeneracy, the eigenvectors follow the rule of self-orthogonality as discussed earlier. This idea can be generalized to higher order matrices and exceptional point degeneracies. \square

Definition 1.3.5. Let $|\psi_k\rangle$ be a rank k generalized eigenvector of eigenvalue λ . Then

$$[|\psi_k\rangle, (A - \lambda I)|\psi_k\rangle, \dots, (A - \lambda I)^{k-1}|\psi_k\rangle] \quad (1.56)$$

is a chain of generalized eigenvectors corresponding to λ . The eigenvector $(A - \lambda I)^{k-1}|\psi_k\rangle$ is the ordinary eigenvector, if $k = \text{Or}(A, \lambda)$.

Definition 1.3.6. A " $k \times k$ " matrix $J_{k,\lambda}$ is said to be a Jordan block of dimension k and of eigenvalue λ iff its diagonal entries are equal to λ and its supradiagonal entries are all equal to 1 or 0, otherwise all other entries apart from them in the matrix are 0.

Example 1.3.4. $J_{k,\lambda} = \begin{pmatrix} 2+i & 1 & 0 \\ 0 & 2+i & 1 \\ 0 & 0 & 2+i \end{pmatrix}$ is a Jordan block of $k = 3$ with eigenvalue $2 + i$.

Theorem 1.3.6. Let A be a $n \times n$ matrix, λ be an eigenvalue of A , and $|\psi_k^J\rangle$ be a generalized eigenvector of A associated to this eigenvalue. Let k be the smallest integer such that $(A - \lambda I)^k |\psi_k^J\rangle = 0$. Consider $P_\lambda = [(A - \lambda I)^{k-1} |\psi_k^J\rangle, (A - \lambda I)^{k-2} |\psi_k^J\rangle \dots |\psi_k^J\rangle]$. This will be a $n \times k$ matrix whose columns are vectors of the Jordan chain discussed above. Then we have

$$AP_\lambda = P_\lambda J_{k,\lambda}, \quad (1.57)$$

where $J_{k,\lambda}$ is a Jordan block of dimension k and has eigenvalues λ .

Proof. Consider

$$\begin{aligned} (A - \lambda I)P_\lambda &= (A - \lambda I)[(A - \lambda I)^{k-1} |\psi_k^J\rangle, (A - \lambda I)^{k-2} |\psi_k^J\rangle, \dots |\psi_k^J\rangle] \\ &= [(A - \lambda I)^k |\psi_k^J\rangle, (A - \lambda I)^{k-1} |\psi_k^J\rangle, \dots (A - \lambda I) |\psi_k^J\rangle] \\ &= [0, (A - \lambda I)^{k-1} |\psi_k^J\rangle, \dots (A - \lambda I) |\psi_k^J\rangle], \end{aligned}$$

where we used the definition $(A - \lambda I)^k |\psi_k^J\rangle = 0$. Also note that $P_\lambda e_1 = (A - \lambda I)^{k-1} |\psi_k^J\rangle$, where $e_1 = (1, 0, 0, 0, \dots)^T$ and so on... Therefore,

$$\begin{aligned}
 (A - \lambda I)P_\lambda &= [0, P_\lambda e_1, \dots, P_\lambda e_{k-1}] \\
 &= P_\lambda [0, e_1, e_2, \dots, e_{k-1}] \\
 &= P_\lambda \begin{pmatrix} 0 & 1 & 0 & \cdots & 0 \\ 0 & 0 & 1 & \ddots & 0 \\ 0 & 0 & 0 & \cdots & 1 \\ 0 & 0 & 0 & \cdots & 0 \end{pmatrix} \\
 &= P_\lambda (J_{k,\lambda} - \lambda I) \\
 &= P_\lambda J_{k,\lambda} - \lambda P_\lambda.
 \end{aligned}$$

From the above relation it is easy to obtain Equation 1.57. □

Example 1.3.5. $A = \begin{pmatrix} 1 & 3 & -2 \\ -2 & 6 & -2 \\ -1 & 2 & 1 \end{pmatrix}$ has for eigenvalue $\lambda = 3$ ($\text{Algmul}(\lambda = 3) = 2$ and $\text{Geomul}(\lambda + 3) = 1$), generalized eigenvector of rank $k = 1$, $|\psi\rangle = (2, 2, 1)^T$ and generalized eigenvector of rank $k = 2$ is $|\psi_1^J\rangle = (-1, 0, 0)^T$. This gives us $P_\lambda = [|\psi_1^J\rangle, |\psi\rangle]$. It can be checked that $AP_\lambda = \begin{pmatrix} 6 & -1 \\ 6 & 2 \\ 3 & 1 \end{pmatrix}$ and the value of $P_\lambda J_{2,\lambda} = \begin{pmatrix} 6 & -1 \\ 6 & 2 \\ 3 & 1 \end{pmatrix}$ where $J_{2,\lambda} = \begin{pmatrix} 3 & 1 \\ 0 & 3 \end{pmatrix}$. Thus this example satisfies, Equation 1.57.

1.4 Outline of the Thesis

In this section we lay out some descriptions of each chapter in the thesis.

Chapter 2: In this chapter we discuss about the concept of non-reciprocity. We explore the properties of non-reciprocal systems with respect to scattering matrices. We show how at isolation, the scattering matrix is a special type of a defective matrix. Then we learn a few examples of non-reciprocal devices (called as isolators) of light. Firstly, we understand the Faraday Isolator, which uses the magneto-optic effect for its operation. Later we understand Optomechanical isolator which uses a membrane in the middle setup. We showcase that it works on the principle of "anti-resonance" and through it we showcase the issues plaguing them w.r.t the bandwidth of operation.

Chapter 3: Here we discuss Non-Hermitian quantum sensors. We discuss how exceptional point degeneracy can be used to increase sensitivity of a sensor. We show how the Hamiltonians of such systems are defective matrices. We discuss some issues raised in terms of efficiency of using such sensors. We then discuss quantum Fisher information being a better metric of performance and how even it is improved by a exceptional point sensor. For this we introduce the concept of Puiseux series and perturbation from such degenerate points.

Chapter 4: In Chapter 2 we learn that the frequency at which isolation occurs in optomechanical isolators is fixed upon fabrication of the membrane in the membrane in the middle setup. In this chapter we discuss about frequency tunable optomechanical isolator. We propose that this can be achieved using a mechanical drive for the membrane. We discuss the Hamiltonian and setup for such a device and showcase how this can be done.

Chapter 5: The physical realization of exceptional point sensors has been elusive. In this chapter we showcase a method to democratize achievement of such systems using quantum computers. We simulate such systems on IBM quantum computer using the Qiskit framework. We explore the performance parameters of such sensors and try to settle certain debates in the literature.

Chapter 6: The conclusion of the thesis is set out in chapter 6, which summarizes the major findings of the research and also outline the scope of future studies.

Chapter 7: We had included the all the relevant sample codes that we used for simulating the quantum sensor in cloud quantum computers.

Chapter 2

Non-Reciprocity and Isolation

The phenomenon of reciprocity is achieved when the response of a system remains the same regardless of the direction of an input signal. However, in certain materials and structures, this symmetry is broken, leading to non-reciprocal transmission. Complete non-reciprocal transmission is known as "isolation".

An electronic diode is an example of such a system. In a diode, current can flow more easily in one direction than in the opposite direction. This property is achieved through the use of a p-n junction, where one side of the diode is doped with a material that has an excess of electrons (n-type), and the other side is doped with a material that has a deficiency of electrons (p-type). When a voltage is applied in the forward bias direction (positive terminal connected to the p-side and negative terminal connected to the n-side), the diode allows current to flow easily due to the alignment of energy bands in the p-n junction. However, when the voltage is applied in the reverse bias direction, the diode exhibits a high resistance and only allows a negligible current to pass through. This non-reciprocal behavior of a diode is essential in various electronic applications. For instance, diodes are used in rectifiers to convert alternating current (AC) to direct current (DC) by allowing current flow only in one direction. They also serve as protection devices by preventing the reverse flow of current and thereby protecting other components from damage.

Another example is that of a valve, which controls the fluid flow. Non-reciprocal transmission in a valve refers to the property of allowing fluid flow in one direction while blocking or significantly restricting flow in the opposite direction. Valves are essential components in various fluid control systems, and the incorporation of non-reciprocal transmission properties can enhance their functionality and efficiency.

Light, with its dual nature as both a wave and a particle, has long been a subject of fascination and investigation. Its ability to propagate through different media and to interact with matter has allowed for numerous technological advancements. One intriguing phenomenon that challenges traditional notions of symmetry is the non-reciprocal transmission of light. This behavior, where light propagates differently depending on its direction of propagation, has sparked considerable interest in the field of optics.

Non-reciprocal transmission of light is fundamentally restricted by "Lorentz Reciprocity theorem" [15, 16]. The Lorentz reciprocity theorem is a fundamental principle in classical electromagnetism that establishes a relationship between the transmission and reception of electromagnetic waves in reciprocal systems. It provides a powerful tool for understanding

and analyzing the behavior of electromagnetic fields in symmetric environments. The theorem, named after the Dutch physicist Hendrik Lorentz, states that in a reciprocal system which obeys the Maxwell's equations, the response of the system to a source placed at one point is the same as the response to an identical source placed at the same location, but with the roles of the source and receiver interchanged. In simpler terms, it implies that the transmission characteristics between two points in a reciprocal system are the same regardless of which point is the source and which point is the receiver.

The most common example of devices which achieve non-reciprocity of light are called as "Faraday isolators". Faraday isolators, named after the renowned physicist Michael Faraday, are important devices used in optical systems to achieve non-reciprocal transmission of light. They are widely employed to protect laser sources from back-reflections and to control the directionality of light propagation. The primary function of a Faraday isolator is to allow light to transmit in one direction while blocking or significantly attenuating its transmission in the opposite direction. This unidirectional transmission is based on the phenomenon of magneto-optical rotation, which occurs in certain materials under the influence of a magnetic field.

The key component of a Faraday isolator is the Faraday rotator, typically made of a material with strong magneto-optical properties such as a rare-earth iron garnet or a terbium gallium garnet crystal. When a magnetic field is applied along the direction of light propagation, the Faraday rotator induces a rotation of the polarization plane of the incident light. The amount of rotation depends on the strength of the magnetic field and the properties of the material. To complete the Faraday isolator setup, two polarizers are placed before and after the Faraday rotator. These polarizers are oriented such that they transmit light with a specific polarization orientation and block light with orthogonal polarization. When light passes through the first polarizer, it acquires a polarization state that matches the transmission axis of the Faraday rotator. As it enters the Faraday rotator, the rotation induced by the magnetic field ensures that the light's polarization aligns with the transmission axis of the second polarizer, allowing it to transmit through. However, when the light tries to propagate in the opposite direction, the rotation induced by the magnetic field is in the opposite direction. As a result, the light's polarization is orthogonal to the transmission axis of the second polarizer, causing it to be blocked or significantly attenuated Figure 2.1.

In this chapter we will first consider the "Lorentz reciprocity theorem" and understand the basic necessities for achieving non-reciprocity of light. Next, we will explain the working principle of a Faraday isolator, in mathematical term. Later in this chapter, we will describe in details how non-reciprocity and isolation is achieved using optomechanics. We will interpret our results in terms of anti-resonance and discuss the factors that can affect the optomechanical non-reciprocity.

2.1 Lorentz Reciprocity Theorem

As discussed earlier, the Lorentz Reciprocity Theorem (LRT) governs the properties of systems which will be reciprocal in transmission of light. Let us understand the theorem in more detail. The LRT can be formally derived by initially considering a specific volume that contains two distinct sets of sources, described by the current densities, J_1 and J_2 . These



Figure 2.1: A schematic diagram of Faraday isolator. The black lines represent the polarization orientation of the electromagnetic field. The red solid (blue dotted) line represents forward (backward) direction of light. The diagram showcases that light transmits in forward direction, but not in backward direction.

sources individually generate electric and magnetic fields, denoted as \vec{E}_1 , \vec{H}_1 , and \vec{E}_2 , \vec{H}_2 , respectively.

Recalling the Maxwell's curl equations, we get

$$\nabla \times \vec{E}_1 = -i\omega\mu\vec{H}_1, \quad (2.1)$$

$$\nabla \times \vec{H}_1 = i\omega\epsilon\vec{E}_1 + \vec{J}_1, \quad (2.2)$$

$$\nabla \times \vec{E}_2 = -i\omega\mu\vec{H}_2, \quad (2.3)$$

$$\nabla \times \vec{H}_2 = i\omega\epsilon\vec{E}_2 + \vec{J}_2, \quad (2.4)$$

where ϵ and μ are permittivity and permeability of the material. Multiplying Equation 2.1 with \vec{H}_2 and the time-harmonic source-less Maxwell's equation Equation 2.2 (by putting $\vec{J}_1 = 0$) with \vec{E}_2 , from the left, gives us

$$\vec{H}_2 \cdot (\nabla \times \vec{E}_1) + \vec{E}_2 \cdot (\nabla \times \vec{H}_1) = i\omega(\vec{E}_2 \epsilon \vec{E}_1 - \vec{H}_2 \mu \vec{H}_1). \quad (2.5)$$

Similarly, multiplying Equation 2.3 with \vec{H}_1 and Equation 2.1 with \vec{E}_1 from the left, we get after considering $\vec{J}_2 = 0$

$$\vec{H}_1 \cdot (\nabla \times \vec{E}_2) + \vec{E}_1 \cdot (\nabla \times \vec{H}_2) = i\omega(\vec{E}_1 \epsilon \vec{E}_2 - \vec{H}_1 \mu \vec{H}_2). \quad (2.6)$$

Subtracting Equation 2.6 and Equation 2.5 we then have

$$\vec{H}_1 \cdot (\nabla \times \vec{E}_2) + \vec{E}_1 \cdot (\nabla \times \vec{H}_2) - \vec{H}_2 \cdot (\nabla \times \vec{E}_1) - \vec{E}_2 \cdot (\nabla \times \vec{H}_1) = i\omega(\vec{E}_1 \epsilon \vec{E}_2 - \vec{H}_1 \mu \vec{H}_2 - \vec{E}_2 \epsilon \vec{E}_1 + \vec{H}_2 \mu \vec{H}_1). \quad (2.7)$$

Using the relation between any two vectors \vec{a} and \vec{b} : $\nabla(\vec{a} \times \vec{b}) = \vec{b}(\nabla \times \vec{a}) - \vec{a}(\nabla \times \vec{b})$ in Equation 2.7, we get

$$\nabla \cdot (\vec{E}_2 \times \vec{H}_1 + \vec{H}_2 \times \vec{E}_1) = \nabla \cdot (\vec{E}_2 \times \vec{H}_1 - \vec{E}_1 \times \vec{H}_2) = i\omega(\vec{E}_1 \epsilon \vec{E}_2 - \vec{H}_1 \mu \vec{H}_2 - \vec{E}_2 \epsilon \vec{E}_1 + \vec{H}_2 \mu \vec{H}_1) . \quad (2.8)$$

If ϵ and μ are symmetric matrices or are scalars, the right hand side of the above equation vanishes and we finally get

$$\nabla \cdot (\vec{E}_2 \times \vec{H}_1 - \vec{E}_1 \times \vec{H}_2) = 0 . \quad (2.9)$$

Note that the above relation holds true even when the ϵ and μ are complex numbers, representing loss or gain.

Note that we have made several assumptions in the above derivation, e.g.,

- ϵ and μ are symmetric (them being matrices)
- We have considered linearity i.e. ϵ and μ are matrices or scalars
- The relation Equation 2.9 is time-independent, which is evident from the Maxwell's equations that are used

These are the conditions necessary for achieving reciprocity of light. If one of the assumptions is broken, we can achieve non-reciprocity. In the next Section, we will carry forward with the assumptions we made earlier, explain what is a scattering matrix.

2.2 Scattering matrix

A scattering matrix, also known as an S-matrix, is a mathematical representation used primarily in the field of quantum mechanics and optics to describe the scattering of particles or waves. It provides a way to understand how particles or waves interact with each other when they collide or propagate through a physical system. The S-matrix relates the initial state of incoming particles or waves to the final state of outgoing particles or waves, taking into account the scattering process that occurs in between. It characterizes the amplitude and phase of the scattered waves for different possible outcomes of the scattering process.

In quantum mechanics, particles and waves are described by wave functions, and the S-matrix connects the wave functions of the incoming and outgoing particles. The S-matrix is typically represented as a matrix of complex numbers, with elements that correspond to transition amplitudes between different states. Mathematically,

$$\Psi_{out} = \begin{pmatrix} A_{L,out} \\ A_{R,out} \end{pmatrix} = \begin{pmatrix} S_{11} & S_{12} \\ S_{21} & S_{22} \end{pmatrix} \begin{pmatrix} A_{L,in} \\ A_{R,in} \end{pmatrix} = S \Psi_{in} , \quad (2.10)$$

where $A_{L/R,out}$ are outgoing wave amplitudes on left and right of the device respectively, $A_{L/R,in}$ are incoming wave amplitudes on left and right of the device respectively. S is the scattering matrix for a 1-d scattering process (Figure 2.2).

The elements of the scattering matrix are defined as given in Table 2.1.

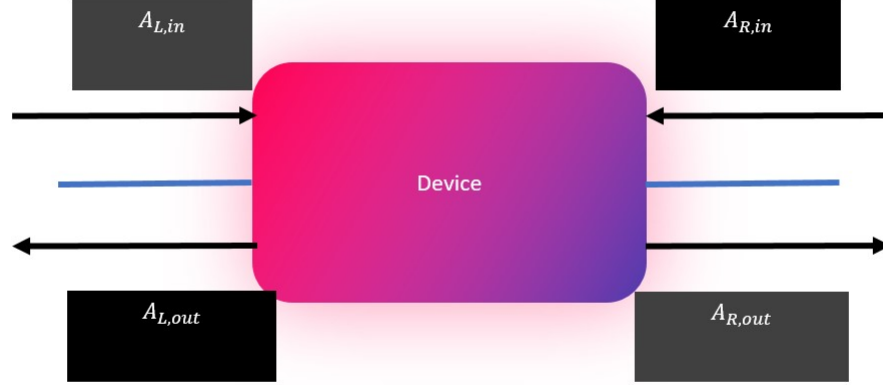


Figure 2.2: Schematic diagram showcasing a 1-d scattering process with the incoming and outgoing waves and directions from a device or a material

$$\begin{array}{c|c} S_{11} = \frac{A_{L,out}}{A_{L,in}} \big|_{A_{R,in}=0} & S_{12} = \frac{A_{L,out}}{A_{R,in}} \big|_{A_{L,in}=0} \\ \hline S_{21} = \frac{A_{R,out}}{A_{L,in}} \big|_{A_{R,in}=0} & S_{22} = \frac{A_{R,out}}{A_{R,in}} \big|_{A_{L,in}=0} \end{array}$$

Table 2.1: Definition of each element of the scattering matrix.

2.3 LRT using Scattering matrix

Let us consider an optical circuit, with boundary surface Ω as shown in Figure 2.3). The components of electric and magnetic field are tangential to the surface.

$$E_{T\mu}(x, y, z) = (a_\mu e^{-i\beta_\mu z} + b_\mu e^{i\beta_\mu z}) \hat{e}_{T\mu}(x, y) , \quad (2.11)$$

$$H_{T\mu}(x, y, z) = (a_\mu e^{-i\beta_\mu z} + b_\mu e^{i\beta_\mu z}) \hat{h}_{T\mu}(x, y) . \quad (2.12)$$

Here a_μ is the amplitude of the field going into the surface, b_μ is that of the field coming out of surface and β_μ is the propagation constant. Note that $\iint_{\Omega} (\hat{e}_\mu \times \hat{h}_\nu) \cdot \hat{n} dS = 2\delta_{\mu\nu}$, as these two unit vectors are perpendicular to each other. If we choose $z = 0$, then the total field is

$$E_T = \sum_{\mu} (a_\mu + b_\mu) \hat{e}_{T\mu} , \quad (2.13)$$

$$H_T = \sum_{\mu} (a_\mu - b_\mu) \hat{h}_{T\mu} . \quad (2.14)$$

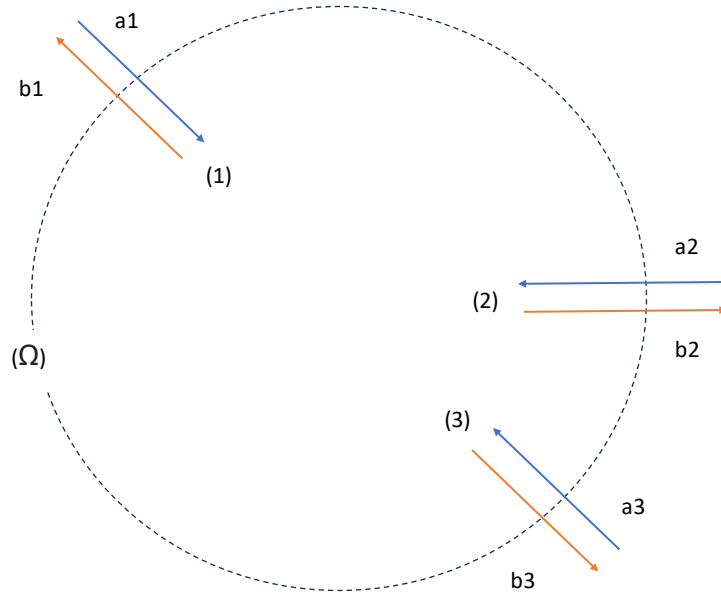


Figure 2.3: A general form of optical circuit, with boundary surface Ω .

Let us define the relation between the amplitudes, b and a by what we call a "Scattering matrix" $S_{\mu\nu}$:

$$b_{\mu} = S_{\mu\nu} a_{\nu} . \quad (2.15)$$

Next, we integrate Equation 2.9 over volume enclosed by the surface Ω , and get

$$\iiint_V \nabla \cdot (\vec{E}_1 \times \vec{H}_2 - \vec{E}_2 \times \vec{H}_1) dV = \oint_S (\vec{E}_1 \times \vec{H}_2 - \vec{E}_2 \times \vec{H}_1) \cdot \hat{n} dS = I_1 - I_2 = 0 , \quad (2.16)$$

where we have used the divergence theorem ($\iiint_V \nabla \cdot A dv' = \oint_S A ds'$). The expression of I_1 can be identified as, after using Equation 2.13 Equation 2.14

$$\begin{aligned} I_1 &= \oint_S \left(\sum_{\mu} (a_{1\mu} + b_{1\mu}) \hat{e}_{1\mu} \times \sum_{\nu} (a_{2\nu} + b_{2\nu}) \hat{h}_{2\nu} \right) \cdot \hat{n} dS \\ &= \sum_{\mu, \nu} (a_{1\mu} a_{2\nu} - a_{1\mu} b_{2\nu} + b_{1\mu} a_{2\nu} - b_{1\mu} b_{2\nu}) \oint (\hat{e}_{1\mu} \times \hat{h}_{2\nu}) \cdot \hat{n} dS \\ &= 2 \sum_{\mu} (a_{1\mu} a_{2\mu} - a_{1\mu} b_{2\mu} + b_{1\mu} a_{2\mu} - b_{1\mu} b_{2\mu}) , \end{aligned} \quad (2.17)$$

where we have noted that the integration results into $2\delta_{\mu\nu}$, as seen earlier. Similarly,

$$I_2 = 2 \sum_{\mu} (a_{2\mu} a_{1\mu} - a_{2\mu} b_{1\mu} + b_{2\mu} a_{1\mu} - b_{2\mu} b_{1\mu}) . \quad (2.18)$$

such that

$$I_1 - I_2 = 4 \sum_{\mu} (b_{1\mu} a_{2\mu} - a_{1\mu} b_{2\mu}) . \quad (2.19)$$

But, according to Equation 2.16, $I_1 - I_2 = 0$. Therefore

$$\sum_{\mu} (b_{1\mu} a_{2\mu} - a_{1\mu} b_{2\mu}) = 0 \quad (2.20)$$

$$\text{or } B_1 A_2^T - A_1 B_2^T = 0 . \quad (2.21)$$

$B_1 = (b_1, b_2, \dots) = \{b_{\mu}\}$ is a matrix, and similarly $A_{1,2}$ and B_2 . However, as we had defined $B = SA$ in Equation 2.15, we have

$$(SA_1)A_2^T - A_1(SA_2)^T = a_1 a_2 (S - S^T) = 0 . \quad (2.22)$$

This implies $S - S^T = 0$, i.e.,

$$S = S^T . \quad (2.23)$$

This shows that with the assumptions and equations used for materials which obey reciprocity, their scattering matrix is symmetric. This is another version of LRT.

Let us now explore an example of a system where non-reciprocity is achieved, namely Faraday isolator.

Definition 2.3.1. A system is reciprocal iff the scattering matrix of the system obeys $S = S^T$.

2.4 Faraday Isolator

As discussed earlier, the Faraday isolators work on the principle of "Faraday rotation". Faraday rotation describes the rotation of the polarization plane of light as it passes through a material in the presence of a magnetic field. The amount of rotation is given by the following equation:

$$\theta = VBL . \quad (2.24)$$

where θ is the rotation angle, V is the Verdet constant (a material-specific property), B is the magnetic field strength, and L is the length of the material traversed by the light.

Let us consider two scenarios: one for light traveling in forward direction (i.e. left to right) and the other for light traveling in backward direction (i.e. right to left).

a) Forward direction only ($A_{R,in} = 0$)

- An unpolarized light enters from left $|\Psi_{L,in}\rangle = |V\rangle$, where $|V\rangle$ represents vertically polarized light. Therefore, its amplitude is normalized as $A_{L,in} = 1$.
- This light then enters the Faraday rotator and it is changed to $\cos(\theta) |V\rangle + e^{i\phi} \sin(\theta) |H\rangle$, where θ follows the Equation 2.24 and $|H\rangle$ denotes horizontally polarized light. We assume that $\phi = 0$, always. If the setup is such that $\theta = 45^\circ$ then the output is $|D\rangle = \frac{1}{\sqrt{2}}(|H\rangle + |V\rangle)$.

- The light then passes through another polarizer which can be represented by the operator $|D\rangle\langle D|$, where $|D\rangle$ denotes diagonal polarization and this gives us the final output state $|\Psi_{R,out}\rangle = |D\rangle$. The output amplitude is $A_{R,out} = 1$.
- According to the definitions of S , this gives us $S_{11} = 0$ and $S_{21} = 1$, considering no back-reflections.
- a) Backward direction only ($A_{L,in} = 0$)
- An unpolarized light enters from right $|\Psi_{R,in}\rangle = |D\rangle$, where $|D\rangle$ is diagonally polarized light. Thus the input field is $A_{R,in} = 1$ in normalized form.
- This light then enters the Faraday rotator and it is changed to $\cos(\theta)|D\rangle + e^{i\phi}\sin(\theta)|A\rangle$. Here $|A\rangle$ denotes anti-diagonally polarized light. For $\theta = 45^\circ$ (this can be achieved without changing anything in the previous case, even keeping the direction of the magnetic field in the same direction), the output is $|H\rangle$.
- The light then passes through another polarizer which can be represented using an operator $|V\rangle\langle V|$, and this gives us the final output state $|\Psi_{L,out}\rangle = 0$. The output amplitude is then $A_{L,out} = 0$.
- This leads to $S_{12} = S_{22} = 0$, considering no back reflections.

Finally, the scattering matrix therefore in this case is

$$S = \begin{pmatrix} 0 & 0 \\ 1 & 0 \end{pmatrix}. \quad (2.25)$$

We can see that light travels in only one direction and not the another. Similarly we can change the direction of the magnetic field to achieve the scattering matrix to be $S = \begin{pmatrix} 0 & 1 \\ 0 & 0 \end{pmatrix}$, such that the transmission is in opposite direction to previous case only.

We can see that $S \neq S^T$ in both cases and hence the system is non-reciprocal. Moreover, it is not only non-reciprocal, it is achieving complete non-reciprocity, also known as "isolation".

Definition 2.4.1. A system is known as non-reciprocal iff its scattering matrix obeys $S \neq S^T$. For a 1-d system (also known as a two port system) a system obeys complete non-reciprocity if $S = \begin{pmatrix} 0 & 1 \\ 0 & 0 \end{pmatrix}$ or $S = \begin{pmatrix} 0 & 0 \\ 1 & 0 \end{pmatrix}$.

It should be noted that in both cases of isolation the scattering matrix is defective as discussed in chapter 1

2.5 Time-reversibility, Non-Reciprocity and Unitarity

The ideas of time-reversibility, non-reciprocity and unitarity of a system are closely related to each other. In this chapter we explore the relation between them. Physical systems which possess the property that they are symmetric with respect to inversion of time, are known as time-reversible systems. A time reversal operation exchanges the roles of the incident and scattered waves, and this exchange corresponds to the following property of the scattering matrix [17]:

Definition 2.5.1. A system is time-reversible if $S^* = S^{-1}$, where $*$ denotes complex conjugation.

Now, for a lossless system the incident power must equal the scattered power. In this case the scattering matrix is defined as follows:

Definition 2.5.2. A system is lossless (Unitary) if $S^\dagger = S^{-1}$, where \dagger denotes Hermitian conjugation.

Theorem 2.5.1. *If a system is time reversible and lossless, it is reciprocal.*

Proof. If a system is time reversible, then according to Def. 2.5.1, $S^* = S^{-1}$ and also as the system is lossless, $S^\dagger = S^{-1}$. As both the relations are satisfied, we have $S^* = S^\dagger$ which gives us $S = S^T$. However, this is the form of the scattering matrix for a reciprocal system according to Def. 2.3.1. Therefore, if a system is time reversible and lossless, it is reciprocal. \square

We should note however, that the reverse is not true. There are systems which are lossy, but are reciprocal [16]. A simple example would be a system which equally attenuates amplitudes of the electromagnetic wave in forward and backward direction, in that $S^\dagger \neq S^{-1}$ but $S = S^T$. Such systems are also time irreversible, which can be easily derived.

Theorem 2.5.2. *When a system is lossless ($S^\dagger = S^{-1}$) and it is also non-reciprocal ($S \neq S^T$), then it has to be time reversal asymmetric ($S^* \neq S^{-1}$)*

Proof. As the system is lossless, the scattering matrix follows ($S^T = S^{*,-1}$). We just manipulated the complex conjugation to take it on the right hand side. Now, as the system is non-reciprocal $S^T \neq S$. Combining the relations we get $S^{*,-1} \neq S$ which gives us the relation $S^* \neq S^{-1}$. However, according to the Def. 2.5.1, this means the system is time irreversible. This is in fact derived in [16]. \square

2.5.1 Non-Reciprocity and Thermodynamics

Initially, it may appear that a device enabling the passage of light in a single direction contradicts the second law of thermodynamics. This is because it seemingly allows light energy to move from a colder object to a hotter one while blocking its flow in the opposite direction. However, this violation is usually misunderstood. In fact, an isolator (non-reciprocal) system is not closed, the energy is either redirected to some another port (consider a 3-port circulator, for example) or emitted into the environment. Suppose we consider a 3-port circulator, a part of it can be considered as a non-reciprocal device (port 1 and 2), where the mode is redirected to port 3. An example of complete scattering matrix of an isolator (the red part) in such a case is

$$\begin{pmatrix} \textcolor{red}{0} & \textcolor{red}{1} & 0 \\ \textcolor{red}{0} & \textcolor{red}{0} & 1 \\ 1 & 0 & 0 \end{pmatrix}, \quad (2.26)$$

where the first 2×2 submatrix corresponds to the port 1 and port 2.

2.6 Applications of non-reciprocity of light

There are many applications of non-reciprocity of light. Let us enlist a few. The applications can be found in Chapter 13 of [18], Chapter 9 of [19], and in [20, 21, 22, 23, 24, 25]

- **Quantum Metrology:** Non-reciprocal light-matter interactions can be used to enhance the sensitivity and precision of quantum metrology applications. Quantum metrology aims to measure physical quantities with high precision beyond classical limits. Non-reciprocal effects can be employed to create non-reciprocal interferometers or to enhance the sensitivity of sensing schemes by exploiting the asymmetric behavior of light propagation.
- **Optical Communications:** Non-reciprocal devices play a crucial role in optical communication systems. Optical isolators, which allow light to transmit in one direction while blocking it in the opposite direction, prevent signal reflections and ensure efficient and reliable data transmission. Non-reciprocal components such as Faraday rotators and circulators are commonly used in optical fiber networks and other communication systems.
- **Laser Systems:** Non-reciprocal elements are essential for the stable operation of laser systems. Laser cavities often incorporate optical isolators to prevent back-reflections from disrupting the laser's output. By allowing light to propagate only in one direction, these devices maintain the laser's stability and prevent unwanted feedback.
- **Microwave Engineering:** Non-reciprocal devices find applications in microwave engineering and radiofrequency systems. Non-reciprocal components such as circulators and isolators are used in radar systems, satellite communication, and wireless technologies. They enable the efficient control and management of microwave signals in complex transmission and reception systems.
- **Antennas and Antenna Arrays:** Non-reciprocity can be leveraged in antenna designs to enhance their performance. By incorporating non-reciprocal components or techniques, antenna arrays can achieve improved signal transmission and reception characteristics, such as enhanced directivity, improved impedance matching, and reduced interference.

These are just a few examples of the applications of non-reciprocity of light. The use of non-reciprocal devices and systems extends across multiple domains, including telecommunications, laser technology, microwave engineering, sensing, and more.

2.7 Optomechanical Non-Reciprocity

Let us understand another example of non-reciprocal device in this section. Optomechanical nonreciprocity is a phenomenon in which the interaction between light and mechanical motion exhibits a directional dependence, breaking the principle of reciprocity. Devices which implement optomechanical non-reciprocity are known as "optomechanical isolators" (or OM isolators). These isolators offer several advantages compared to Faraday isolators, which are traditionally used for optical isolation, e.g.,

- **Compactness and Integration:** OM isolators can be designed in a compact form factor, allowing for easy integration into various optical systems. They can be fabricated using micro- or nanofabrication techniques, enabling on-chip integration with other photonic components. In contrast, Faraday isolators typically consist of bulky magneto-optical materials and strong magnetic fields, making them larger and less amenable to integration.
- **Low Optical Loss:** OM isolators can achieve low insertion loss, minimizing the loss of optical power during transmission. The direct mechanical modulation of the optomechanical interaction allows for efficient control of the transmission and isolation without significant loss. In contrast, Faraday isolators inherently introduce some level of insertion loss due to the polarization rotation induced by the magneto-optical effect.
- **High Isolation Ratio:** OM isolators can provide high isolation ratios, effectively blocking light from propagating in the reverse direction. The directional dependence of the optomechanical interaction allows for efficient suppression of back-reflections, preventing them from interfering with the desired optical signals. Faraday isolators also offer high isolation, but their performance can be limited by factors such as polarization-dependent losses and temperature variations.
- **Compatibility with Non-Magnetic Environments:** OM isolators do not rely on magnetic fields or magneto-optical materials for their operation. This makes them suitable for applications in non-magnetic environments or in situations where magnetic fields are undesirable or impractical. Faraday isolators, on the other hand, require magnetic fields and can be sensitive to external magnetic interference.

While OM isolators offer these advantages, it is important to note that Faraday isolators still have their own strengths and are widely used in many applications. They are especially well-suited for high-power and high-extinction-ratio applications, where their robustness and polarization-dependent characteristics are advantageous. OM isolators also have their disadvantages which we will discuss in later section. Nonetheless, the unique features of OM isolators make them an attractive alternative, particularly for compact and integrated optical systems that require low optical loss.

2.7.1 Cavity Optomechanics

Optomechanics is an interdisciplinary field of research that combines the principles of optics and mechanics to study the interaction between light and mechanical systems Figure 2.4. It explores the intricate interplay between the motion of mechanical objects and the behavior of light, enabling the manipulation and control of mechanical systems through optical means.

In optomechanical systems, light interacts with the mechanical motion of objects, such as nanomechanical resonators or micro-mirrors. This interaction arises from the radiation pressure exerted by light, which can induce mechanical motion or modulate the mechanical properties of the system. Conversely, the mechanical motion can affect the behavior of light, leading to phenomena such as cavity optomechanics or optomechanically induced transparency.

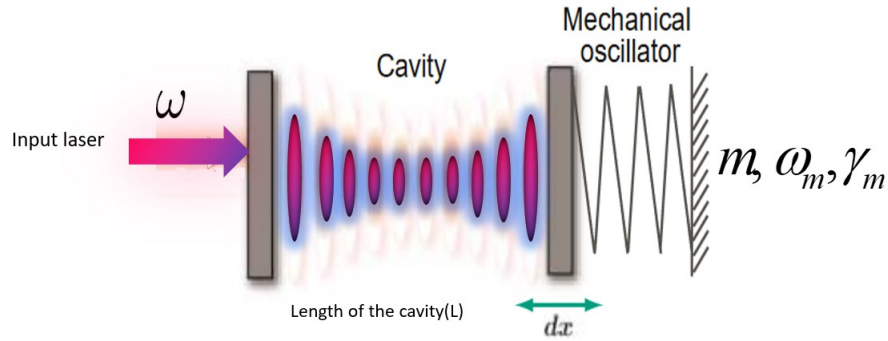


Figure 2.4: Schematic diagram of an optomechanical setup. It contains an input laser driving of frequency ω (or ω_d). There is a partially reflective fixed mirror and a movable, completely reflective mirror. We call it as mechanical oscillator, which has a mass m , natural frequency ω_m and dissipative constant γ_m . The length of the cavity is L and the displacement of the moving mirror from its equilibrium position is x .

One of the fundamental ingredients in optomechanics is the optomechanical coupling, which describes the strength of the interaction between light and mechanical motion. This coupling can be enhanced by using devices with high-quality factors (Q factors) [26, 27] or by engineering structures that have strong light confinement. By manipulating the optomechanical coupling, researchers can achieve a wide range of effects, including cooling of mechanical resonators to their quantum ground state, amplification or control of mechanical motion, and even the generation of squeezed or entangled states of light.

These systems involve a Fabry-Perot cavity comprising two mirrors. One of the mirrors remains fixed and has partial transparency, while the other mirror is highly reflective and capable of moving around its equilibrium position. We introduce a laser field to the fixed and transmittive mirror, leading to the presence of circulating photons within the cavity. These photons exert a pressure on the movable mirror, and the force experienced by the mirror depends on the number of photons within the cavity.

The equilibrium position of the movable mirror undergoes a shift due to the radiation pressure from the laser field, causing the mirror to oscillate. These oscillations result in a change in the length of the cavity, which, in turn, alters the resonance frequency of the cavity. This change in resonance frequency leads to a variation in the number of photons present within the cavity. A laser, operating at frequency ω_p , passes through a mirror that allows transmission. The cavity mode represents a standing wave with a frequency of ω_c . The length of the cavity when the mirror is at rest is denoted by L . The natural frequency of the moving mirror is represented by ω_m . The mass of the moving mirror is denoted by m . The size of the zero-point fluctuation of the mirror is given by $x_{zpt} = \sqrt{\frac{\hbar}{m\omega_m}}$. Suppose

the movable mirror is fixed, the optomechanical system is like a Fabry Perot cavity and the Hamiltonian for such a system is simply given as

$$H_c = \hbar\omega_c \hat{a}^\dagger \hat{a} , \quad (2.27)$$

where \hat{a} and \hat{a}^\dagger are the annihilation and the creation operators, respectively, ω_c is the resonant frequency of the cavity. Now, as the second mirror is movable, its Hamiltonian will be that of a mechanical oscillator, given by

$$H_m = \frac{\hat{p}^2}{2m} + \frac{1}{2}\omega_m^2 \hat{x}^2 , \quad (2.28)$$

where we can define the momentum operator \hat{p} and position operator \hat{x} in terms of annihilation and creation operators of mechanical oscillator (\hat{b} and \hat{b}^\dagger) as

$$\hat{x} = \sqrt{\frac{\hbar}{2m\omega_m}}(\hat{b} + \hat{b}^\dagger) , \quad (2.29)$$

and

$$\hat{p} = -i\sqrt{\frac{2m\omega_m}{\hbar}}(\hat{b} - \hat{b}^\dagger) . \quad (2.30)$$

Using the above definition, the Hamiltonian of the mechanical oscillator can be rewritten as

$$H_m = \hbar\omega_m \hat{b}^\dagger \hat{b} . \quad (2.31)$$

The total Hamiltonian of the optomechanical system is however incomplete without considering the effect of radiation pressure force from the cavity field on the mechanical oscillator. The resonant frequency of the cavity in terms of the length of the cavity L is given as

$$\omega_c = \frac{2\pi nc}{L} , \quad (2.32)$$

where c is speed of light in vacuum, $n = 1, 2, 3, \dots$ is the mode number of the resonance of the cavity field inside the cavity. The radiation pressure exerted on the mirror induces its displacement, leading to a change in the length of the cavity from L to $L + x$. This now affects ω_c and it becomes dependent on the position of the second mirror. Therefore,

$$\omega_c(x) = \frac{2\pi nc}{L + x} . \quad (2.33)$$

As the radiation pressure is negligible, the displacement x is much smaller than L and we can expand the above expression using the Taylor's series as

$$\omega_c(x) = \frac{2\pi nc}{L + x} = \frac{2\pi nc}{L} \left(1 - \frac{x}{L}\right) = \omega_c - \frac{\omega_c}{L} \hat{x} = \omega_c - \frac{\omega_c}{\sqrt{2}L} x_{zpt} (\hat{b} + \hat{b}^\dagger) . \quad (2.34)$$

We have used Equation 2.30 and the definition of x_{zpt} .

Then Equation 2.33 modifies the Equation 2.27 to

$$H_c = \hbar\omega_c \hat{a}^\dagger \hat{a} - \hbar g_0 (\hat{b} + \hat{b}^\dagger) \hat{a}^\dagger \hat{a} , \quad (2.35)$$

where g_0 , as given below, is known as single-photon "optomechanical coupling" constant.

$$g_0 = \frac{\omega_c}{\sqrt{2}L} x_{zpt} = \sqrt{\frac{\hbar}{2m\omega_m} \frac{\omega_c}{L}}. \quad (2.36)$$

The above parameter g_0 has dimensions of frequency and can be used to compare other frequencies in the system.

Moreover, if the system is driven by an input laser field, the Hamiltonian of the laser term with driving field frequency ω_d is

$$H_l = -i\hbar (\epsilon^* e^{i\omega_d t} \hat{a} - \epsilon e^{-i\omega_d t} \hat{a}^\dagger), \quad (2.37)$$

where $\epsilon = \sqrt{\frac{2\kappa P}{\hbar\omega_p}}$ is the coupling strength between laser and optical mode, P is the power of the driving field and κ is the photon decay rate. We can define the κ as

$$\kappa = \frac{\pi c}{2FL}, \quad F = \frac{\pi(1-T)^{1/4}}{1-(1-T)^{1/2}}, \quad (2.38)$$

where F is the finesse of cavity and the T is the transmissivity of the mirror.

Combining all the Hamiltonian parts, Equation 2.35, Equation 2.31 and Equation 2.37 we have the total Hamiltonian of the optomechanical system to be

$$\hat{H} = \hbar\Delta_c \hat{a}^\dagger \hat{a} + \hbar\omega_m \hat{b}^\dagger \hat{b} - \hbar g_0 (\hat{b} + \hat{b}^\dagger) \hat{a}^\dagger \hat{a} - i\hbar (\epsilon^* e^{i\omega_d t} \hat{a} - \epsilon e^{-i\omega_d t} \hat{a}^\dagger). \quad (2.39)$$

Let us now understand the setup of a generic optomechanical isolator.

2.7.2 Generic Optomechanical Isolator

We learnt about a simple optomechanical setup in previous section. Let us now understand, how such systems, where there can be coupling between optical and mechanical parts, can be used to create the phenomenon of isolation. In this context, we will need to modify the system to be that of a "membrane-in-middle" (MIM) setup, as shown in Figure 2.5. The setup contains two fixed partially reflective mirrors with a dielectric membrane in the middle. The Hamiltonian of the setup with laser driving is slightly modified from the previous Equation 2.39 and is given by

$$\begin{aligned} H = & \omega_1 a_1^\dagger a_1 + \omega_2 a_2^\dagger a_2 + \omega_b b^\dagger b + J(a_1^\dagger a_2 + a_2^\dagger a_1) \\ & + g_1 a_1^\dagger a_1 (b^\dagger + b) + g_2 a_2^\dagger a_2 (b^\dagger + b) \\ & + i[\epsilon_1 e^{-i(\omega_{da,1}t - \phi_1)} a_1^\dagger + \epsilon_2 e^{-i(\omega_{da,2}t - \phi_2)} a_2^\dagger - h.c.], \end{aligned} \quad (2.40)$$

where a_i ($i = 1, 2$) represents intracavity optical mode of the either side of the membrane, with the corresponding fundamental frequency ω_i , when the membrane is fully reflective. These modes couple with the mechanical mode b with the corresponding optomechanical coupling constants g_i . In addition, the term with J describes the direct coupling between these two cavity modes, arising due to tunneling through the membrane. The i th cavity mode is driven by a field of amplitude ϵ_i , frequency $\omega_{da,i}$ and phase ϕ_i .

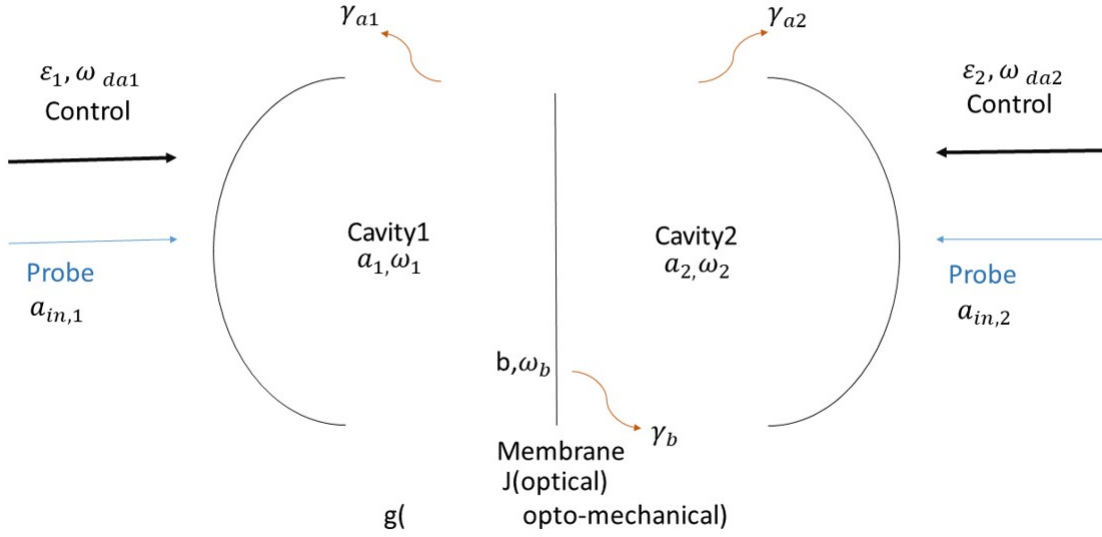


Figure 2.5: Schematic diagram of membrane in the middle setup for optomechanical isolation. The physical setup consists of a cavity optomechanical system with linear optomechanical coupling, along with a time-harmonic mechanical drive for the membrane. The $a_{in,1}$ is the annihilation operator of the probe or input field entering into the cavity coupling to its i th mode. The other notations are explained after the Equation 2.40.

Upon rotating the frame with respect to the driving field frequency $\omega_{da,i}$, we get the modified version of the Hamiltonian:

$$\begin{aligned}
H' = & \Delta_1 a_1^\dagger a_1 + \Delta_2 a_2^\dagger a_2 + \omega_b b^\dagger b + J(a_1^\dagger a_2 + a_2^\dagger a_1) \\
& + g_1 a_1^\dagger a_1 (b^\dagger + b) \\
& + g_2 a_2^\dagger a_2 (b^\dagger + b) \\
& + i \left[\epsilon_1 e^{i\phi_1} a_1^\dagger + \epsilon_2 e^{i\phi_2} a_2^\dagger - h.c. \right] .
\end{aligned} \tag{2.41}$$

Here, $\Delta_i = \omega_i - \omega_{da,i}$ ($i \in 1, 2$) are the detunings. In deriving the above Hamiltonian, we have used the following transformation: upon the transformation $H' = U H U^\dagger - i U \frac{\partial U^\dagger}{\partial t}$, where $U = \exp[i(\omega_{da,1} t a_1^\dagger a_1 + \omega_{da,2} t a_2^\dagger a_2)]$.

By inserting the Hamiltonian (Equation 2.41) into the Heisenberg equation, while considering the effects of damping and associated noise terms, we arrive at the quantum Langevin equations (QLEs) governing the behavior of the optical and mechanical motion operators.

$$\begin{aligned}
\frac{d}{dt} a_1 = & \left\{ -\frac{\gamma_1}{2} - i[\Delta'_1] \right\} a_1 - iJ a_2 \\
& + \epsilon_1 e^{i\phi_1} + \sqrt{\gamma_1} a_{in,1} ,
\end{aligned} \tag{2.42}$$

$$\begin{aligned}
\frac{d}{dt} a_2 = & \left\{ -\frac{\gamma_2}{2} - i[\Delta'_2] \right\} a_2 - iJ a_1 \\
& + \epsilon_2 e^{i\phi_2} + \sqrt{\gamma_2} a_{in,2} ,
\end{aligned} \tag{2.43}$$

$$\begin{aligned}
\frac{d}{dt} b = & \left(-\frac{\gamma_b}{2} - i\omega_m \right) b \\
& - i(g_1 a_1^\dagger a_1 + g_2 a_2^\dagger a_2) + \sqrt{\gamma_b} b_{in} .
\end{aligned} \tag{2.44}$$

where γ_i and (γ_b) are the damping rates of the i th optical mode a_i and the mechanical mode b . The input quantum fields with zero mean values are a_{in} and b_{in} .

When the control field amplitude is significantly greater than the probe field amplitude, in what is known as the strong driving limit, we can make the factorization assumption. This assumption involves separating any two annihilation operators a and c , while calculating their joint expectation values, as $\langle ac \rangle = \langle a \rangle \langle c \rangle$. Under this assumption, the average number of excitations in the cavity modes and the membrane can be determined at the steady state.

$$\begin{aligned}
\langle a_1 \rangle = \alpha_1 = & \frac{\left(\frac{\gamma_2}{2} + i\Delta_2'' \right) \epsilon_1 e^{i\phi_1} - iJ \epsilon_2 e^{i\phi_2}}{\left(\frac{\gamma_1}{2} + i\Delta_1'' \right) \left(\frac{\gamma_2}{2} + i\Delta_2'' \right) + J^2} , \\
\langle a_2 \rangle = \alpha_2 = & \frac{\left(\frac{\gamma_1}{2} + i\Delta_1'' \right) \epsilon_2 e^{i\phi_2} - iJ \epsilon_1 e^{i\phi_1}}{\left(\frac{\gamma_1}{2} + i\Delta_1'' \right) \left(\frac{\gamma_2}{2} + i\Delta_2'' \right) + J^2} , \\
\langle b \rangle = \beta = & \frac{-i(g_1 |\alpha_1|^2 + g_2 |\alpha_2|^2)}{\left(\frac{\gamma_b}{2} + i\omega_m \right)} .
\end{aligned} \tag{2.45}$$

where $\Delta_1'' = \Delta_1 + g_1(\beta + \beta^*)$ and $\Delta_2'' = \Delta_2 + g_2(\beta + \beta^*)$ are the effective detuning which includes frequency shifts caused by the optomechanical interaction.

To solve the Equation 2.43 to Equation 2.44, we linearize the equations in strong driving condition ($\epsilon_1 \gg \gamma_1$ and $\epsilon_2 \gg \gamma_2$). We can then write the operators as sum of mean values

and small quantum fluctuation terms i.e. $a_1 = \alpha_1 + \delta a_1$, $a_2 = \alpha_2 + \delta a_2$ and $b = \beta + \delta b$. Substituting them into the Equation 2.43 to Equation 2.44 and keeping only the first order terms in the quantum fluctuations ($\delta a_1, \delta a_2, \delta b$), we obtain the quantum Langevin equations:

$$\begin{aligned} \frac{d}{dt}\delta a_1 &= \left(-\frac{\gamma_1}{2} - i\Delta_1''\right)\delta a_1 - iG_1(\delta b + \delta b^\dagger) \\ &\quad - iJ\delta a_2 + \sqrt{\gamma_1}a_{\text{in},1} , \end{aligned} \quad (2.46)$$

$$\begin{aligned} \frac{d}{dt}\delta a_2 &= \left(-\frac{\gamma_2}{2} - i\Delta_2''\right)\delta a_2 - iG_2(\delta b + \delta b^\dagger) \\ &\quad - iJ\delta a_1 + \sqrt{\gamma_2}a_{\text{in},2} , \end{aligned} \quad (2.47)$$

$$\begin{aligned} \frac{d}{dt}\delta b &= \left(-\frac{\gamma_b}{2} - i\omega_m\right)\delta b - i(G_1\delta a_1^\dagger + G_1^*\delta a_1) \\ &\quad - i(G_2\delta a_2^\dagger + G_2^*\delta a_2) + \sqrt{\gamma_b}b_{\text{in}} . \end{aligned} \quad (2.48)$$

where $G_1 = g_1\alpha_1 = |G_1|e^{i\theta_1}$ and $G_2 = g_2\alpha_2 = |G_2|e^{i\theta_2}$ are the effective optomechanical coupling rates with phase difference $\theta = \theta_2 - \theta_1$. These phases can be easily related to those ϕ_i of the driving fields, and hence controllable using the driving field.

The equations Equation 2.47 to Equation 2.48 can be solved in Fourier domain. We first write them in the index notation,

$$\dot{V}_i = -M_{ij}V_j + \Gamma_{ij}V_{j,\text{in}} , \quad (2.49)$$

where $i, j = 1, 2, \dots, 2n$ ($n = 3$ being the number of distinct modes in the system, namely, $a_{1,2}$ and b). Here the elements of fluctuation and input field vectors are arranged as $V = \left(\delta a_1, \delta a_2, \delta b, \delta a_1^\dagger, \delta a_2^\dagger, \delta b^\dagger\right)^T$ and $V_{\text{in}} = \left(a_{\text{in},1}, a_{\text{in},2}, b_{\text{in}}, a_{\text{in},1}^\dagger, a_{\text{in},2}^\dagger, b_{\text{in}}^\dagger\right)^T$, respectively. The matrix Γ is given by

$$\text{diag}(\sqrt{\gamma_1}, \sqrt{\gamma_2}, \sqrt{\gamma_b}, \sqrt{\gamma_1}, \sqrt{\gamma_2}, \sqrt{\gamma_b}) . \quad (2.50)$$

By introducing the Fourier transform of any arbitrary operator \hat{o} , as

$$\tilde{o}(\omega) = \frac{1}{\sqrt{2\pi}} \int_{-\infty}^{+\infty} o(t)e^{i\omega t} dt , \quad (2.51)$$

$$\tilde{o}(\omega)^\dagger = \frac{1}{\sqrt{2\pi}} \int_{-\infty}^{+\infty} o(t)^\dagger e^{i\omega t} dt , \quad (2.52)$$

and by using the properties of Fourier transformation, we can find the solution to the quantum Langevin equations (Equation 2.49), in frequency domain, given by

$$\tilde{V}_i(\omega) = (M - i\omega I)_{ij}^{-1} \Gamma_{jk} \tilde{V}_{\text{in},k}(\omega) , \quad (2.53)$$

where I is the identity matrix. According to the input-output formalism [28], the relationship between internal, input and output fields under the first Markov approximation is given as

$$o_{\text{out}} + o_{\text{in}} = \sqrt{\gamma_o}\delta o , \quad (2.54)$$

where, $o \equiv a_1, a_2, b$ and the γ_o are the damping rates for the respective o . The output field vector in the frequency domain is then given by

$$\tilde{V}_{\text{out},i}(\omega) = \sum_{l=1}^{2n} U_{i,l} \tilde{V}_{\text{in},l}(\omega) , \quad (2.55)$$

where

$$U_{i,l} = [\Gamma_{ij}(M - i\omega I)_{jk}^{-1}\Gamma_{kl} - \delta_{il}] , \quad (2.56)$$

$$\tilde{V}_{\text{out}} = \left(a_{\text{out},1}, a_{\text{out},2}, b_{\text{out}}, a_{\text{out},1}^\dagger, a_{\text{out},2}^\dagger, b_{\text{out}}^\dagger \right)^T . \quad (2.57)$$

To obtain the spectrum of scattering probabilities, we now invoke the two-frequency correlation of various elements of the V -matrices. Let us start with

$$\tilde{V}_{\text{out},i}^\dagger \tilde{V}_{\text{out},j} = \sum_{l,m=1}^{2n} U_{i,l}^* U_{j,m} \tilde{V}_{\text{in},l}^\dagger \tilde{V}_{\text{in},m} . \quad (2.58)$$

Now, as $\langle \tilde{V}_{\text{in},i}^\dagger \tilde{V}_{\text{in},j} \rangle$ are non-zero only for $i = j$, we find that

$$\langle \tilde{V}_{\text{out},i}^\dagger \tilde{V}_{\text{out},j} \rangle = \sum_{l=1}^{2n} U_{i,l}^* U_{j,l} \langle \tilde{V}_{\text{in},l}^\dagger \tilde{V}_{\text{in},l} \rangle . \quad (2.59)$$

Defining $S_{i,\text{out}}(\omega) = \int d\omega' \langle \tilde{V}_{\text{out},i}^\dagger(\omega') \tilde{V}_{\text{out},i}(\omega) \rangle$ and $S_{i,\text{in}}(\omega) = \int d\omega' \langle \tilde{V}_{\text{in},i}^\dagger(\omega') \tilde{V}_{\text{in},i}(\omega) \rangle$ ($i \in 1, 2, 3$), we now obtain following expression, relating the frequency correlations at the input and output ports:

$$S_{\text{out}}(\omega) = T(\omega) S_{\text{in}}(\omega) + S_{\text{vac}}(\omega) , \quad (2.60)$$

where S_{in} , S_{out} , and $S_{\text{vac}}(\omega) = (s_{a1,\text{vac}}(\omega), s_{a2,\text{vac}}(\omega), s_{b,\text{vac}}(\omega))^T$ are the n -component column matrices. The T denotes the scattering probability matrix.

The element T_{ij} of this matrix represents the probability to scatter from the i th mode to the j th mode, and is given by

$$T_{ij} = |U_{i,j}|^2 + |U_{i,j+n}|^2 , \quad (2.61)$$

for $i, j \in 1, 2, 3$. Similarly, the elements of $S_{\text{vac}}(\omega)$ can be written in terms of the elements of the U -matrix, as

$$S_{i,\text{vac}}(\omega) = |U_{i,i+n}(\omega)|^2 + |U_{i,i+n+1}(\omega)|^2 + \dots + |U_{i,i+2n}(\omega)|^2 . \quad (2.62)$$

In Figure 2.6 we display the variation of the scattering probabilities T with respect to ω/γ (Ratio of the signal frequency and the damping rate). Here, T_{12} represents scattering probability from mode a_1 to a_2 and T_{21} represents the vice-versa. One of them reaching zero and the other reaching 1 simultaneously for same parameters gives rise to isolation. The scattering matrix in this case is that of Equation 2.25 or the other. Specifically, optical isolation occurs for $\theta = (2k + 1)\pi/2$, for all integers k , while for $\theta \equiv \pi/2 \pmod{2\pi}$, the transmission vanishes from the mode a_1 to a_2 and for $\theta \equiv 3\pi/2 \pmod{2\pi}$, the reverse situation is achieved. This asymmetry in transmission profile can be understood in terms of interference phenomenon which will be discussed in later section. The signal frequency ω also needs to exactly match the natural frequency of the membrane (or the mechanical oscillator) ω_m .

Definition 2.7.1. The signal frequency at which isolation occurs is known as “isolation” (or central) frequency.

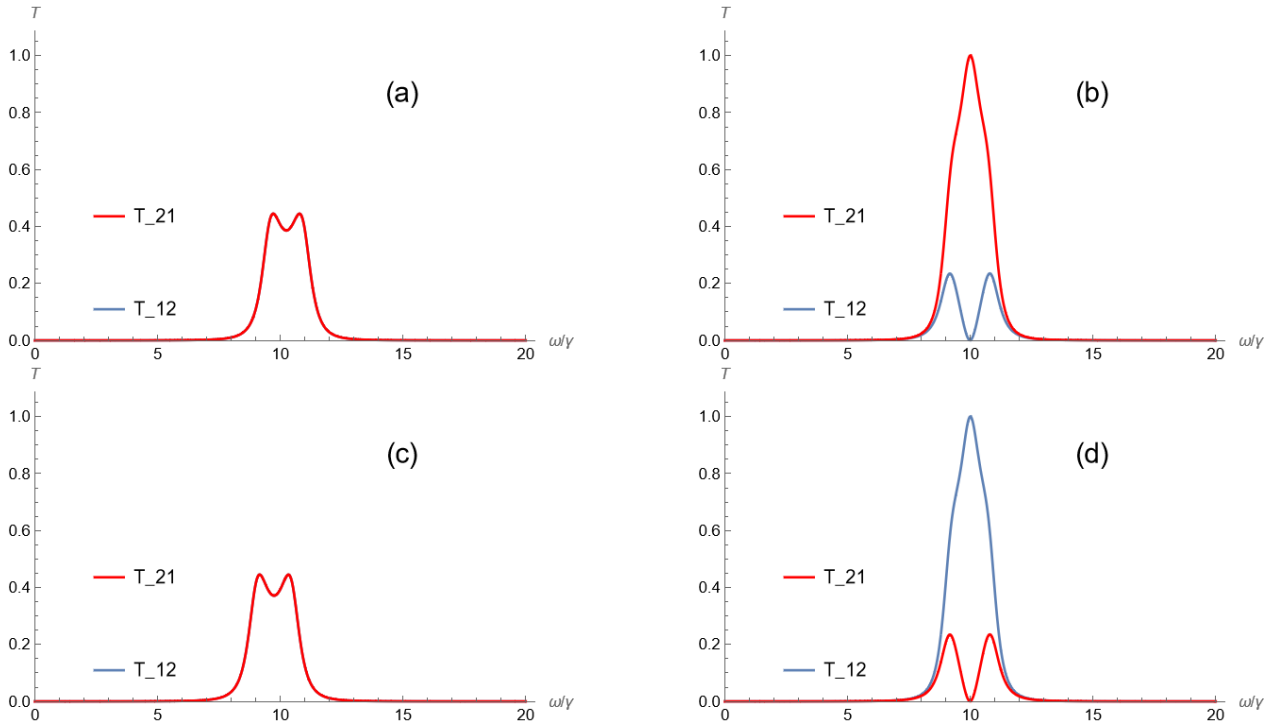


Figure 2.6: Plot for the scattering probabilities (T) with respect to normalized input frequency ω/γ for various θ . T_{12} (blue), T_{21} (red), (a) $\theta = 0$, (b) $\theta = \pi/2$, (c) $\theta = \pi$ and (d) $\theta = 3\pi/2$. The other parameters chosen are $J = |G_1| = |G_2| = \gamma_1/2 = \gamma_2/2 = \gamma_b/2 = \gamma/2$ and $\omega_m = \Delta'_1 = \Delta'_2 = \Delta = 10\gamma$. Plots (b) and (d) showcase the isolation feature in opposite directions. Moreover, it is to be noted the isolation occurs exactly at the signal frequency $\omega = 10\gamma$, which is the mechanical oscillators natural frequency (ω_m). This means that the isolation frequency of the isolator is fixed according to the natural frequency of the mechanical oscillator.

The role of the phase of modified optomechanical coupling is very well explained in [29]. Note that we have used a parameter domain, as $\Delta = \omega_m = 10\gamma$; $J, g = \gamma/2$, satisfying a large detuning limit $\Delta \gg J, \gamma, g$. Hence, from Equation 2.45, we have, for $\epsilon_1 = \epsilon_2 = \epsilon$,

$$\begin{aligned}\alpha_1 &\approx \frac{\Delta\epsilon}{D} e^{i(\phi_1 + \pi/2 - \zeta)}, \\ \alpha_2 &\approx \frac{\Delta\epsilon}{D} e^{i(\phi_2 + \pi/2 - \zeta)}.\end{aligned}\tag{2.63}$$

Here, the denominator in the expressions of α_1 and α_2 [see Eqs. (Equation 2.45)] is written as $De^{i\zeta}$, and the phase $\pi/2$ appears in the numerator. Clearly, the phase difference between α_1 and α_2 is given by $\phi_1 - \phi_2$. This is exactly the same as $\theta_1 - \theta_2$, as used in the expressions of the effective optomechanical coupling: $G_1 = (g\beta)\alpha_1 = |G_1|e^{i\theta_1}$ and $G_2 = (g\beta)\alpha_2 = |G_2|e^{i\theta_2}$, while the optomechanical coupling g is a real quantity. The driving fields therefore create an effective phase-difference in the optomechanical couplings, which in turn, leads to non-reciprocity.

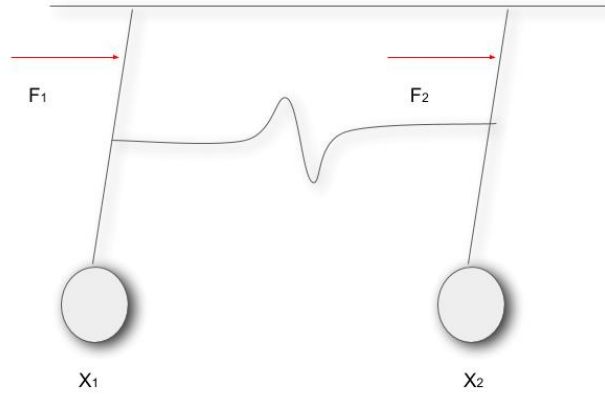


Figure 2.7: A schematic diagram of a coupled pendulum with driving forces $F_1 \cos(\omega_{d1}t + \phi_1)$ and $F_2 \cos(\omega_{d2}t + \phi_2)$.

2.7.3 OM non-reciprocity and Anti-resonance

Usually, a pair of simple pendulums (each of angular frequency ω), linearly coupled with the corresponding constant g can have two independent eigenmodes of oscillation - the in-phase mode at a frequency ω and the out-of-phase mode at a frequency $\sqrt{\omega^2 + g^2}$. The intensity spectrum of such a system therefore exhibits a doublet, with a peak separation $\sim g$ in weak coupling limit.

Anti-resonance occurs when one of these pendulums is driven by an oscillating field. The amplitude spectrum of the driven oscillator exhibits a deep minimum at a frequency half-way between the two normal-mode frequencies. More importantly, this is associated with a sharp change in phase across this anti-resonance point.

Here we consider both the pendulums to be driven with oscillating fields [see Fig. 2.7]. Generalizing to the case, when the pendulums are of different natural frequencies ω_1 and ω_2 , we can write down the corresponding equations of motion of the amplitudes x_i of these pendulums, as follows:

$$\begin{aligned} \ddot{x}_1 + \gamma_1 \dot{x}_1 - 2g\omega_1 x_2 + \omega_1^2 x_1 &= 2F_1 \cos(\omega_{d,1}t - \phi_1) , \\ \ddot{x}_2 + \gamma_2 \dot{x}_2 - 2g\omega_2 x_1 + \omega_2^2 x_2 &= 2F_2 \cos(\omega_{d,2}t - \phi_2) , \end{aligned} \quad (2.64)$$

where, γ_i denotes the damping rate of the i th pendulum ($i \in 1, 2$), the g denotes the coupling constant between the two pendulums, and F_i denotes the amplitude of the i th driving force with frequency $\omega_{d,i}$ and phase ϕ_i .

These equations (Equation 2.64) involve second-order derivatives of x_i 's. Next, we choose a suitable change of variables as $\alpha_1 = \omega_1 x_1 + i\dot{x}_1$ and $\alpha_2 = \omega_2 x_2 + i\dot{x}_2$. Assuming that the driving fields have the same frequencies, i.e., $\omega_{d,1} = \omega_{d,2} = \omega_d$ and making a transformation

to the rotating frame with respect to the driving field frequency ω_d , i.e., $\alpha_i \rightarrow \alpha_i e^{-i\omega_d t}$, we get

$$\begin{aligned}\dot{\alpha}_1 &= -i\Delta_1\alpha_1 - \gamma_1/2(\alpha_1 - \alpha_1^* e^{2i\omega_d t}) - i\frac{g\omega_1}{\omega_2}(\alpha_2 + \alpha_2^* e^{2i\omega_d t}) \\ &\quad + iF_1(e^{i\phi_1} + e^{-2i\omega_d t}e^{-i\phi_1}), \\ \dot{\alpha}_2 &= -i\Delta_2\alpha_2 - \gamma_2/2(\alpha_2 - \alpha_2^* e^{2i\omega_d t}) - i\frac{g\omega_2}{\omega_1}(\alpha_1 + \alpha_1^* e^{2i\omega_d t}) \\ &\quad + iF_2(e^{i\phi_2} + e^{-2i\omega_d t}e^{-i\phi_2}).\end{aligned}\tag{2.65}$$

Neglecting the counter-rotating terms containing $e^{2i\omega_d t}$ (which corresponds to using the rotating wave approximation), we get the final set of equations, as follows:

$$\begin{aligned}\dot{\alpha}_1 &= i(-\Delta_1 + i\gamma_1/2)\alpha_1 - i\frac{g\omega_1}{\omega_2}\alpha_2 + F_1e^{i\phi_1}, \\ \dot{\alpha}_2 &= i(-\Delta_2 + i\gamma_2/2)\alpha_2 - i\frac{g\omega_2}{\omega_1}\alpha_1 + F_2e^{i\phi_2},\end{aligned}\tag{2.66}$$

where a transformation $\phi_i \rightarrow \phi_i + \pi/2$ is considered and $\Delta_i = \omega_i - \omega_d$ is the detuning of the i th pendulum from the driving field.

In steady state, i.e., when $\dot{\alpha}_1 = \dot{\alpha}_2 \approx 0$, the steady state values of the $\alpha_i = \alpha_{i,ss}$ can be found as

$$\begin{aligned}\alpha_{1,ss} &= \frac{(\gamma_2/2 + i\Delta_2)F_1e^{i\phi_1} - igF_2e^{i\phi_2}}{(\gamma_1/2 + i\Delta_1)(\gamma_2/2 + i\Delta_2) + g^2}, \\ \alpha_{2,ss} &= \frac{(\gamma_1/2 + i\Delta_1)F_2e^{i\phi_2} - igF_1e^{i\phi_1}}{(\gamma_2/2 + i\Delta_2)(\gamma_1/2 + i\Delta_1) + g^2}.\end{aligned}\tag{2.67}$$

We note that the amplitudes are complex. Hence, we plot in Figs. 2.8 magnitude and phase spectrum of these steady state amplitudes of the oscillators, where we have chosen $\Delta_i = \Delta$. We see that there is a sharp dip in the amplitude of the first oscillator [Fig. 2.8(c)], that is associated with a singular phase-change of π [Fig. 2.8(d)], when the two driving fields have a phase difference ($\phi_1 - \phi_2 = \pi/2$). This phenomenon is called anti-resonance. Such a spectral feature is clearly analogous to non-reciprocity, in which the energy content of the input mode vanishes and that of the output mode becomes maximum. However, for a given phase-difference $\phi_1 - \phi_2$, one cannot achieve the reverse situation, namely, vanishing (maximum) energy content of the output (input) mode. This means that the system behaves as an isolator. We find that The physics of anti-resonance is discussed in [30, 31], where only one of the oscillators is driven by an external harmonic field.

More importantly, when the phase-difference between the driving fields is changed to $\phi_1 - \phi_2 = -\pi/2$, we see such anti-resonance behavior in the spectrum of the second oscillator, instead of the first one [Figs. 2.8(e) and 2.8(f)]. Such a reversal of the spectral behavior of two oscillators can also be seen in the context of optomechanical nonreciprocity [1, 32], in which such reversal of the directions of the field can be done by changing the phase differences of the two cavity driving fields. These phenomenon are analogous. We emphasize that by driving only one oscillator, the reversal of the spectral behavior cannot be obtained.

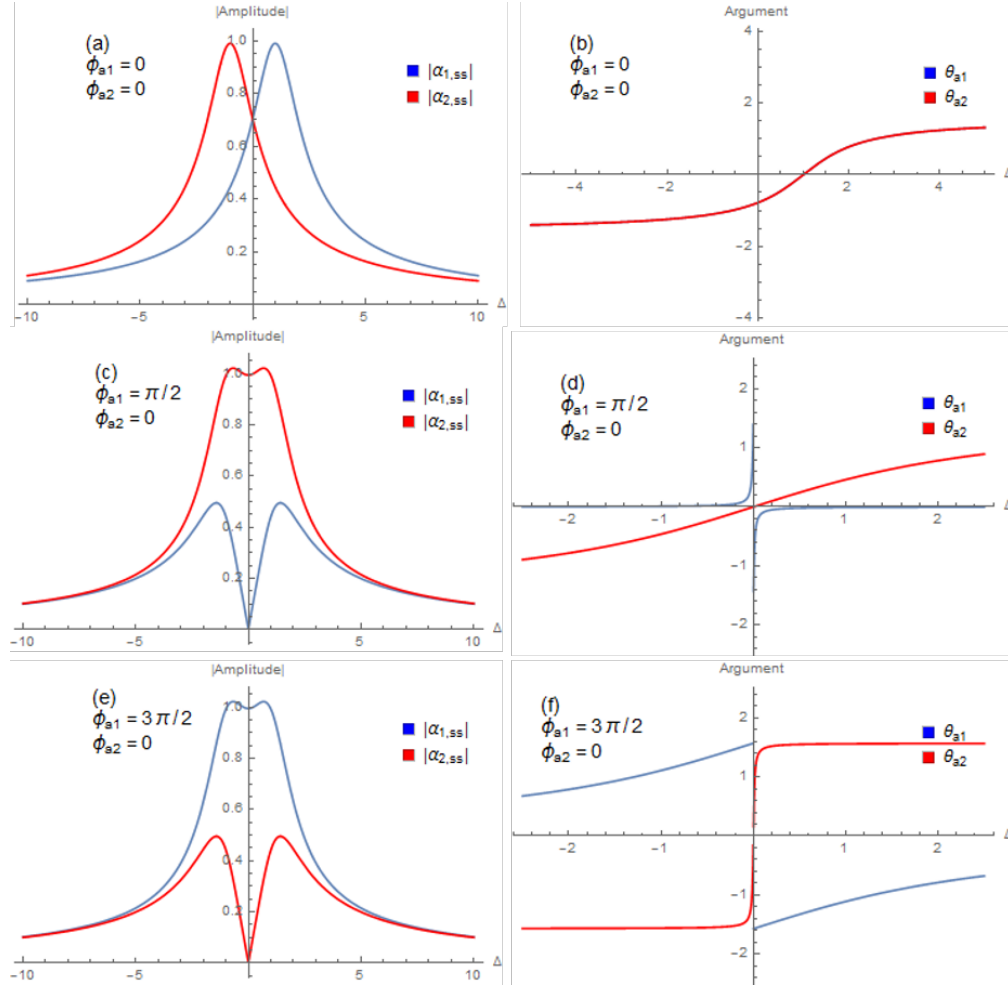


Figure 2.8: Plots (a), (c), (e) on the left panel represent the variation of magnitudes of the $\alpha_{i,ss}$ with respect to Δ for various combinations of ϕ_1 and ϕ_2 . Plots (b), (d), (f) on the right panel represent the phases (argument) of the $\alpha_{i,ss}$ with respect to Δ , corresponding to the same combinations of values of ϕ_1 and ϕ_2 . The other parameters chosen are $\gamma_1 = \gamma_2 = \gamma$, $F_1 = F_2 = \gamma$, and $g = \gamma/2$.

We have outlined how the anti-resonance phenomenon can be analogous to optomechanical nonreciprocity. However the anti-resonance occurs only at a certain frequency $\Delta = 0$ [see Figure 2.8], that depends upon the natural frequency of the mechanical oscillator (ω_i). Analogously, in optomechanical isolators, the isolation occurs only at a certain frequency ([1]) is dependent on natural frequency of the membrane). In such a narrow-band isolator, one is limited with the natural frequency of the membrane itself, that is fixed in a given architecture and cannot be manipulated externally. This means that one does not have any dynamical control to make it useful for isolation at other frequencies.

2.7.4 Issues plaguing OM non-reciprocity

Challenges affecting optomechanical nonreciprocity are:

1. **Imbalanced Coupling:** Achieving nonreciprocal behavior requires a significant difference in the optical and mechanical coupling strengths. However, in practical systems, it can be challenging to maintain a large and stable imbalance in the coupling strengths over a wide range of operating conditions.
2. **Loss and Damping:** Nonreciprocal devices are susceptible to losses and damping, which can degrade the performance and efficiency of optomechanical nonreciprocal effects. Mitigating losses and minimizing damping mechanisms are crucial for achieving robust nonreciprocal behavior.
3. **Thermal Noise:** The presence of thermal noise can limit the effectiveness of nonreciprocal devices. The random thermal fluctuations can introduce noise into the system, reducing the signal-to-noise ratio and affecting the overall performance of optomechanical nonreciprocity.
4. **Frequency and Bandwidth Limitations:** Optomechanical nonreciprocal devices often operate within specific frequency ranges and exhibit limited bandwidth. Expanding the operational bandwidth and achieving nonreciprocity over a broader frequency range remain significant challenges in the field.
5. **Fabrication and Integration:** Fabricating and integrating complex optomechanical structures with precise control over device parameters can be challenging. Ensuring consistent and reliable fabrication techniques while maintaining device performance is crucial for the widespread implementation of optomechanical nonreciprocity.

Addressing these issues requires advancements in fabrication techniques, improved materials, novel device designs, and effective strategies for mitigating losses, noise, and thermal effects in optomechanical systems. In this thesis, we will later present a technique to address the frequency and bandwidth limitations.

2.8 Conclusion

In our exploration, we delved into the phenomenon of non-reciprocity and isolation, focusing on its understanding through scattering matrices. By studying the scattering properties of

systems, we gained insights into the conditions necessary to achieve non-reciprocity of light. This investigation led us to the Lorentz Reciprocity Theorem, which outlines the prerequisites for the realization of non-reciprocity. Moreover, we discovered the intriguing connection between non-reciprocity and thermodynamics, highlighting the thermodynamic aspects underlying the phenomenon. Expanding our knowledge, we examined the Faraday isolator, a device commonly used to achieve non-reciprocal light transmission. Additionally, we explored an optomechanical isolator configuration that employs a membrane positioned in the middle, leveraging optomechanical interactions. Throughout our exploration, we encountered challenges and limitations associated with optomechanical isolators, gaining a comprehensive understanding of the issues that currently impact their practical implementation.

Chapter 3

Non-Hermitian Quantum Sensing

Non-Hermitian quantum sensing [33, 34, 35, 36, 37, 38] is a fascinating and emerging field within quantum physics that explores the use of non-Hermitian systems for sensitive measurements and sensing applications. Traditionally, Hermitian Hamiltonians, which correspond to observable quantities in quantum mechanics, have been the cornerstone of quantum sensing. However, recent developments have shown that non-Hermitian systems can offer unique advantages in terms of sensitivity, precision, and robustness in certain sensing scenarios.

In quantum mechanics, Hermitian operators represent physical observables, such as position, momentum, and energy, and their corresponding eigenvalues represent the possible outcomes of measurements. Hermiticity ensures that the eigenvalues are real, reflecting physically measurable quantities. However, in non-Hermitian systems, the Hamiltonian matrix is not Hermitian, meaning it does not satisfy the condition $H^\dagger = H$, where H^\dagger denotes the Hermitian conjugate of H .

Non-Hermitian quantum sensing harnesses the distinctive properties of non-Hermitian systems, such as the presence of complex eigenvalues and non-orthogonal eigenvectors, to enable novel sensing strategies. One intriguing aspect of non-Hermitian systems is the concept of exceptional points (EPs). An exceptional point occurs when two or more eigenvalues and their corresponding eigenvectors coalesce, leading to a nontrivial geometric phase and enhanced sensitivity to perturbations [37, 39, 40, 41, 42, 43, 44, 45].

The unique behavior of EPs in non-Hermitian systems can be exploited for various sensing applications, for example, in the detection of small changes in physical parameters, such as temperature, pressure, or electric fields, with increased precision compared to conventional sensing techniques. The measurement sensitivity gets enhanced near the EP, so that even tiny changes can cause significant variations in the system's response. Moreover, such systems can also be applied to quantum state estimation and metrology. By leveraging the intricate structure of non-Hermitian systems, it becomes possible to obtain precise information about the unknown quantum states or to estimate parameters that characterize quantum systems accurately.

Non-Hermitian quantum sensing is still a rapidly evolving field, with ongoing research focused on exploring the fundamental properties of non-Hermitian systems, developing new sensing protocols, and identifying practical applications. As scientists delve deeper into the realm of non-Hermitian quantum mechanics, they continue to unveil the potential of these systems for pushing the boundaries of quantum sensing and measurement technology.

In this chapter we explore the concept of non-Hermitian sensing. First, we present a two-level prototype of an EP sensor. In this system a non-Hermitian system at EP degeneracy is perturbed and the strength of the splitting is used for sensing purpose. Next, we discuss in detail the metrics that are used to assess the sensor performance, with a brief introduction to the concerns raised about the EP sensing in recent literature. Later, we will explain how Quantum Fisher Information (QFI) and Quantum Cramer Rao Bound (QCRB) become relevant in defining the limits achievable in sensing protocols. Finally, we study the perturbation theory at EPs and derive the QFI at EPs and study its implications on QCRB.

QCRB is a fundamental principle in quantum estimation theory that places a limit on the precision with which certain physical quantities can be estimated in quantum systems. It is an extension of the classical Cramér-Rao bound to the quantum realm. According to this bound, the uncertainty in estimating a parameter in a quantum system is inversely proportional to QFI. The QCRB bound plays a crucial role in understanding the fundamental limits of precision in quantum measurements and has implications in various fields, including quantum metrology, quantum information theory, and quantum sensing.

3.1 Exceptional point sensing

Several modern sensor devices are based on the detection of frequency (energy-level) splittings, e.g., magnetic field sensors, nanomechanical mass sensors etc. The system, say, a two level system (TLS) is a degenerate system at equilibrium. Detection of the target creates a perturbation which lifts this degeneracy. The amount of splitting or lifting enables to determine the strength of the target, Figure 3.1. Below, we explain this in mathematical terms.

Consider a two-level Hermitian degenerate sensor which is subjected to a perturbation of strength ϵ :

$$H_{DP} = \begin{pmatrix} E_0 & 0 \\ 0 & E_0 \end{pmatrix} + \epsilon \begin{pmatrix} E_1 & A_1 \\ B_1 & E_1 + \Delta E_1 \end{pmatrix}. \quad (3.1)$$

The eigenvalues for such a system are

$$\Lambda_- = \frac{1}{2}(-\epsilon\sqrt{4A_1B_1 + \Delta E_1^2} + \epsilon\Delta E_1 + 2E_0 + 2\epsilon E_1), \quad (3.2)$$

$$\Lambda_+ = \frac{1}{2}(\epsilon\sqrt{4A_1B_1 + \Delta E_1^2} + \epsilon\Delta E_1 + 2E_0 + 2\epsilon E_1). \quad (3.3)$$

Now consider a two-level defective sensor subjected to the same perturbation. The corresponding Hamiltonian is therefore as follows:

$$H_{EP} = \begin{pmatrix} E_0 & A_0 \\ 0 & E_0 \end{pmatrix} + \epsilon \begin{pmatrix} E_1 & A_1 \\ B_1 & E_1 + \Delta E_1 \end{pmatrix}, \quad (3.4)$$

the eigenvalues of which are given by

$$\Lambda_{-,EP} = \frac{1}{2}(-\sqrt{\epsilon}\sqrt{4A_0B_1 + 4\epsilon A_1B_1 + \epsilon\Delta E_1^2} + \epsilon\Delta E_1 + 2E_0 + 2\epsilon E_1), \quad (3.5)$$

$$\Lambda_{+,EP} = \frac{1}{2}(\sqrt{\epsilon}\sqrt{4A_0B_1 + 4\epsilon A_1B_1 + \epsilon\Delta E_1^2} + \epsilon\Delta E_1 + 2E_0 + 2\epsilon E_1). \quad (3.6)$$

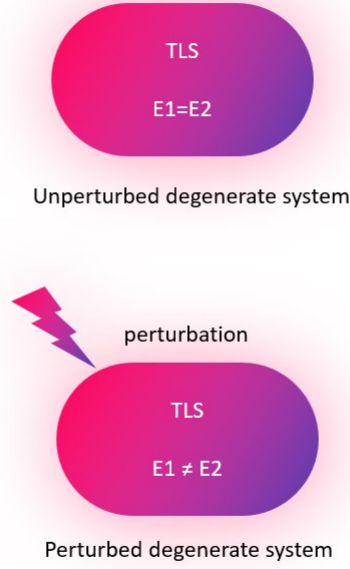


Figure 3.1: A schematic diagram of a two level system exhibiting energy degeneracy. When an external perturbation is applied, the degeneracy is generally broken.

The splitting in these two cases can be found as

- Hermitian case:

$$\Delta E_{DP} = \Lambda_+ - \Lambda_- = \epsilon \sqrt{4A_1B_1 + \Delta E_1^2}, \quad (3.7)$$

- Defective Case:

$$\Delta E_{EP} = \Lambda_+ - \Lambda_- = \sqrt{\epsilon} \sqrt{4A_0B_1 + 4\epsilon A_1B_1 + \epsilon \Delta E_1^2}. \quad (3.8)$$

To compare their sensitivities, we can set $\Delta E_1 = 0$, leading to

$$\Delta E_{DP} = 2\epsilon \sqrt{A_1B_1}, \quad \Delta E_{EP} = 2\sqrt{\epsilon} \sqrt{A_0B_1 + \epsilon A_1B_1}. \quad (3.9)$$

Choosing $A_0 = A_1$, their ratio can be obtained as

$$\frac{\Delta E_{EP}}{\Delta E_{DP}} = \sqrt{1 + \frac{1}{\epsilon}}. \quad (3.10)$$

Therefore, for $0 < \epsilon < 1$, the above ratio is always greater than 1, referring to more sensitivity Figure 3.2. It can be observed that the ratio never reaches 1, i.e. the splitting at exceptional point due to perturbation is always higher than that for Hermitian system for the same perturbation strength.

We find that there exist some experimental demonstrations of EP sensors in literature [42, 43, 46, 47, 48, 49, 50, 51, 52, 53] as well.

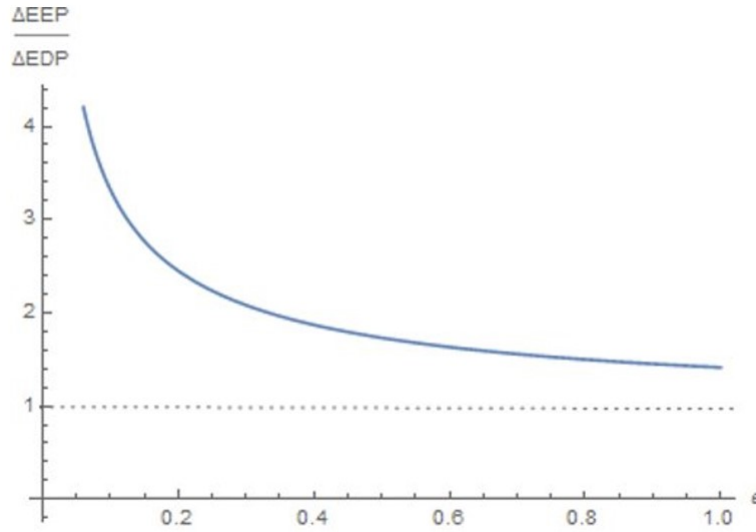


Figure 3.2: Plot of the ratio between the splitting for a perturbed exceptional point system and that for a perturbed Hermitian system, with respect to the perturbation strength ϵ .

3.2 Metrics for measuring sensor performance

Let us discuss about various metrics for performance of a standard sensor.

3.2.1 Sensitivity

The sensitivity S of a measurement device is typically defined as the ratio of the change in the output signal amplitude to the corresponding change in the input signal amplitude.

$$S = \frac{(\text{Change in output})}{(\text{Change in input})}. \quad (3.11)$$

It quantifies the instrument's ability to distinguish and measure small differences or increments in the measured parameter.

High sensitivity is desirable in many metrological applications because it allows for the detection of subtle changes and improves the precision and accuracy of measurements. A sensitive instrument can provide more detailed and precise information about the quantity being measured, enabling better control, analysis, and decision-making. It is important to note that sensitivity alone does not guarantee the accuracy or reliability of measurements. Other factors such as calibration, resolution, linearity, repeatability, and environmental conditions also play significant roles in the overall performance of a measuring instrument.

In the EP sensor setup we discussed earlier, it is easy to see that the frequency splitting due to perturbation is directly proportional to the sensitivity of the system.

However, it has been pointed out that merely having larger sensitivity is not a good measure of a better sensor [54, 55, 56]. This is because a more sensitive sensor may not distinguish between noise and signal and will amplify both simultaneously.

3.2.2 Signal-to-noise ratio

The signal-to-noise ratio (SNR) measures the ratio of the desired signal strength to the level of background noise or unwanted interference in the measurement. It indicates the quality of the measured signal relative to the noise present in the system. A higher SNR indicates a stronger, more reliable signal compared to the noise level. The SNR is usually expressed in decibels (dB) and can be calculated in terms of the ratio of signal power to noise power.

$$SNR(dB) = 10 \log_{10} \frac{\text{Signal Power}}{\text{Noise Power}} . \quad (3.12)$$

While the sensitivity focuses on the ability to detect small changes in the input signal, SNR assesses the quality and reliability of the measured signal in the presence of noise. A high sensitivity sensor can respond to small changes, but if the noise level is also high, it may lead to a low SNR and reduced accuracy of the measurement. Conversely, a sensor with a low sensitivity might not be able to detect small changes, regardless of the noise level. Hence, sensitivity reflects the responsiveness of a sensor to changes in the input quantity, while the SNR evaluates the quality of the measured signal relative to the background noise.

In [54, 56], the SNR has been used as a performance metric to study the effect of noise on EP sensors, while criticizing the use of sensitivity as a parameter in [38] and other earlier related articles.

3.2.3 Quantum Fisher Information

The concept of QFI is related to the precision of measurements through the (Quantum) Cramer-Rao bound.

The precision of a measurement refers to the degree of consistency, repeatability, or reproducibility of the measured results when multiple measurements are taken under similar conditions. It provides information about the scatter or spread of the data points around the average or expected value, Figure 3.3. Precision is distinct from accuracy. While precision refers to the consistency of measurements, accuracy refers to the proximity of the measured values to the true or accepted value. A measurement can be precise but not accurate if it consistently deviates from the true value, or it can be accurate but not precise if it shows a large spread of measurements around the true value.

The goal of quantum parameter estimation is to determine the value of a continuous parameter γ that is encoded within the state of a quantum system ρ_γ . This can be achieved by interacting the quantum system with an external signal that we aim to characterize. The process of parameter estimation involves two steps. First, the state ρ_γ is measured, and then, in the second step, the estimate of γ is obtained by processing the measurement outcomes using data-processing techniques.

In fact, we aim to determine a reliable approximation for a specific parameter of interest, such as the population mean (μ), by utilizing a sample. This approximation, referred to as a

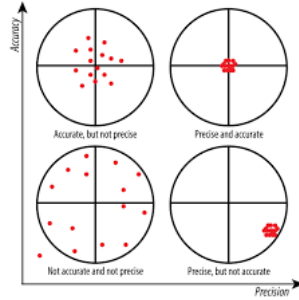


Figure 3.3: Difference between precision and accuracy.

point estimate or estimation, is computed by calculating a statistic, such as the sample mean (\bar{X}) or sample standard deviation (σ). The objective is to derive a numerical value that can be considered a plausible estimate for the true value of the parameter.

When discussing general concepts and inference methods, it is useful to have a generic symbol that represents the parameter of interest. In this case, we will use the letter γ for that purpose. The goal of estimation is to choose a single number, based on sample data, that serves as a reasonable value for γ . To obtain an estimate for the parameter γ , we select an appropriate statistics and calculate its value using the provided sample data. The chosen statistic is referred to as the estimator of γ which is denoted by $\hat{\gamma}$.

Ideally, we would like to have an estimator $\hat{\gamma}$ that always equals the true value γ . However, since $\hat{\gamma}$ is based on the sample X_i 's, it is actually a random variable. Consequently, there will be instances where $\hat{\gamma}$ produces a value larger than γ for a particular sample, while in other samples, $\hat{\gamma}$ will underestimate γ . If we express this situation in mathematical terms, we can write:

$$\hat{\gamma} = \gamma + \text{error} . \quad (3.13)$$

Therefore an accurate estimator would be one resulting in small estimation errors, so that estimated values will be near the true value. Mathematically, if we denote the estimator as $\hat{\gamma}$ and consider it as a random variable, the variance of the estimator, denoted as $\text{Var}(\gamma)$, is calculated as the average of the squared differences between the estimated values and their mean. It represents the average squared deviation from the expected value of the estimator. A lower variance indicates that the estimator tends to produce estimates that are closer to the true parameter value on average, implying higher precision. Converse is true for a higher variance.

Let us now establish the relation of the variance with the QFI. To understand QFI, we first need to introduce fidelity. In quantum mechanics, fidelity is a measure of the similarity or closeness between two quantum states or quantum operations. It quantifies how well a quantum state or operation can be preserved or reproduced. Let us consider a state parametrized by the parameter to be estimated and denote it by $|\psi(\gamma)\rangle$. The overlap between the states at γ and $\gamma + \delta\gamma$ is then given by

$$f(\gamma, \gamma + \delta\gamma) = \langle \psi(\gamma) | \psi(\gamma + \delta\gamma) \rangle , \quad (3.14)$$

where the state $|\psi(\gamma + \delta\gamma)\rangle$ can be expanded in Taylor series as

$$|\psi(\gamma + \delta\gamma)\rangle = |\psi\rangle + \delta\gamma |\partial_\gamma \psi\rangle + |\partial_\gamma^2 \psi\rangle \frac{\delta\gamma^2}{2!} + \dots \quad (3.15)$$

This leads to an explicit form of the overlap as

$$f(\gamma, \gamma + \delta\gamma) = 1 + \delta\gamma \langle \psi(\gamma) | \partial_\gamma \psi(\gamma) \rangle + \frac{\delta\gamma^2}{2!} \langle \psi(\gamma) | \partial_\gamma^2 \psi \rangle + \dots \quad (3.16)$$

The fidelity is therefore given by

$$|f|^2 = 1 + \delta\gamma (\langle \psi | \partial_\gamma \psi \rangle + \langle \partial_\gamma \psi | \psi \rangle) + \delta\gamma^2 (\langle \partial_\gamma \psi | \psi \rangle + \frac{1}{2} \langle \psi | \partial_\gamma^2 \psi \rangle + \frac{1}{2} \langle \partial_\gamma^2 \psi | \psi \rangle) + \dots \quad (3.17)$$

Using the following identities

$$\begin{aligned} \langle \psi | \partial_\gamma \psi \rangle + \langle \partial_\gamma \psi | \psi \rangle &= \frac{\partial \langle \psi | \psi \rangle}{\partial \gamma} = 0 \\ \langle \partial_\gamma^2 \psi | \psi \rangle + \langle \psi | \partial_\gamma^2 \psi \rangle &= -2(\langle \partial_\gamma \psi | \partial_\gamma \psi \rangle), \end{aligned} \quad (3.18)$$

we finally get

$$|f|^2 = 1 + \frac{\delta\gamma^2}{2} (\langle \psi | \partial_\gamma \psi \rangle \langle \psi | \partial_\gamma \psi \rangle - \langle \partial_\gamma \psi | \partial_\gamma \psi \rangle) = 1 - \frac{\delta\gamma^2}{2} (\chi_\gamma) \quad (3.19)$$

Here χ_γ is known as the fidelity susceptibility, and can be expressed as

$$\chi_\gamma = \frac{2 - 2|f|^2}{\delta\gamma^2}. \quad (3.20)$$

where the numerator $2 - 2|f|^2$ is also known as Bures distance [57, 58]. The QFI is defined as

$$QFI = \frac{1}{4} \chi_\gamma = \lim_{\delta\gamma \rightarrow 0} \frac{1}{4} \left(\frac{\langle \partial_\gamma \psi | \partial_\gamma \psi \rangle - |\langle \psi | \partial_\gamma \psi \rangle|^2}{\delta\gamma^2} \right). \quad (3.21)$$

It is to be noted that in [59, 60], the QFI is defined as just the numerator of the above relation. We choose to use Equation 3.21 in our work, as this suits numerical studies.

The Quantum Cramer Rao Bound (QCRB) as discussed in [57, 61] is given by

$$\text{Var}(\gamma) = \frac{1}{nQFI(\gamma)}, \quad (3.22)$$

where n is the number of measurements performed. This bound sets the minimum possible variance of γ in the estimation protocol concerned. We can see that higher the QFI , lesser the variance and better the estimation and sensing. In fact, in literature [54, 55, 56] QFI is often considered as a measure of performance.

3.3 Concerns with EP sensing

Two major concerns arise with EP sensors. One is the systems with non-Hermitian Hamiltonians have remained elusive and second the effect of noise. Effect of noise on EP sensors has recently been studied, though there has not been any consensus among researchers on whether the EP sensors can provide any sensing advantage in presence of noise.

As discussed in section 3.1, the sensitivity is increased when a sensor is kept at an exceptional point degeneracy rather than Hermitian degeneracy. However, using sensitivity as a performance metric for sensors is dubious as a more sensitive sensor not only amplifies required signal but also amplifies noise.

In [37] the author discusses the effect of classical noise on EP sensors. Some work has been done where the effect of classical noise on such sensors is shown to be ameliorated. For example, in a class of electronic circuits, it has been shown theoretically [62] that the additional noise caused by the gain in PT-symmetric arrangements can be made very small.

On the other hand, the effect of quantum noise has been studied theoretically in [63, 54, 55, 56]. Some of the claims in these articles have been contradictory. The authors of [63] showed that the field changes at both DPs (i.e. Hermitian degeneracy) and EPs are proportional to the perturbation parameter ϵ . This means that the response at an EP is not parametrically larger than at a DP. In fact, the response at an EP can be even larger in absolute value. However, this does not mean that EP-based sensors have a superior scaling behavior in terms of the quantum-limited signal-to-noise ratio. This is because this ratio is not only determined by the response of the sensor, but also by the noise that is present in the system. It is argued that the noise that is present in real systems will likely mask any advantage that EP-based sensors may have in terms of response.

In [54], the authors focus on analyzing the parametric-sensing properties of linear coupled-mode systems that are described by effective non-Hermitian Hamiltonians. It explores the potential of non-Hermitian systems, specifically the existence of exceptional points, as a resource for sensing applications. The impact of noise and utility in both classical and quantum regimes is investigated to gain a comprehensive understanding of the system's behavior. The analysis takes into account noise effects in both these regimes and considers a realistic and optimal measurement protocol based on coherent driving and homodyne detection. By studying two-mode devices, they derive fundamental bounds on the signal power and signal-to-noise ratio for any sensor based on non-Hermitian systems. These bounds provide insights into the fundamental limits of such sensors. These results demonstrate that enhanced signal power can be achieved by incorporating gain in the system, without necessarily requiring proximity to an EP. This finding indicates that EP physics is not the sole factor determining the signal power enhancement in these sensors.

Moreover, when considering the effects of noise, the researchers show that non-reciprocity plays a crucial role in sensing. Non-reciprocity allows the sensor to surpass the fundamental bounds that constrain conventional reciprocal sensors. In other words, non-reciprocity becomes a valuable resource for achieving parametrically-enhanced sensing capabilities. The analysis also explores simple two-mode non-reciprocal sensors that enable this parametrically-enhanced sensing without relying on EP physics. These sensors offer a promising approach to surpass the limits of conventional reciprocal sensing systems, highlighting the potential of non-Hermitian systems in sensing applications.

The sensitivity of parameter estimation near exceptional points has been further explored using the precise framework of quantum Fisher information [55]. By utilizing the exact formalism of quantum Fisher information, one can determine the maximum sensitivity attainable without specifying a particular measurement approach. However, contrary to expectations, the study finds that exceptional points do not exhibit a significant enhancement of sensitivity. Instead, the merging of eigenstates precisely counteracts the divergence

of eigenvalue susceptibility at the exceptional point. This counteraction results in a smooth relationship between sensitivity and the perturbative parameter. In other words, the sensitivity does not show any dramatic changes or enhancements at the exceptional point; rather, it behaves as a continuous function of the perturbative parameter.

A quantum noise theory has also been developed that allows one to calculate the signal-to-noise performance of an EP sensor [56]. The concept of quantum Fisher information (QFI) is employed to establish a lower bound for the signal-to-noise ratio (SNR). By utilizing this framework, it is demonstrated that parametrically enhanced SNR is indeed possible in EP sensors, which is in contradiction to [63, 54, 55].

Furthermore, the researchers devise a specific experimental protocol for sensing using an EP amplifier operating close to its lasing threshold, coupled with heterodyne signal detection. This protocol is designed to achieve the optimal scaling predicted by the Fisher bound. The results obtained from this experimental setup can be generalized to higher order EPs in any bosonic non-Hermitian system with linear interactions.

In comparison of recent articles exploring the performance of EP sensors, we see that the results in [63, 54, 55] are contradictory to the findings of [56]. In chapter 5 we explore the argument by simulating the system on an actual quantum computer and measure the QFI at EPs.

3.4 QFI for non-Hermitian Hamiltonians

3.4.1 Calculating QFI for non-Hermitian Hamiltonians

As the Hermitian systems follow orthogonality rules, the systems with complex Hamiltonians do not follow the same criteria. We had discussed this in chapter 1, that the eigenstates of non-Hermitian Hamiltonians follow "bi-orthogonality" and "self-orthogonality" rules. This leads to change in expression of the QFI and other quantities. Moreover around EP we will assume that eigenvalues and eigenvectors of perturbed Hamiltonians expand with fractional order powers of the perturbation parameter γ rather than integer, as in case of Taylor and Laurent series. This expansion is known as "Puiseux series" expansion, which is an artifact of expansion at algebraic singularities. We will give explanation for this expansion in next section. As we consider a two-level system, only the first order EP can be obtained in such a system. Hence, the perturbed eigenvalues and eigenvectors expand in the fractional powers of $\gamma^{1/2}$. Let us understand it further in this section.

The QFI in non-Hermitian case is given as

$$QFI = \lim_{\delta\gamma \rightarrow 0} \frac{1}{4} \left(\frac{\langle \partial_\gamma \chi | \partial_\gamma \phi \rangle - |\langle \phi | \partial_\gamma \chi \rangle|^2}{\delta\gamma^2} \right). \quad (3.23)$$

Note here $|\phi\rangle$ is the eigenstate of H and $|\chi\rangle$ is the eigenstate of H^\dagger . Note that the above definition is different from the Equation 3.21.

3.4.2 Quantum Fisher Information around EP

We will consider a two-level system parameterized by γ ($H_p(\gamma)$) with EP at $\gamma = 0$. Let us consider a small perturbation around exceptional point. This gives us the eigenvalue equation

$H_p |\phi_p\rangle = \lambda_p |\phi_p\rangle$ for non-Hermitian Hamiltonian around EP.

$$(H + \gamma H' + \dots)(|\phi\rangle + \gamma^{1/2} |\phi'\rangle + \dots) = (\lambda + \gamma^{1/2} \lambda' + \dots)(|\phi\rangle + \gamma^{1/2} |\phi'\rangle + \dots) . \quad (3.24)$$

Here we have used the concept of Puiseux series expansion as EP are square root singularities in parameter space [64, 65]. Expanding the brackets and comparing the powers of γ , we get

$$H |\phi\rangle = \lambda |\phi\rangle , \quad (3.25)$$

$$H |\phi'\rangle = \lambda |\phi'\rangle + \lambda' |\phi\rangle , \quad (3.26)$$

$$H |\phi''\rangle + H' |\phi\rangle = \lambda |\phi''\rangle + \lambda' |\phi'\rangle + \lambda'' |\phi\rangle . \dots \quad (3.27)$$

Now consider the inner product $\langle \chi^J | (|\phi\rangle + \gamma^{1/2} |\phi'\rangle + \dots) \rangle$ where $|\chi^J\rangle$ is the Jordan normal vector for H^\dagger . As $\langle \chi^J | \phi \rangle = 1$ according to self-orthogonality rule defined in chapter 1, we have

$$\langle \chi^J | \phi^i \rangle = 0 , \quad (3.28)$$

where $i = 1, 2, \dots$ (i.e. higher order perturbations). Multiplying the second equation in Equation 1.33 with λ' and comparing it with Equation 3.26, we have

$$|\phi'\rangle = \lambda' |\phi^J\rangle . \quad (3.29)$$

Let us now substitute this in Equation 3.27, to obtain

$$H |\phi''\rangle + H' |\phi\rangle = \lambda |\phi''\rangle + \lambda'^2 |\phi^J\rangle + \lambda'' |\phi\rangle . \quad (3.30)$$

Multiplying by $\langle \chi |$ (i.e., the eigenvector of H^\dagger) from left, we get

$$\langle \chi | (H - \lambda) | \phi \rangle = \lambda'^2 \langle \chi | \phi^J \rangle + \lambda'' \langle \chi | \phi \rangle - \langle \chi | H | \phi \rangle . \quad (3.31)$$

As $\langle \chi | H = \lambda \langle \chi |$, the left hand side of the above equation identically vanishes, and therefore, the from the right hand side, we get

$$\lambda'^2 \langle \chi | \phi^J \rangle + \lambda'' \langle \chi | \phi \rangle - \langle \chi | H | \phi \rangle = 0 . \quad (3.32)$$

Finally, using the self-orthogonality rules $\langle \chi | \phi^J \rangle = 1$ and $\langle \chi | \phi \rangle = 0$, we get the following expressions of the eigenvalues:

$$\lambda'_\pm = \pm \sqrt{\langle \chi | H | \phi \rangle} . \quad (3.33)$$

Hence the perturbed eigenvector can be written as

$$|\phi_{p\pm}\rangle = |\phi_\pm\rangle + \gamma^{1/2} \lambda'_\pm |\phi_\pm^J\rangle + \dots \quad (3.34)$$

Now let us find the normalization constant N for $|\phi_p\rangle$. To calculate this, we note that $N^2 = (\langle \chi | + \gamma^{1/2} \lambda'_\pm \langle \chi^J |) (|\phi\rangle + \gamma^{1/2} \lambda'_\pm |\phi^J\rangle)$. Using the bi-orthogonality and self-orthogonality rules, we have

$$N^2 = 2\gamma^{1/2} \lambda'_\pm , \quad (3.35)$$

leading to the following form of the normalization constant:

$$N = \frac{1}{\sqrt{2\gamma^{1/2}\lambda'_\pm}} . \quad (3.36)$$

This gives us

$$|\phi_{p\pm}\rangle = \frac{1}{\sqrt{2\lambda'_\pm}} \left[\gamma^{-1/4} |\phi_\pm\rangle + \gamma^{1/4} \lambda'_\pm |\phi_\pm^J\rangle \right] , \quad (3.37)$$

$$|\chi_{p\pm}\rangle = \frac{1}{\sqrt{2\lambda'_\pm}} \left[\gamma^{-1/4} |\chi_\pm\rangle + \gamma^{1/4} \lambda'_\pm |\chi_\pm^J\rangle \right] , \quad (3.38)$$

where $|\chi_p\rangle$ is the perturbed eigenvector from an EP for H^\dagger . Let us differentiate Equation 3.37 with respect to γ . This leads to

$$|\partial_\gamma \phi_{p+}\rangle = \frac{1}{\sqrt{2\lambda'_+}} \left[\frac{-1}{4} \gamma^{-5/4} |\phi_+\rangle + \frac{1}{4} \gamma^{-3/4} \lambda'_+ |\phi_+^J\rangle \right] . \quad (3.39)$$

Note we have taken only one of the eigenstates (i.e. $+$) to study further. We multiply and divide the right hand side by γ and using the fact that $\lambda'_+ = -\lambda'_-$, we get

$$|\partial_\gamma \phi_{p+}\rangle = \frac{i}{4\gamma} \left[\frac{1}{\sqrt{2\lambda'_-}} \left(\gamma^{-1/4} |\phi_+\rangle + \gamma^{1/2} \lambda'_- |\phi_+^J\rangle \right) \right] = \frac{i}{4\gamma} |\phi_{p-}\rangle . \quad (3.40)$$

and similarly $(|\partial_\gamma \phi_{p+}\rangle)^\dagger = \frac{-i}{4\gamma} \langle \chi_{p-}|$. We used the fact that $(|\phi_{p-}\rangle)^\dagger = \langle \chi_{p-}|$ from the bi-orthogonality rules.

Now if we calculate the QFI for complex Hamiltonians Equation 3.23, we get,

$$QFI \propto \left[\frac{1}{16\gamma^2} \langle \chi_{p-} | \phi_{p-} \rangle + \frac{i}{4\gamma} \langle \chi_{p-} | \phi_{p+} \rangle \right] \propto \frac{1}{\gamma^2} . \quad (3.41)$$

We have used the bi-orthogonality rules $\langle \chi_{p-} | \phi_{p-} \rangle = 1$ and $\langle \chi_{p-} | \phi_{p+} \rangle = 0$. This shows us that the QFI diverges at EP which is at $\gamma = 0$.

3.4.3 Why Puiseux series expansion ?

Let us understand why we need Puiseux series expansion for a two-level system around EP in fractional power of perturbation parameter, $\gamma^{1/2}$.

Consider the equation

$$(H + \gamma H')(|\phi\rangle + |\bar{\phi}'\rangle + |\bar{\phi}''\rangle + \dots) = (\lambda + \bar{\lambda}' + \bar{\lambda}'')(|\phi\rangle + |\bar{\phi}'\rangle + |\bar{\phi}''\rangle + \dots) . \quad (3.42)$$

Note that unlike in Equation 3.24, we have not written the powers of γ here and assumed that it is absorbed in the eigenvector and eigenvalue terms. Taking inner product of Equation 3.42 with $\langle \chi|$ and using the self-orthogonality rules, we get

$$\gamma \langle \chi | H' | \phi \rangle = \bar{\lambda}' \langle \chi | \bar{\phi}' \rangle , \quad (3.43)$$

Assuming that the left hand side does not vanish, the above equation implies that $\bar{\lambda}' |\bar{\phi}'\rangle$ is proportional to γ as $|\phi\rangle$, $|\chi\rangle$, and H' are independent of it at EP. This means each $\bar{\lambda}'$ and $|\bar{\phi}'\rangle$ is proportional to fractional power of γ . Now it remains to find the power. Combining the first order equations in Equation 3.42 we have

$$(H - \lambda) |\bar{\phi}'\rangle = \bar{\lambda}' |\phi\rangle . \quad (3.44)$$

This shows that using the arguments earlier, we have $|\bar{\phi}'\rangle$ and $\bar{\lambda}'$ to have the same powers. Therefore, combining the results of Equation 3.43 and Equation 3.44, we conclude that the both $|\bar{\phi}'\rangle$ and $\bar{\lambda}'$ are both proportional to $\gamma^{1/2}$. Similarly, we can find the proportionality for higher orders.

Hence, we have for the perturbed eigenvalues and eigenvectors

$$\lambda_{p\pm} = \lambda \pm \gamma^{1/2} \lambda' \pm \gamma \lambda'' + \dots \quad (3.45)$$

$$|\phi_{p\pm}\rangle = |\phi\rangle \pm \gamma^{1/2} |\phi'\rangle \pm \gamma |\phi''\rangle + \dots \quad (3.46)$$

For comparison let us consider degenerate eigenvalue away from EP. In this case, the self-orthogonality does not apply and we have

$$\gamma \langle \chi | H' | \phi \rangle = \bar{\lambda}' \langle \chi | \phi \rangle , \quad (3.47)$$

$$(H - \lambda) |\bar{\phi}'\rangle = -\gamma H' |\phi\rangle , \quad (3.48)$$

instead of Equation 3.43 and Equation 3.44. Using above expressions we see that $\bar{\lambda}'$ and $|\bar{\phi}'\rangle$ in this case are proportional to γ and hence we have integer power expansions in this case with respect to γ .

A more rigorous and concise proof is found in [64].

3.5 Experimental demonstrations

There are several experimental demonstrations of EP sensors. Most of the demonstrations are in optics domain and a very few are in quantum domain or do explore quantum sensing. We would like to enumerate a few with a short description:

article	description
[46]	The experimental verification of [38] prediction regarding the increased splitting was successfully achieved within an optical micro-cavity.
[66]	A particle sensor based on an integrated exceptional surface system has been successfully implemented. The results showcased an observable improvement in the frequency splitting due to minor perturbations.
[42]	A higher order EP had been successfully demonstrated believed to achieve higher sensitivity.
[47]	The concept of EP-based sensing has been applied in a modified fashion to thermal mapping
[48, 49, 50, 51]	Classical wireless EP sensor demonstrations. The inductive coupling between the sensor and a reader is the basis for operation. The quantity being measured detunes the capacitive or inductive components of the sensor, causing frequency shifts that the reader may detect externally.
[52, 53]	These articles consider demonstration of ring laser gyroscopes with EP enhancement
[67]	This article demonstrates EP based sensors in plasmonic domain.
[68]	This article exploits the phenomenon of stochastic resonance to overcome the sensitivity of EP to noise.

Some interesting proposals worth mentioning are [69] where the authors suggested a concept that involved leveraging exceptional surfaces to amplify the sensitivity of a particle sensor while minimizing the impact of unwanted disturbances. In [70] an anti-PT-symmetric device was proposed for particle sensing. In [71] a novel concept of utilizing a spinning resonator, rotating at its center, was put forward to attain exceptional points for nanoparticle detection and sensing capabilities. In [72] it was proposed that EP present in an optomechanical cavity can be utilized to enhance the sensitivity of a mass sensor. This can be achieved by manipulating the cavity's operation through the use of a blue-detuned laser to induce gain or a red-detuned laser to induce loss. There is rapid progress in realizing the sensors, however there are still many conceptual and theoretical difficulties in understanding them.

3.6 Conclusion

In our exploration, we began by providing a general overview of the initial proposals for EP (Exceptional Point) sensors. These sensors utilize the unique properties of EPs, which are points of non-Hermitian degeneracy in physical systems. Moving forward, we delved into various metrics used to assess the performance of any sensor. Specifically, we discussed sensitivity, signal-to-noise ratio (SNR), and quantum Fisher information (QFI) as key evaluation criteria.

Continuing our discussion, we addressed concerns related to EP sensors, considering potential challenges and limitations associated with their implementation. Moreover, we ex-

plored the QFI for non-Hermitian Hamiltonians, broadening our understanding of the fundamental principles involved in EP sensing.

In a significant development, we derived a form of QFI specifically around the vicinity of EPs and demonstrated that, in general, it diverges around these points of non-Hermitian degeneracy. This finding highlighted the intricate nature of EPs and their impact on the sensitivity and precision of EP sensors.

Finally, we provided an overview of several experimental realizations of EP sensors, showcasing their practical applications. Additionally, we discussed intriguing proposals that have emerged in the field, further expanding the potential of EP sensing in various domains. By exploring the theoretical foundations, concerns, and practical implementations of EP sensors, we gained valuable insights into the advancements and challenges within this exciting field.

Chapter 4

Isolation Frequency Tunable Optomechanical Isolator

An optical isolator can be treated as an optical analog of an electronic diode. As the diodes allow the electrons to move predominantly along one direction and not in the opposite direction, an optical isolator lets the photons transmit in only one direction. The system becomes transparent for only one direction of the field, and opaque in another direction. Quantitatively, the input and output mode of an ideal two-port optical isolator can be related via a scattering matrix S , as

$$\bar{A}_{out} = S\bar{A}_{in} \text{ where } S = \begin{pmatrix} 0 & 1 \\ 0 & 0 \end{pmatrix} \text{ or } \begin{pmatrix} 0 & 0 \\ 1 & 0 \end{pmatrix}, \quad (4.1)$$

and \bar{A}_{in} and \bar{A}_{out} are the column vectors representing the input and output modes of the device. In such scenarios the scattering matrix of the isolator is not unitary as discussed in [73, 74].

However, it is challenging to construct an isolator for light (or photons) due to the Lorentz reciprocity theorem. According to this theorem, a device with linear, isotropic, and time-independent dielectric constant [74, 73] cannot be non-reciprocal and hence cannot be used for isolation. In addition, an ideal optical diode (a) should function for any arbitrary frequency of light, i.e., the matrix S should be frequency-independent, (b) should not require an external control field or a bias (note that the Faraday isolators, on the other hand, require an external magnetic field to operate [75]), (c) should not modify the transmitted light in the direction in which the device is transparent. An OM (optomechanical) isolator exploits the OM coupling between light and a mechanical resonator to generate the non-reciprocity and isolation.

To understand the functioning of OM isolators let us look at the following discussion. An atomic system which behaves like an opaque medium for an input probe light field with certain frequency, in the presence of a suitable control field will appear transparent for the same probe field. Such quantum optical phenomenon is often referred to as the electromagnetically induced transparency (EIT)[76]. The control field modifies the atomic system such that there is resonance in the transmission profile of the system at the input probe field frequency [77]. Alternatively, EIT can be mimicked in Optomechanical systems and is known

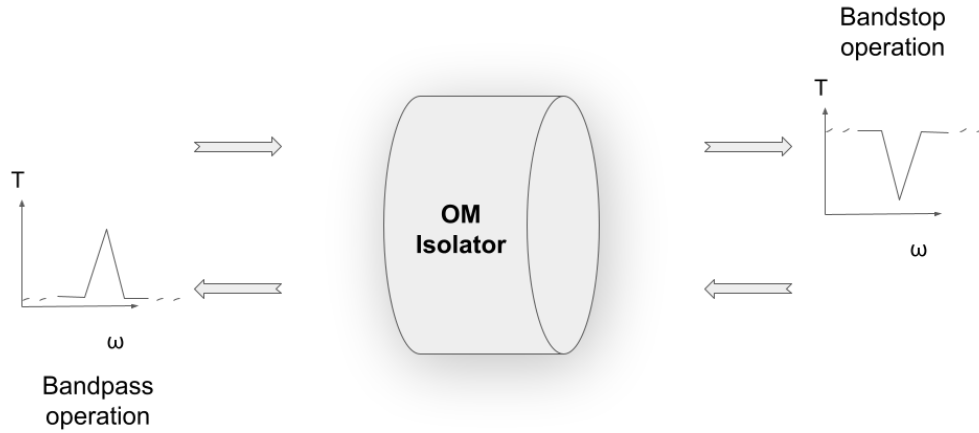


Figure 4.1: A schematic diagram of the OM isolator. This depicts that OM isolator acts as Bandpass filter for an input from right to left direction and Band stop in another. The arrows depict input and output on both sides. The plots represent transmission (T) v/s frequency of the input (ω). The center frequency of both processes should be same and we call it isolation frequency. It is to be noted that filters are resonant systems and hence OM isolator is also a resonant system.

as optomechanically induced transparency (OMIT) [78]. The obverse phenomenon of EIT is electromagnetically induced absorption (EIA) [79, 80, 81] where absorption can be induced by a control light field, thus making a medium which was transparent for an input light field at a certain frequency, to become opaque for it. Here, the control field modifies the atomic system such that there is anti-resonance (dip) in the transmission profile of the system at the input probe field frequency. Its optomechanical analogue is known as optomechanically induced absorption (OMIA) which has been experimentally verified by [82, 83, 84, 85, 86]. It should be noted that these phenomenon work only for certain input probe frequency because it is an interplay of resonance and anti-resonances. Usually, EIT/EIA is explained as the phenomena where a quantum destructive/constructive interference between the different excitation pathways to atomic levels enhances/reduces light transmission over a narrow spectral region in a coherently driven atomic system. Hence, EIT/EIA have been proposed for bandpass/band reject filtering as it works for narrow spectral region [87, 88, 89].

Anti-resonance occurs when at least one of the oscillator in coupled oscillators is driven. This system is not usually explored in standard textbooks. They are pronounced minimum in the amplitude of one of the coupled oscillator for a particular driving frequency (they are the exact opposite of what resonance is). Unlike resonance, coupling is essential for anti-resonance [90, 31]. In the quantum domain it has been discussed recently in [30]. Anti-resonance plays a major role in OM non-reciprocity and OM isolation, by creating a dip in the amplitude of one of the outputs at a particular frequency.

In recent years, OM isolators have emerged as possible candidates for achieving isolation [1, 91, 32, 92, 93]. It was seen that in these systems for particular input signal frequency,

and phase difference between the control fields, the scattering matrix of the isolator is as given by Eq. (4.1). It is to be noted that OM isolators work only for particular input signal frequency like all resonant systems (i.e. there is resonance or antiresonance only for certain driving frequency) [91]. Hence, they are proposed primarily for filtering purpose [91]. In brief, Bandpass filters are devices which encounter resonance at a particular frequency of the signal, on the other hand Bandstop or Notch filters encounter anti-resonance for a particular frequency of the signal [94]. Hence, an OM isolator is a Bandpass filter in one direction and a Bandstop filter in another Fig. 4.1. The frequency at which the filter operates is known as center frequency. In an OM isolator, the center frequency of the Bandpass and Bandstop process, has to be the same and we would call it "isolation frequency". This is a limitation for any broadband application of OM isolator. We try to circumvent this issue by providing tunability to the isolation frequency of the OM isolator.

The structure of this chapter is as follows : In section 4.1, we explore the requirements of OM coupling term for the tunability of the OM isolation frequency. In Section 4.2, we discuss a tunable model of OM isolators with a mechanical drive attached to a quadratically OM coupled membrane. In Section 4.3, we discuss the non-reciprocal features of such a device. Finally, in Section 5, we discuss experimental proposals and conclude. In the section 4.4, we discuss the requirement of the phase difference of the cavity driving fields, for isolation. For the theory and preliminaries related to this chapter the reader can refer to chapter 2.

4.1 Requirements for Tunable OM isolator

It has been observed in previous works on OM isolators, that the center (or isolation) frequency depends on the natural frequency of the mechanical mode (ω_{b1}), i.e. isolation is observed only when the signal frequency is equal to the natural frequency of the mechanical mode. This has been discussed in the following commentary [91]. It is also mentioned that the Bandwidth limitation of these OM isolators make them suitable for filtering applications. Hence, we can achieve tunability of the center frequency by having control over ω_{b1} .

One possible way is by driving the mechanical mode. There are research articles discussing the addition of driving to mechanical mode, however its' application for tunability of OM isolators has not yet been explored. We discuss these articles in detail in Sec. 5. By driving the mechanical mode it can be observed that in the certain rotating frame $\omega_{b1} \rightarrow \Delta_{b1}$ where $\Delta_{b1} = \omega_{b1} - \omega_{db1}$, i.e. the difference between natural mechanical frequency and the driving frequency of the mechanical drive. This is similar to the case where the natural frequency of the cavities needs to be replaced by the optical detunings, inside the Hamiltonian. We can use this control over the frequency of the mechanical drive, to control the detuning and indirectly control the isolation frequency of the device.

Quantitatively, for an OM isolator with an Hamiltonian of an MIM setup, the Hamiltonian is

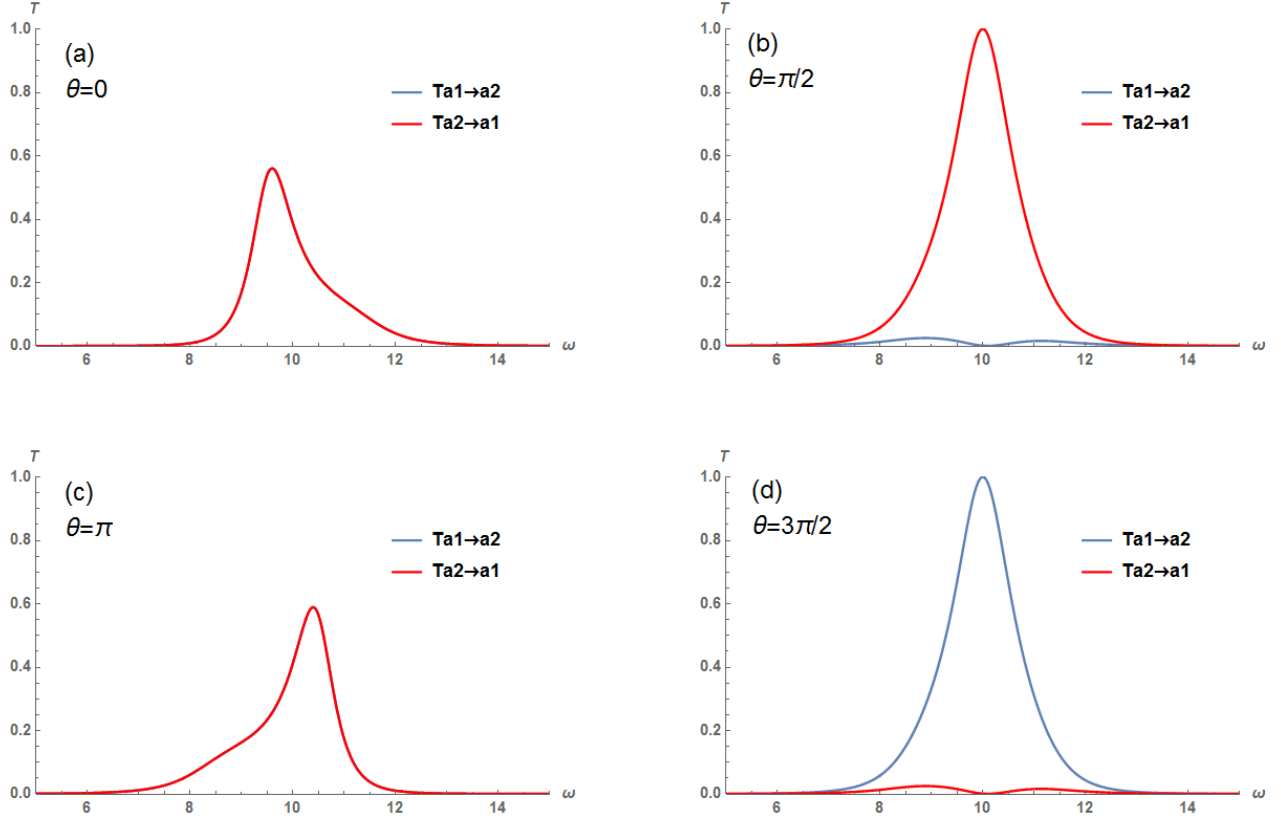


Figure 4.2: Variation of scattering probabilities T_{12} and T_{21} with the normalized input frequency ω/γ for (a) $\theta = 0$, (b) $\theta = \pi/2$, (c) $\theta = \pi$, and (d) $\theta = 3\pi/2$. The other parameters chosen are $J = |G_{11}| = |G_{21}| = \gamma_{a1}/2 = \gamma_{a2}/2 = \gamma_{b1}/8 = \gamma/2$ and $\Delta''_{b1} = \Delta''_{a1} = \Delta''_{a2} = \Delta = 10\gamma$. Clearly, with suitable choice of θ , one can achieve non-reciprocity of in either direction, i.e., either $T_{12} = 0$ or $T_{21} = 0$.

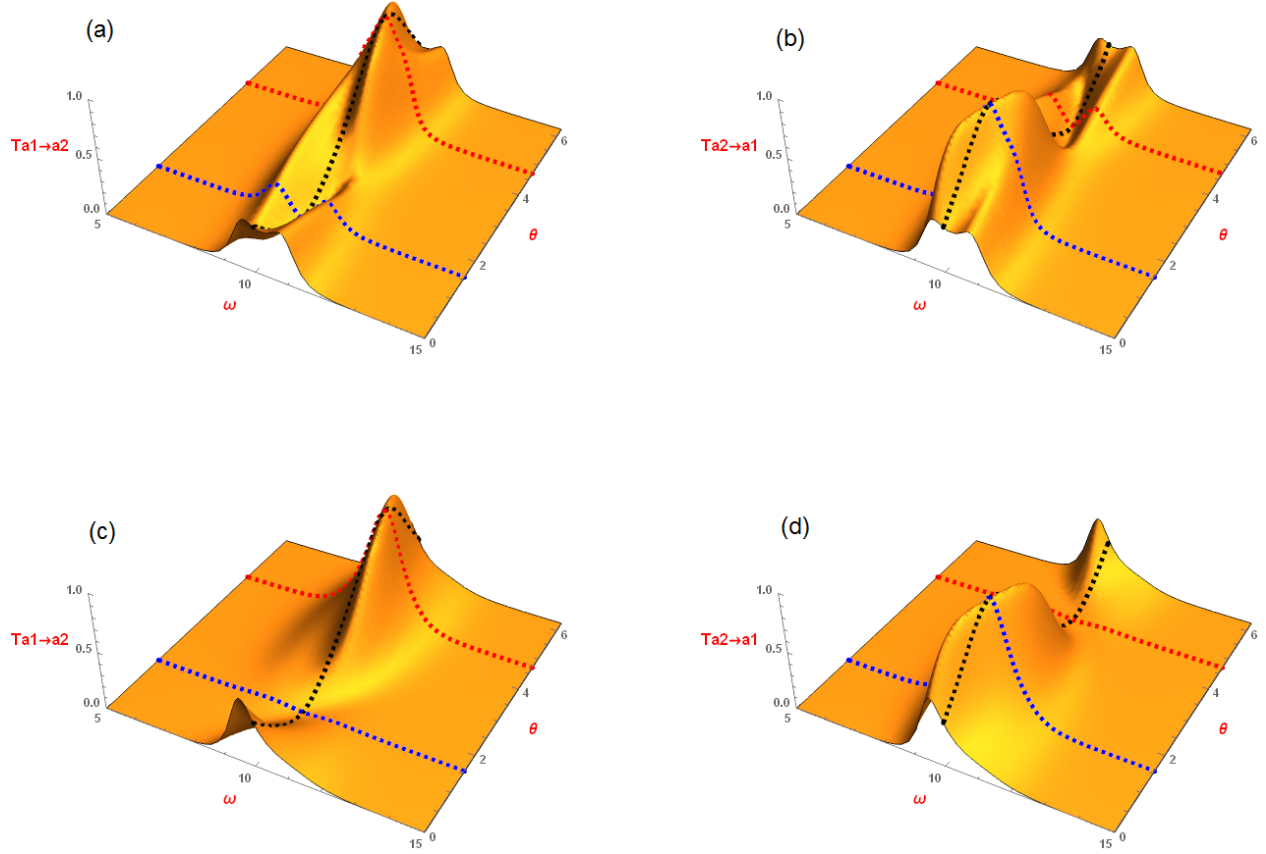


Figure 4.3: Complete profile of T v/s signal frequency ω and modified Optomechanical coupling phase θ . (a) $T_{a1 \rightarrow a2}$ for $|G_{11}| = |G_{21}| = \gamma_{a1}/4 = \gamma_{a2}/4 = \gamma_{b1}/4 = \gamma/4$. (b) $T_{a2 \rightarrow a1}$ for $|G_{11}| = |G_{21}| = \gamma_{a1}/4 = \gamma_{a2}/4 = \gamma_{b1}/4 = \gamma/4$. (c) $T_{a1 \rightarrow a2}$ for $|G_{11}| = |G_{21}| = \gamma_{a1}/2 = \gamma_{a2}/2 = \gamma_{b1}/8 = \gamma/2$. (d) $T_{a2 \rightarrow a1}$ for $|G_{11}| = |G_{21}| = \gamma_{a1}/2 = \gamma_{a2}/2 = \gamma_{b1}/8 = \gamma/2$. Black dotted line depicts $\omega = 10\gamma$. Red (Blue) line depicts $\theta = \pi/2$ ($3\pi/2$). Here, (a) and (b) profiles are as observed in [1], however it is to be noted that the parameters are different in this case.

$$\begin{aligned}
H = & \omega_{a1}a_1^\dagger a_1 + \omega_{a2}a_2^\dagger a_2 + \omega_{b1}b_1^\dagger b_1 + J(a_1^\dagger a_2 + a_2^\dagger a_1) \\
& + g_{11}a_1^\dagger a_1(b_1^\dagger + b_1) + g_{21}a_2^\dagger a_2(b_1^\dagger + b_1) \\
& + i \left[\epsilon_{a1}e^{-i(\omega_{da1}t - \phi_{a1})}a_1^\dagger + \epsilon_{a2}e^{-i(\omega_{da2}t - \phi_{a2})}a_2^\dagger \right. \\
& \left. + \epsilon_{b1}e^{-i(\omega_{db1}t - \phi_{b1})}b_1^\dagger - h.c. \right], \tag{4.2}
\end{aligned}$$

where a_i (for $i=1,2$) are the optical modes of the cavities, ω_{ai} and ω_{b1} are the optical and mechanical natural frequencies. J is the optical coupling constant. ' g_{ij} ' are the OM coupling constants, 'i' denoting the index for the optical mode and 'j' denoting the phonon mode. ω_{dai} and ω_{db1} are the driving frequencies. ϵ_{ai} and ϵ_{b1} are the amplitudes of the driving. ϕ_{ai} and ϕ_{b1} are the phases of the driving.

The first two terms describe the bare Hamiltonian of the cavities and the third term describes the membrane (neglecting the constant terms of $1/2$). The fourth term describes the optical coupling term between the two cavities. The fifth and sixth terms are known as the OM coupling terms, they denote the photon-phonon coupling for the cavities. The last term describes the driving part and includes the term for periodic driving of the mechanical membrane.

Upon rotating the frame using $U = \exp[i(\omega_{da1}ta_1^\dagger a_1 + \omega_{da2}ta_2^\dagger a_2 + \omega_{db1}tb_1^\dagger b_1)]$ i.e. upon the transformation $H' = UH U^\dagger - iU \frac{\partial U^\dagger}{\partial t}$. It can be observed that the transformed Hamiltonian is

$$\begin{aligned}
H' = & \Delta_{a1}a_1^\dagger a_1 + \Delta_{a2}a_2^\dagger a_2 + \Delta_{b1}b_1^\dagger b_1 + J(a_1^\dagger a_2 + a_2^\dagger a_1) \\
& + g_{11}a_1^\dagger a_1(b_1^\dagger e^{i\omega_{db1}t} + b_1 e^{-i\omega_{db1}t}) \\
& + g_{21}a_2^\dagger a_2(b_1^\dagger e^{i\omega_{db1}t} + b_1 e^{-i\omega_{db1}t}) \\
& + i \left[\epsilon_{a1}e^{i\phi_{a1}}a_1^\dagger + \epsilon_{a2}e^{i\phi_{a2}}a_2^\dagger + \epsilon_{b1}b_1^\dagger e^{i\phi_{b1}} - h.c. \right]. \tag{4.3}
\end{aligned}$$

We consider both cavities are driven by same frequency, $\omega_{da1} = \omega_{da2} = \omega_{da}$. This makes the fourth term time independent, however it does not make the fifth and sixth term time independent. Note, $\Delta_{ai} = \omega_{ai} - \omega_{da}$ ($i \in 1,2$) are the detunings of the i th cavity mode and $\Delta_{b1} = \omega_{b1} - \omega_{db1}$ is the detuning of the membrane mode, from their respective driving field.

However, it can be observed that in the rotated frame the standard OM coupling terms become time dependent and the system will not reach a steady state. This makes the setup useless as an OM isolator. Hence, it can be deduced that for a tunable OM isolator, non-standard OM coupling should be used. We can deduce the form of the necessary conditions of the OM coupling terms to render them useful for isolation frequency tunable OM isolation.

Consider a general OM coupling term G_i for membrane in middle setup, which is function of $a_i, a_i^\dagger, b_1, b_1^\dagger$, and t , (for $i=1,2$). If $G'_i = e^{i\lambda X} G_i e^{-i\lambda X}$. Here, $X(a_i, a_i^\dagger, b_1, b_1^\dagger, t)$, is Hermitian operator and λ is some real number. Then, it is easy to prove using Baker-Campbell-Hausdorff formula that $\frac{dG'_i}{dt} = 0$ (i.e. the transformed term is time-independent) if $[G_i, X] = 0$ and $\frac{dG_i}{dt} = 0$. It can be seen that for the standard linear OM term $[G_i, X] \neq 0$ for $X = (\omega_{da1}ta_1^\dagger a_1 + \omega_{da2}ta_2^\dagger a_2 + \omega_{db1}tb_1^\dagger b_1)$ hence, it does not satisfy the condition needed. A term, $G_i = ga_i^\dagger a_i b_1^\dagger b_1$

satisfies the conditions and hence can be termed suitable for a tunable OM isolation. Such coupling is explored for QND measurement of phonons (after approximation using RWA (Under resolved-sideband limit) on quadratic coupling term) [95, 96]. Hence, we need to consider a quadratic OM coupling term as discussed in [95, 96]. We will explore this in further sections.

4.2 Tunable model with Quadratic Coupling

Optomechanical (OM) isolators with linear coupling have been studied theoretically [97, 1, 98, 99, 92, 100, 101, 102, 93] and also experimentally demonstrated in [103, 29, 104, 105, 106, 107, 108, 109]. Our physical setup for achieving OM isolation with tunable isolation frequency is that of a quadratically coupled optomechanical system with Hamiltonian similar to that used in a membrane-in-the middle (MIM) configuration. The system is driven by a strong optical coupling field with amplitude ϵ_i , frequency $\omega_{da,i}$, and phase ϕ_i and a weak coherent mechanical driving with amplitude ϵ_b , frequency ω_{db} , and phase ϕ_b for the membrane. In a MIM setup with optical cavities, a thin partially reflecting dielectric membrane with frequency ω_b , effective mass m , and finite reflectivity R is suspended inside the cavity which is formed by two fixed mirrors separated from each other by a distance L . When the membrane is placed at the anti-node of the cavity frequency (such that $\partial\omega_a/\partial x = 0$, x being the displacement of the membrane from its equilibrium position) the linear OM term $\propto a_i^\dagger a_i (b^\dagger + b)$ (where a_i and b refer to optical and mechanical modes, respectively) can be neglected [95, 110]. Thus the leading order OM coupling becomes quadratic in membrane displacement, with a coupling constant $g = \frac{8\pi^2 c}{L\lambda^2 [R/(1-R)]^{1/2}}$ [111, 112], where c is the speed of light in a vacuum and λ is the wavelength of the control field.

The relevant Hamiltonian can then be written as

$$\begin{aligned} H_q = & \omega_1 a_1^\dagger a_1 + \omega_2 a_2^\dagger a_2 + \omega_b b^\dagger b + J(a_1^\dagger a_2 \\ & + a_2^\dagger a_1) + g_1 a_1^\dagger a_1 (b^\dagger + b)^2 + g_2 a_2^\dagger a_2 (b^\dagger + b)^2 \\ & + i[\epsilon_1 e^{-i(\omega_{da,1}t - \phi_1)} a_1^\dagger + \epsilon_2 e^{-i(\omega_{da,2}t - \phi_2)} a_2^\dagger \\ & + \epsilon_b e^{-i(\omega_{db}t - \phi_b)} b^\dagger - h.c.] . \end{aligned} \quad (4.4)$$

This Hamiltonian is similar to Equation 4.2, exception being in the fifth and sixth term, where we consider quadratic coupling instead of linear coupling. This coupling has been experimentally achieved in MIM setup [95, 113, 110].

We transform the Hamiltonian H_q , in a frame co-rotating with the drive frequency, to $H'_q = U H_q U^\dagger - iU \frac{\partial U^\dagger}{\partial t}$ where $U = \exp[i(\omega_{da,1} t a_1^\dagger a_1 + \omega_{da,2} t a_2^\dagger a_2 + \omega_{db} t b^\dagger b)]$, as mentioned before. Using the Baker-Campbell-Hausdorff formula and the commutation properties of the bosonic operators, we find the following form of the Hamiltonian:

$$\begin{aligned} H'_q = & \Delta'_1 a_1^\dagger a_1 + \Delta'_2 a_2^\dagger a_2 + \Delta'_b b^\dagger b + J(a_1^\dagger a_2 + a_2^\dagger a_1) + 2g_1 a_1^\dagger a_1 (b^\dagger b) + 2g_2 a_2^\dagger a_2 (b^\dagger b) \\ & + i \left[\epsilon_1 e^{i\phi_1} a_1^\dagger + \epsilon_2 e^{i\phi_2} a_2^\dagger + \epsilon_b b^\dagger e^{i\phi_b} - h.c. \right] . \end{aligned} \quad (4.5)$$

Here, $\Delta'_i = \omega_i - \omega_{da,i} + g$ and $\Delta'_b = \omega_b - \omega_{db}$ are the modified detunings. In the following, we consider that the cavity driving frequencies are equal, i.e., $\omega_{da,1} = \omega_{da,2}$ and the OM coupling

constant are also equal, i.e., $g_1 = g_2 = g$, such that we can identify $G_i = ga_i^\dagger a_i (b^\dagger + b)^2$. For the same transformation matrix U as described before, we now have $U(G_i)U^\dagger = ga_i^\dagger a_i (b^{\dagger 2} e^{-2i\omega_{db}t} + b^\dagger b + bb^\dagger + b^2 e^{2i\omega_{db}t}) = 2ga_i^\dagger a_i b^\dagger b + ga_i^\dagger a_i$, where we used rotating wave approximation (RWA) and normal ordering. The RWA is applicable when cavity damping is small compared to the natural mechanical frequency, as discussed in [95, 114, 115].

To study how isolation works in such a system, we first obtain the Heisenberg-Langevin equations of the relevant field operators, taking into account the damping and corresponding noise terms:

$$\begin{aligned} \frac{d}{dt}a_1 &= \left\{ -\frac{\gamma_1}{2} - i[\Delta'_1 + 2gb^\dagger b] \right\} a_1 - iJa_2 \\ &\quad + \epsilon_1 e^{i\phi_1} + \sqrt{\gamma_1} a_{\text{in},1} , \end{aligned} \quad (4.6)$$

$$\begin{aligned} \frac{d}{dt}a_2 &= \left\{ -\frac{\gamma_2}{2} - i[\Delta'_2 + 2gb^\dagger b] \right\} a_2 - iJa_1 \\ &\quad + \epsilon_2 e^{i\phi_2} + \sqrt{\gamma_2} a_{\text{in},2} , \end{aligned} \quad (4.7)$$

$$\begin{aligned} \frac{d}{dt}b &= \left(-\frac{\gamma_b}{2} - i[\Delta'_b + 2g(a_1^\dagger a_1 + a_2^\dagger a_2)] \right) b \\ &\quad + \epsilon_b e^{i\phi_b} + \sqrt{\gamma_b} b_{\text{in}} . \end{aligned} \quad (4.8)$$

Here, $a_{\text{in},1}$, $a_{\text{in},2}$ and b_{in} are the input noise fields with mean values equal to zero, γ_i and γ_b are the damping rates of i th cavity mode and the membrane mode, respectively.

In the strong driving limit (i.e., when the control field amplitude is very large compared to the probe field amplitude), we can consider factorization assumption (i.e. $\langle ca \rangle = \langle c \rangle \langle a \rangle$) of two annihilation operators a and c . In such a scenario, the mean number of excitation in cavity modes and the membrane, at the steady state, are:

$$\begin{aligned} \langle a_1 \rangle &= \alpha_1 = \frac{\left(\frac{\gamma_2}{2} + i\Delta''_2 \right) \epsilon_1 e^{i\phi_1} - iJ\epsilon_2 e^{i\phi_2}}{\left(\frac{\gamma_1}{2} + i\Delta''_1 \right) \left(\frac{\gamma_2}{2} + i\Delta''_2 \right) + J^2} , \\ \langle a_2 \rangle &= \alpha_2 = \frac{\left(\frac{\gamma_1}{2} + i\Delta''_1 \right) \epsilon_2 e^{i\phi_2} - iJ\epsilon_1 e^{i\phi_1}}{\left(\frac{\gamma_1}{2} + i\Delta''_1 \right) \left(\frac{\gamma_2}{2} + i\Delta''_2 \right) + J^2} , \\ \langle b \rangle &= \beta = \frac{\left(\epsilon_b e^{i\phi_b} \right)}{\left(\frac{\gamma_b}{2} + i\Delta''_b \right)} . \end{aligned} \quad (4.9)$$

Here, $\Delta''_i = \Delta'_i + 2g\langle b^\dagger b \rangle$ and $\Delta''_b = \Delta'_b + 2g\left(\langle a_1^\dagger a_1 + a_2^\dagger a_2 \rangle\right)$ (detunings and frequency shifts due to the optomechanical interaction). We have assumed $\Delta''_i \approx \Delta''_b$ (analogous to that used in the resolved sideband limit) and $\gamma_i, \gamma_b, g \ll \Delta'_b$ ($i \in 1, 2$). Note that β is complex, and with a proper choice of phase of the mechanical drive, we can make $\beta \in \mathbb{R}$.

4.3 Non-Reciprocity and control of isolation frequency

To investigate the nonreciprocity at the steady state, we need to obtain the fluctuation dynamics of all the subsystems involved, namely, two cavity modes and the membrane. We consider that the driving field amplitudes are larger than the relevant decay rates. In

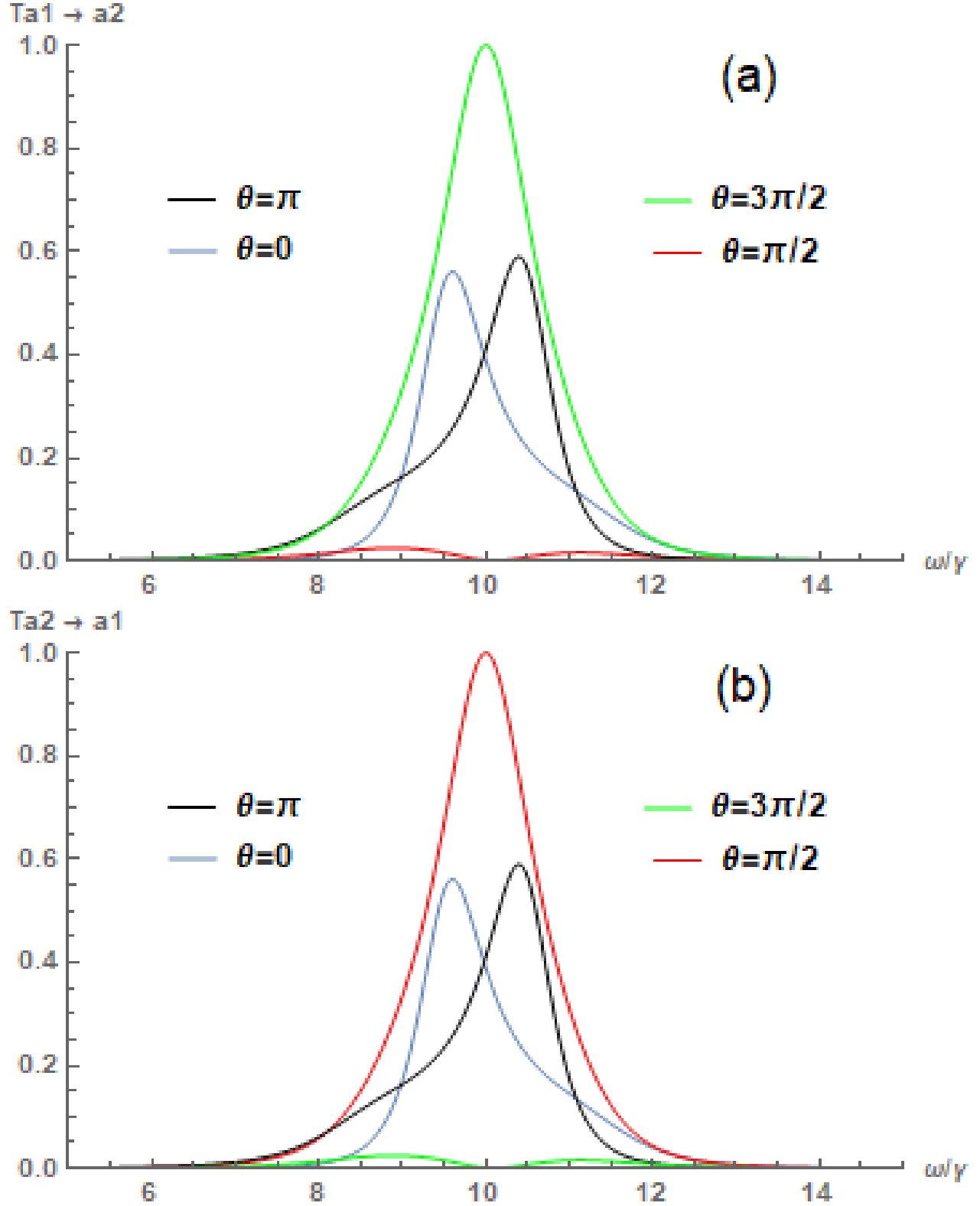


Figure 4.4: Plot for the scattering probabilities (T) with respect to normalized input frequency ω/γ for various θ . $\theta = 0$ (blue), $\theta = \pi/2$ (red), $\theta = \pi$ (black) and $\theta = 3\pi/2$ (green). The figure (a) depicts the scattering probability from the optical mode a_1 to a_2 , $T_{a1 \rightarrow a2}$, and (b) depicts the scattering probability from the optical mode a_2 to a_1 , $T_{a2 \rightarrow a1}$. The other parameters chosen are $J = |G_1| = |G_2| = \gamma_1/2 = \gamma_2/2 = \gamma_b/8 = \gamma/2$ and $\Delta_b'' = \Delta_1'' = \Delta_2'' = \Delta = 10\gamma$. Red and green curves in both subfigures showcase the non reciprocity. It is to be noticed when one is equal to 1 at 10γ the other is approximately 0 at 10γ .

this limit, we can linearize the (Equation 4.7-Equation 4.8), by expanding the annihilation operators as a sum of its steady state averages and the fluctuation operators, namely, $a_1 = \alpha_1 + \delta a_1$, $a_2 = \alpha_2 + \delta a_2$, $b = \beta + \delta b$. Substituting them in the (Equation 4.7-Equation 4.8), the linearized quantum Langevin equations can be written as:

$$\begin{aligned} \frac{d}{dt}\delta a_1 &= \left(-\frac{\gamma_1}{2} - i\Delta_1''\right)\delta a_1 - iG_1(\delta b + \delta b^\dagger) \\ &\quad - iJ\delta a_2 + \sqrt{\gamma_1}a_{\text{in},1}, \end{aligned} \quad (4.10)$$

$$\begin{aligned} \frac{d}{dt}\delta a_2 &= \left(-\frac{\gamma_2}{2} - i\Delta_2''\right)\delta a_2 - iG_2(\delta b + \delta b^\dagger) \\ &\quad - iJ\delta a_1 + \sqrt{\gamma_2}a_{\text{in},2}, \end{aligned} \quad (4.11)$$

$$\frac{d}{dt}\delta b = \left(-\frac{\gamma_b}{2} - i\Delta_b''\right)\delta b + \sqrt{\gamma_b}b_{\text{in}}. \quad (4.12)$$

Here, $G_1 = g\alpha_1\beta = |G_1|e^{i\theta_1} = |G_1|$ and $G_2 = g\alpha_2\beta = |G_2|e^{i\theta_2} = |G_2|e^{i\theta}$ (Note, that we have considered β as a real number considering particular phase of the driving field ϕ_b). Here $\theta = \theta_2 - \theta_1$ is the phase difference between G_1 and G_2 . These phases can be easily related to those ϕ_i of the driving fields, and hence controllable using the driving field, discussed later (see in section 4.4).

The Equation 4.11-Equation 4.12 can be solved in Fourier domain. We first write them in the index notation,

$$\dot{V}_i = -M_{ij}V_j + \Gamma_{ij}V_{j,\text{in}}, \quad (4.13)$$

where $i, j = 1, 2, \dots, 2n$ (where $n = 3$ is the number of distinct modes in the system). Here the elements of fluctuation and input field vectors are arranged as $V = (\delta a_1, \delta a_2, \delta b, \delta a_1^\dagger, \delta a_2^\dagger, \delta b^\dagger)^T$

and $V_{\text{in}} = (a_{\text{in},1}, a_{\text{in},2}, b_{\text{in}}, a_{\text{in},1}^\dagger, a_{\text{in},2}^\dagger, b_{\text{in}}^\dagger)^T$, respectively. The matrix Γ is given by

$$\text{diag}(\sqrt{\gamma_1}, \sqrt{\gamma_2}, \sqrt{\gamma_b}, \sqrt{\gamma_1}, \sqrt{\gamma_2}, \sqrt{\gamma_b}).$$

By introducing the Fourier transform of the operators \hat{o} , as

$$\tilde{o}(\omega) = \frac{1}{\sqrt{2\pi}} \int_{-\infty}^{+\infty} o(t)e^{i\omega t} dt, \quad (4.14)$$

$$\tilde{o}(\omega)^\dagger = \frac{1}{\sqrt{2\pi}} \int_{-\infty}^{+\infty} o(t)^\dagger e^{i\omega t} dt, \quad (4.15)$$

the matrix Eq. (4.13) can be rewritten in the frequency domain as,

$$\tilde{V}_i(\omega) = (M - i\omega I)_{ij}^{-1} \Gamma_{jk} \tilde{V}_{\text{in},k}(\omega), \quad (4.16)$$

where I is the identity matrix.

According to the input-output formalism [28], the relationship between internal, input and output fields under the first Markov approximation is given as

$$o_{\text{out}} + o_{\text{in}} = \sqrt{\gamma_o} \delta o, \quad (4.17)$$

where, $o \equiv a_1, a_2, b$ and the γ_o are the damping rates for the respective o . Using this in (4.16), and defining $\tilde{V}_{\text{out}} = \left(a_{\text{out},1}, a_{\text{out},2}, b_{\text{out}}, a_{\text{out},1}^\dagger, a_{\text{out},2}^\dagger, b_{\text{out}}^\dagger \right)^T$, we find that

$$\begin{aligned} \tilde{V}_{\text{out},i}(\omega) &= \sum_{l=1}^{2n} U_{i,l} \tilde{V}_{\text{in},l}(\omega) , \\ U_{i,l} &= [\Gamma_{ij}(M - i\omega I)_{jk}^{-1} \Gamma_{kl} - \delta_{il}] . \end{aligned} \quad (4.18)$$

To obtain the spectrum of scattering probabilities, we now invoke the two-frequency correlation of various elements of the V -matrices. Let us start with

$$\tilde{V}_{\text{out},i}^\dagger \tilde{V}_{\text{out},j} = \sum_{l,m=1}^{2n} U_{i,l}^* U_{j,m} \tilde{V}_{\text{in},l}^\dagger \tilde{V}_{\text{in},m} , \quad (4.19)$$

$$\text{or, } \langle \tilde{V}_{\text{out},i}^\dagger \tilde{V}_{\text{out},j} \rangle = \sum_{l=1}^{2n} U_{i,l}^* U_{j,l} \langle \tilde{V}_{\text{in},l}^\dagger \tilde{V}_{\text{in},l} \rangle , \quad (4.20)$$

where we have used the fact that $\langle \tilde{V}_{\text{in},i}^\dagger \tilde{V}_{\text{in},j} \rangle$ are non-zero only for $i = j$.

Defining $S_{i,\text{out}}(\omega) = \int d\omega' \langle \tilde{V}_{\text{out},i}^\dagger(\omega') \tilde{V}_{\text{out},i}(\omega) \rangle$ and $S_{i,\text{in}}(\omega) = \int d\omega' \langle \tilde{V}_{\text{in},i}^\dagger(\omega') \tilde{V}_{\text{in},i}(\omega) \rangle$ ($i \in 1, 2, 3$), we now obtain following expression, relating the frequency correlations at the input and output ports:

$$S_{\text{out}}(\omega) = T(\omega) S_{\text{in}}(\omega) + S_{\text{vac}}(\omega) , \quad (4.21)$$

where S_{in} , S_{out} , and $S_{\text{vac}}(\omega) = (s_{a1,\text{vac}}(\omega), s_{a2,\text{vac}}(\omega), s_{b,\text{vac}}(\omega))^T$ are the n -component column matrices, with the number of modes in $n = 3$. The T denotes the scattering probability matrix. The element T_{ij} of this matrix represents the probability to scatter from the i th mode to the j th mode, and is given by

$$T_{ij} = |U_{i,j}|^2 + |U_{i,j+n}|^2 , \quad (4.22)$$

for $i, j \in 1, 2, 3$. Similarly, the elements of $S_{\text{vac}}(\omega)$ can be written in terms of the elements of the U -matrix, as

$$S_{i,\text{vac}}(\omega) = |U_{i,i+n}(\omega)|^2 + |U_{i,i+n+1}(\omega)|^2 + \dots + |U_{i,i+2n}(\omega)|^2 . \quad (4.23)$$

In Fig. 4.2(a), we display the spectra of scattering probability T_{12} , i.e. from the cavity mode a_1 to a_2 for various values of the phase difference θ between the effective optomechanical coupling strengths G_1 and G_2 . In Fig. 4.2(b), we display the same for T_{21} . We have assumed that $\Delta_b'' = \Delta_1'' = \Delta_2'' = \Delta$.

It is to be noticed that for $\theta = \pi/2$, the scattering probability $T_{12} = 0$ when the frequency of the signal to be isolated becomes $\omega = \Delta$, while T_{21} becomes unity for the same (Compare Red curves in both subfigures). This means that for a certain frequency, one can achieve a complete transmission of the field from the mode a_2 to a_1 , but zero transmission vice versa. This is the signature of optical isolation. This scenario can be reversed by changing the phase difference θ to $3\pi/2$ (one may compare green curves in the subfigures). Generally, optical isolation occurs for $\theta = (2k + 1)\pi/2$, for all integers k , while for $\theta \equiv \pi/2 \pmod{2\pi}$,

the transmission vanishes from the mode a_1 to a_2 and for $\theta \equiv 3\pi/2(\text{mod } 2\pi)$, the reverse situation is achieved. This asymmetry in transmission profile can be understood in terms of interference phenomenon. At a particular input signal frequency (here $10\omega/\gamma$) and a particular phase difference of the control (driving) fields as given in section 4.4, one of the output optical modes exhibits anti-resonance while the other displays resonance. The driving acting on one of the cavity interferes destructively with the feedback due to coupling from another cavity and anti-resonance occurs for the output optical mode from it. While, in opposite direction there is constructive interference or resonance on the output mode from it. This is the reason for isolation in OM isolator [30]. As the signal is weak, it does not cause any additional mode oscillation.

In Fig. 4.3 complete transmission profiles for a large range of signal frequency ω and the modified optomechanical coupling phase θ are compared for the device with different parameter sets. It should be noted that the profile shown in Fig. 4.3 (a)-(b) is similar to that reported in [1]. However, by increasing the decay rate, we can easily see in Fig. 4.3 (c)-(d) that the isolation profile is highly suppressed. This makes our proposal better suited for isolation, due to the enhanced suppression compared to [1].

The very fact that the membrane mode is driven by an external field provides us an additional handle to control the isolation frequency at which one achieves non-reciprocity in either direction. We show in Fig. 4.5, how the isolation frequency varies with change in Δ for $\theta = \pi/2$. It is clearly seen that one can achieve optical isolation at $\omega = \Delta$, for any chosen value of Δ . In previous proposals, the isolation frequency was fixed during fabrication of the OM isolator. The mechanical drive along with the quadratic coupling (under the RWA) provides us an extra advantage to control the mechanical mode frequency (technically speaking, the detuning Δ). Choosing different values of Δ for our proposal corresponds to just setting up the frequencies of the driving fields externally. Theoretically, the frequency can be tuned until the resolved sideband regime is not violated. It is to be noted that, in this scenario, the dependence of the isolation profile on θ remains the same, as displayed in Fig. 4.4. It is further emphasized that it is possible to tune the isolation frequency and direction, by suitable choices of phase and frequency of the external driving fields of cavities as well as the membrane.

It was indicated that the isolation can be better obtained in systems with larger decay rates [see Fig. 4.3]. However there is an optimum value of the decay rate, beyond which the isolation does not become complete. We show in Fig. 4.6 how the isolation gets maximized at a certain decay rate γ_b , for $\theta = \pi/2$ or $3\pi/2$ and the signal frequency $\omega = \Delta$. We must emphasize here that the isolation happens when the condition $G_i = \gamma_1/2 = \gamma_2/2$ is satisfied. Thus for a fixed value of the fundamental decay rates γ_i , one can change the values of $|G_i|$, such that the above condition is satisfied. This can be done, for example, using, by suitably controlling α_i , i.e., by choosing suitable values of the amplitudes ϵ_i and phases ϕ_i of the cavity control fields [see Eq. (4.9)].

4.4 Phase difference in optomechanical couplings

The role of the phase of modified optomechanical coupling is very well explained in [29]. Note that we have used a parameter domain, as $\Delta = 10\gamma$; $J, g = \gamma/2$, satisfying a large detuning

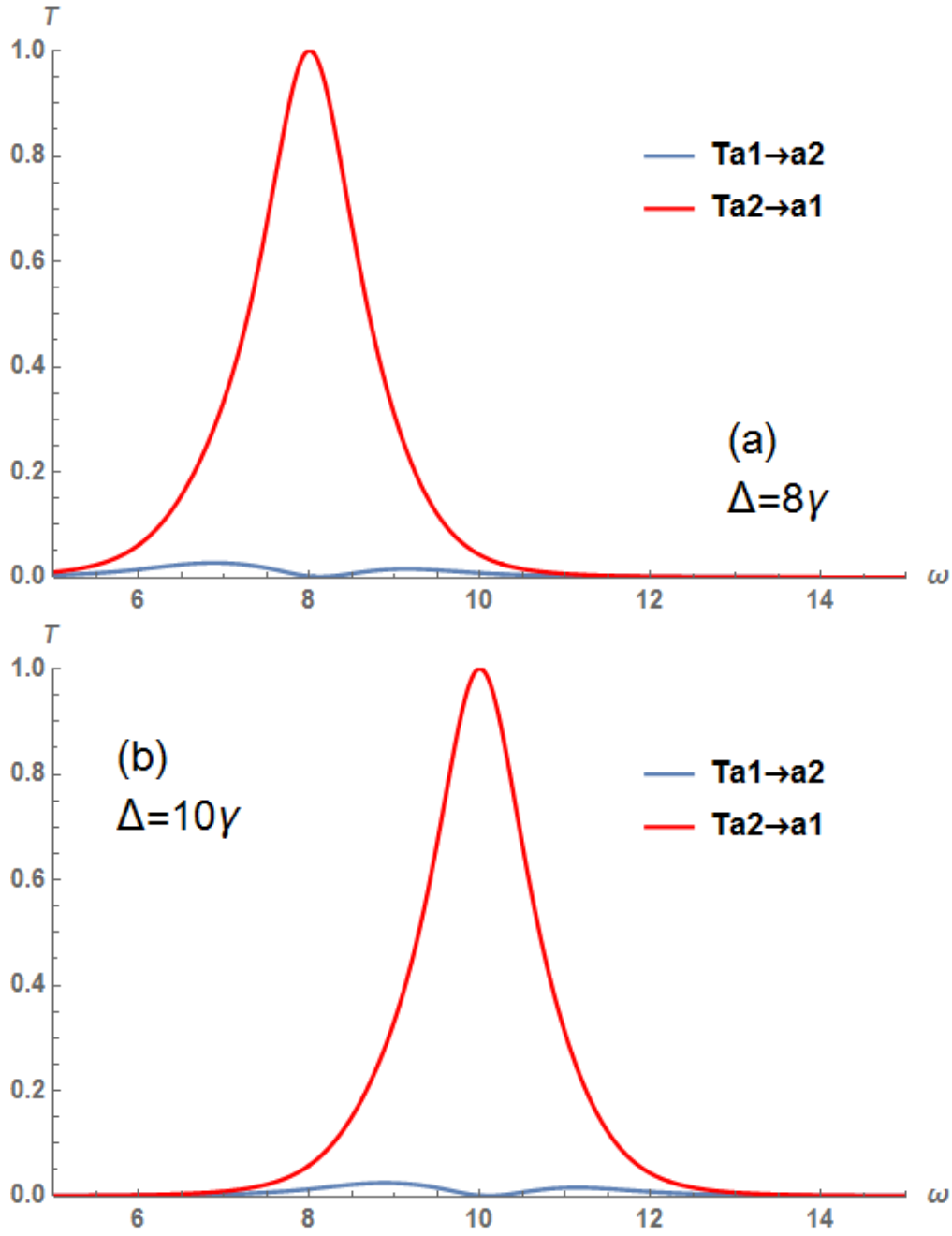


Figure 4.5: Plot of Scattering probability T with respect to ω/γ for various Δ . $\Delta = 8\gamma$ (Blue), $\Delta = 10\gamma$ (Red) and $\Delta = 12\gamma$ (Black). (a) Depicts the scattering probability from optical mode a_1 to a_2 , $T_{a1 \rightarrow a2}$ and (b) Depicts the scattering probability from optical mode a_2 to a_1 , $T_{a2 \rightarrow a1}$. The other parameters chosen are $J = |G_1| = |G_2| = \gamma_1/2 = \gamma_2/2 = \gamma_b/8 = \gamma/2$, $\theta = \pi/2$ and $\Delta'_b = \Delta'_1 = \Delta'_2 = \Delta$. The reader is advised to compare same colors. It demonstrates that the device is frequency-tunable.

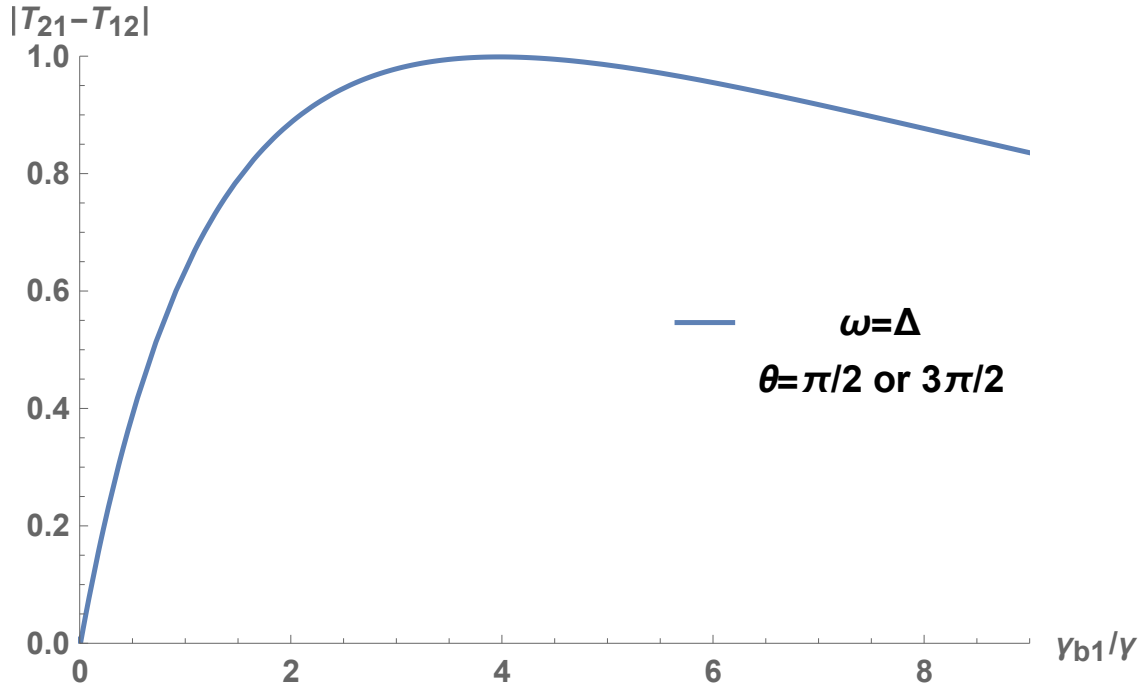


Figure 4.6: Variation of absolute difference of scattering probabilities $|T_{21} - T_{12}|$ with respect to γ_b/γ . The other parameters chosen are $J = |G_1| = |G_2| = \gamma_1/2 = \gamma_2/2 = \gamma/2$, $\theta = \pi/2$ or $3\pi/2$ and $\omega = \Delta_b'' = \Delta_1'' = \Delta_2'' = \Delta$. Note that these are the parameters which are the requirement for isolation as depicted in Fig. 4.4. Maximum isolation occurs at $\gamma_b/\gamma = 4$.

limit $\Delta \gg J, \gamma, g$. Hence, from Eq. (4.9), we have, for $\epsilon_1 = \epsilon_2 = \epsilon$,

$$\begin{aligned}\alpha_1 &\approx \frac{\Delta\epsilon}{D} e^{i(\phi_1 + \pi/2 - \zeta)}, \\ \alpha_2 &\approx \frac{\Delta\epsilon}{D} e^{i(\phi_2 + \pi/2 - \zeta)}.\end{aligned}\quad (4.24)$$

Here, the denominator in the expressions of α_1 and α_2 [see Eqs. (4.9)] is written as $De^{i\zeta}$, and the phase $\pi/2$ appears in the numerator. Clearly, the phase difference between α_1 and α_2 is given by $\phi_1 - \phi_2$. This is exactly the same as $\theta_1 - \theta_2$, as used in the expressions of the effective optomechanical coupling: $G_1 = (g\beta)\alpha_1 = |G_1|e^{i\theta_1}$ and $G_2 = (g\beta)\alpha_2 = |G_2|e^{i\theta_2}$, while the optomechanical coupling g is a real quantity. The notations are as discussed in section 4.3. The driving fields therefore create an effective phase-difference in the optomechanical couplings, which in turn, leads to non-reciprocity.

4.5 Conclusion

Proposal	Q	MD	RD
[116, 117](E)			✓
[118](TP)			✓
[119](TP)	✓		✓
[120, 121, 122, 123, 124, 125, 126](E)		✓	
[127, 128, 129](TP)		✓	
[86, 130, 131, 132](TP)	✓	✓	

Table 4.1: Table listing the experiments (E) and theoretical proposals for the experiment (TP) which could be useful to achieve the physical system depicted in this article. Q stands for quadratic coupling, MD stands for mechanical driving, RD stands for reversed dissipation.

The dissipation rate of optical cavity mode is usually larger than that of the mechanical one ($\gamma_i > \gamma_b$). The reversed dissipation regime considers the inverse regime, i.e., $\gamma_b > \gamma_i$. It inverts the roles of photons and phonons in the OM system. It can be seen in Fig. 4.6 that a particular value of the mechanical decay rate greater than the optical decay rate is needed to achieve optimal isolation. Moreover, the requirement is stringent as revealed in Fig. 4.6. In fact, such a reversed dissipation regime is a non-standard requirement for achieving optomechanical non-reciprocity and isolation [1, 92, 106]. Reversed dissipation regime has been experimentally achieved in [116, 117] and experimental proposals to achieve them are found in [119, 118]. In addition to reversed dissipation, one needs quadratic coupling and coherent mechanical driving to implement our proposal, as can be seen from the previous section. Note that optical non-reciprocity using piezo-optomechanical systems has been recently discussed [133], where the mechanical mode is driven and the isolation has been controlled using piezo-electric coupling coefficient, instead of a coherent drive of the membrane. In Table. 4.1 we summarize different theoretical proposals and experiments which would lead to the direction of achieving the tunable-frequency isolator device discussed in this article. In summary, it was

shown that the isolation frequency, (i.e., the frequency of the input field at which maximum non-reciprocity occurs) is limited to a small window which is dependent on inherent system parameters, namely, the fundamental frequency of the membrane. This frequency could not be dynamically manipulated because it is fixed during fabrication of the membrane. We here have shown that this issue can be resolved by driving the membrane by an external field and using a quadratic OM coupling in the resolved sideband limit ($\omega_b \gg \gamma_i$). The suitable detuning of the mechanical drive allows the control of isolation frequency. Moreover, it can be seen from Fig. 4.3, that we achieve enhanced suppression due to the quadratic coupling, compared to [1] which considers linear coupling and does not consider a mechanical driving of the membrane. Note that we can use this device as OMIT or OMIA as required, by just changing the phase difference and keeping other parameters as given in this paper. This device has potential applications for quantum communication and sensing, where tunability of isolation frequency (wavelength) is required.

Chapter 5

Simulation of Exceptional Point Sensors on Quantum Computer

Quantum operations can be classified as either unitary or non-unitary. Much attention has been given to unitary operations in physics. In fact, in a quantum computer, quantum gates are made up of unitary operations. However, there are several reasons to consider non-unitary transformations. Open quantum systems exhibit non-unitary dynamics [134, 135, 136, 137, 136]. In quantum chemistry, as well, non-unitary evolutions are often studied [138, 139, 140]. Quantum speedups have also been proposed in nonlinear quantum computing through non-unitary Abrams-Lloyds gate [141, 142]. Quantum machine learning needs non-unitarity and non-linearity [143, 144, 145, 146] too.

Consider a transformation, represented by e^{-iA} . If A is Hermitian, this transformation becomes unitary and vice-versa. However, for e^{-iA} to be non-unitary, its generator A must be non-Hermitian. This requires one to study the behaviour non-Hermitian matrices. Usually, non-hermiticity does not guarantee that its eigenvalues would be real, unlike the Hermitian ones. In 1998, [147] showcased that there exist certain non-Hermitian Hamiltonians that have real eigenvalues. This sparked a debate around postulates of quantum mechanics and explorations of such systems in quantum domain. It was shown in [12] that all such Hamiltonians, if diagonalizable, are related to Hermitian ones by similarity transformations, and hence are “pseudo-Hermitian”. On the other hand, the non-Hermitian Hamiltonians, which are non-diagonalizable, lie at degeneracy called the non-Hermitian degeneracy or exceptional points (EP) in literature. Such an operator has degeneracy in both eigenvalues and eigenvectors of the operator. In this paper, we will consider these non-diagonalizable systems in the context of quantum sensing, particularly for estimation of an unknown parameter.

For the best possible estimate of any parameter γ , there exists the so-called Quantum Cramer-Rao Bound (QRCB) [58, 57] which is given by the inverse of the quantum Fisher information (QFI). This can be represented as

$$\Delta\gamma \leq \frac{1}{\sqrt{QFI_\gamma}} . \quad (5.1)$$

It can be observed that higher the QFI , less the variance ($\Delta\gamma^2$) and hence more precise the estimation. Hence, a very high QFI shows promise in its exploitation for precise sensing.

It was first theoretically pointed out in [148] that the EPs can be utilized for parameter estimation as QFI may diverge at EP of a non-Hermitian non-diagonalizable Hamiltonian, in absence of noise. Note that the divergence of QFI does not violate Heisenberg's uncertainty principle as the latter is concerned with simultaneous measurement of two canonically conjugate physical variables while QRCB is concerned with precision of measurement of a particular physical variable [149, 150]. Later, it was deduced in [55] that QFI does not necessarily exhibit any divergence at EP, and this result was negated by a more accurate analysis in [56] that shows that the QFI indeed diverges. This debate of divergence is also highlighted in [151, 37]. In fact, the divergence of QFI is related to the expansion of a perturbed eigenfunctions and eigenvalues in Puiseux series rather than Taylor series for any perturbations at EPs, as was already shown in [64] and which was often overlooked in literature.

The possibility of divergence of the QFI at EP motivates us to explore how to implement non-Hermitian dynamics in real quantum computers. Till recent times, the non-Hermitian systems have been mostly explored in optical systems through an analogous connection between Helmholtz equation and Schrodinger equation [40]. There have been a few experimental considerations of EPs in certain quantum systems too [43, 152]. Here, we democratize access to such exotic systems using quantum computers. Note that these computers, which are accessible via cloud, operate unitarily. In this paper, we show that it is indeed possible to implement the nonunitary dynamics, generated by non-Hermitian Hamiltonian, in the existing architecture itself. We propose use of ancillary qubits in this regard. We employ post-selection strategy to extract the state of the EP system, that will be used to calculate the QFI and to evaluate the performance of the system for parameter estimation. We also provide a circuit model that we use in our cloud experiments in the IBM Q Experience platform.

The achievable precision of a quantum parameter estimation protocol is limited by the noise in the system, which could degrade the QFI . The early EP sensing protocols did not consider the effect of noise. Later, various studies related to impact of noise on such sensors were reported [63, 54, 55, 56]. In [54], the authors showed that a non-Hermitian non-reciprocal system delivers an unbounded signal-to-noise ratio (SNR) and thereby a better sensing performance compared to the reciprocal ones, even when it operates away from the EP. On the contrary, in this paper, we focus on studying the behavior of the QFI , and not the SNR, in presence of noise. Note that, though for certain parameter domain, the QFI becomes numerically identical to the SNR, they are fundamentally different quantities. While the QFI is related to the amount of information that can be extracted from a quantum system about a particular parameter of interest, the SNR is a measure of the relative strength of a signal to the level of background noise. Thus, in the context of quantum sensing, the QFI is a more suitable quantity than the SNR to characterize the performance of the quantum sensor, more so when the quantum noise dominates over the classical noise and when their sensitivity to changes in a parameter is governed by the quantum rules, e.g., the Heisenberg uncertainty principle.

The structure of the chapter is as follows. In section 5.1 we will describe the theory related to simulation of non-unitary dynamics using ancilla based method [153]. In section 5.2 we describe the gate based quantum computing model. In the section 5.3, we will present the results of our simulation of dynamics of non-Hermitian systems using IBM Q Experience. We will explicitly show the divergence of QFI at exceptional points. Then in section 5.4,

we discuss effects of various noise models on EP sensors. We will discuss in section 5.6 the limitations of the ancilla-based method used in this paper. Finally, in section 5.7 we conclude the chapter. For the theory and preliminaries related to this chapter the reader can refer to chapter 3.

5.1 Simulating non-unitary dynamics

Consider Non-Hermitian Hamiltonians, where the adjoint of the Hamiltonian is not equal to the Hamiltonian itself $((NH)^\dagger \neq NH)$.

The objective of this simulation is to determine the resulting state, denoted as $\frac{1}{\mathcal{N}}|\phi\rangle$, which is obtained by applying the operator $\exp[\frac{-i(NH)t}{\hbar}]$ to the input state $|\xi\rangle$. Here, $|\xi\rangle$ represents the initial state, \mathcal{N} is a normalization constant, and t is the time parameter. It is important to note that although the evolution is non-unitary, both the input and output states are pure states under our consideration.

Let us consider the following steps:

(a) *Singular value decomposition:* Our initial step is to compute the non-unitary time evolution matrix (referred to as $NUTE$), which is defined as $NUTE = \exp[\frac{-i(NH)t}{\hbar}]$. For the purpose of simulation, we will adopt the values $t = 1$ and $\hbar = 1$ from now on. This time evolution matrix can be expressed as a sequence of three distinct evolutions using the singular value decomposition (SVD), namely $NUTE = U\Sigma V^\dagger$. Here U and V^\dagger are unitary matrices and can easily be used as gates in gate based quantum computer. However, as the operation Σ is a diagonal matrix with non-negative entries (also called singular values), this matrix is not necessarily unitary and simulation of such an evolution is not possible on a quantum computer using unitary gates. Moreover, the singular values need not always be less than one. The requirement of singular values to be less than or equal to 1 arises from the fact that they are used to parameterize unitary gate in the required circuit. Consider a to be a singular value of Σ . Then the corresponding parameterized unitary gate can be written in the following form, iff $a \leq 1$:

$$U(a) = \begin{pmatrix} a & -\sqrt{1-a^2} \\ \sqrt{1-a^2} & a \end{pmatrix}. \quad (5.2)$$

(b) *L^2 -normalization:* We will next L^2 -normalize the $NUTE$ matrix using the maximum singular value, $\max(\Sigma)$. We denote this normalized form as $NUTE_N$. The singular values of a such a L^2 -normalized matrix (of 2 dimensions) are always 1 and m . where $m \leq 1$ (equality arising when $NUTE$ is unitary). Note that such a normalization does not affect the output state as the output is not affected when the transformation is multiplied by a scalar constant.

(c) *Introduction of an ancilla:* Simulating the $NUTE_N$ in its current form still may not be possible in a quantum computer. To circumvent this issue, we next dilate the Hilbert space of the system by using an ancillary system. Note that the joint operation of the system and ancilla can be unitary, while that for the system itself remains non-unitary. We start with the joint state $|\xi\rangle|0\rangle$ of the system and the ancilla.

(d) *Two-qubit operation:* We create a two-qubit gate $C\Sigma = U(1) \oplus U(m)$, where $U(1) = I$ (I is an identity matrix) and $U(m)$ is also a unitary matrix. Note that $C\Sigma$ is unitary because the direct sum of unitary matrices is always unitary.

Now we consider the operation

$$(U \otimes I)[C\Sigma](V^\dagger \otimes I) \quad (5.3)$$

acting on the state $|\xi\rangle|0\rangle$. This is described in Fig. 5.1(a). This operation can be written as $(U \otimes I)[(\Sigma \otimes I) + (\Sigma' \otimes ZX)](V^\dagger \otimes I)$, because,

$$C\Sigma = U(1) \oplus U(m) = \begin{pmatrix} 1 & 0 & 0 & 0 \\ 0 & 1 & 0 & 0 \\ 0 & 0 & m & -\sqrt{1-m^2} \\ 0 & 0 & \sqrt{1-m^2} & m \end{pmatrix} = (\Sigma \otimes I) + (\Sigma' \otimes ZX), \quad (5.4)$$

where

$$\Sigma' = \begin{pmatrix} 0 & 0 \\ 0 & \sqrt{1-m^2} \end{pmatrix}. \quad (5.5)$$

Here Z and X are usual Pauli spin operators.

In presence of the ancilla, the operator $NUTE_N$ can then be revised as $U(C\Sigma)V^\dagger$. The output of this operation on $|\xi\rangle|0\rangle$ is then given by

$$(U\Sigma V^\dagger|\xi\rangle)|0\rangle - (U\Sigma' V^\dagger|\xi\rangle)|1\rangle = |\phi, 0\rangle + |\phi', 1\rangle, \quad (5.6)$$

where $|\phi'\rangle = -U\Sigma' V^\dagger|\xi\rangle$.

(e) *Post-selection*: We apply a post-selection protocol on the above output state such that the ancilla is projected into $|0\rangle$. This can be represented by the following expression:

$$(I \otimes P_0)(|\phi, 0\rangle + |\phi', 1\rangle) = |\phi, 0\rangle, \quad (5.7)$$

where $P_0 = |0\rangle\langle 0|$. Upon normalization (which is performed by the measurement operation itself), we have the state $\frac{1}{\mathcal{N}}|\phi, 0\rangle$ which is the required output from this non-Hermitian evolution. Here \mathcal{N} is given by

$$\mathcal{N} = \sqrt{(\langle\phi, 0| + \langle\phi', 1|)(I \otimes P_0)(|\phi, 0\rangle + |\phi', 1\rangle)} = \sqrt{\langle\phi, 0|\phi, 0\rangle}. \quad (5.8)$$

The probability of success of the post-selection protocol can be calculated as

$$\left| \frac{\langle\phi|\phi\rangle}{\sqrt{|\langle\phi|\phi\rangle|^2 + |\langle\phi'|\phi'\rangle|^2}} \right|^2. \quad (5.9)$$

We apply the repeat-until-success strategy to extract out the $|\phi', 1\rangle$ state through post-selection.

(f) *Calculation of the QFI*: We intend to find the QFI for parameter estimation using a two-level non-Hermitian sensor. We choose one of the eigenstates, denoted by $|\phi_+(\gamma)\rangle$, of the two-level system. To calculate QFI , we first obtain the expression of the fidelity as

$$F = |\langle\tilde{\phi}_+(\gamma + \delta\gamma)|\phi_+(\gamma)\rangle|^2, \quad (5.10)$$

where $\langle\tilde{\phi}_+(\gamma + \delta\gamma)| = \langle\chi_+(\gamma + \delta\gamma)|$ is the left eigenvector, corresponding to the right eigenvector $|\phi_+(\gamma + \delta\gamma)\rangle$, according to the bi-orthogonality rules [see section 1.2]. The fidelity can be found on the actual quantum computing hardware using a SWAP test, as described in Fig. 5.1(b) [154]. The QFI is then calculated numerically by using the equation

$$QFI = \lim_{\delta\gamma \rightarrow 0} \frac{D_b^2}{4(\delta\gamma)^2}, \quad (5.11)$$

where $D_b^2 = 2 - 2F$ is known as Bures distance [58, 57].

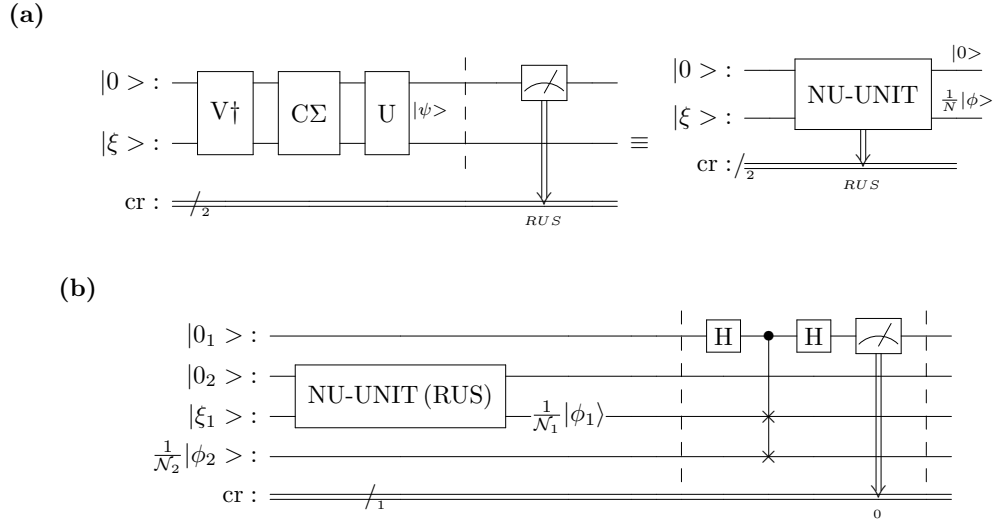


Figure 5.1: (a) The circuit diagram for simulating non-unitary evolution. We decompose the non-unitary transformation using SVD transform into $U\Sigma V^\dagger$. Then using the procedure as mentioned in the text, we apply the operations on the input state $|\xi, 0\rangle$ to obtain $|\psi\rangle$. This is followed by a post-selection protocol applied on the output using "Repeat until success" (RUS) method. Here we discard all measurements results which project the ancilla in the state $|1\rangle$, and repeat the procedure till we get the ancilla to be in the state $|0\rangle$. This collapses the state to $\frac{1}{N}|\phi, 0\rangle$ which contains the required state due to non-unitary evolution. On the right hand side, we schematically represent the non-unitary gate. Note that 'cr' in the circuit refers to classical register. (b) The circuit diagram for the SWAP test to measure fidelity between two states i.e. $F = \frac{1}{|\mathcal{N}_1\mathcal{N}_2|^2}|\langle\phi_2|\phi_1\rangle|^2$. We can consider $\frac{1}{N_1}|\phi_1\rangle$ and $\frac{1}{N_2}|\phi_2\rangle$ to be the states as given in Eq. 5.10. The circuit between the dashed vertical barriers represents SWAP test. We specifically mention \mathcal{N} in denominator to show that non-unitary circuits un-normalize input states and we need to consider normalization of such output states.

5.2 Gate based Quantum Computing

In this section we will discuss the gate based model of quantum computing as it will be used later in this chapter. Before we go forward, for a wider picture let us know about models of classical computation. There are several models of classical computing that have been developed over the years. Here are some of the most common models:

- **Turing Machine:** Proposed by Alan Turing in 1936, the Turing machine is a theoretical model of a computing device that manipulates symbols on an infinite tape according to a set of rules. It is considered the foundation of classical computing and can simulate any algorithmic computation.
- **Von Neumann Architecture:** This model, also known as the von Neumann machine, is the basis for most modern computers. It was proposed by John von Neumann in the late 1940s and consists of a central processing unit (CPU), memory, input/output devices, and a stored program. The von Neumann architecture allows instructions and data to be stored in the same memory, enabling the sequential execution of instructions.
- **Random Access Machine (RAM):** The RAM model is a theoretical abstraction of a computer that performs computations by executing a sequence of instructions. It assumes a machine with an unlimited number of registers and allows direct access to any memory location. RAM is used to analyze the time complexity of algorithms and is a common model for theoretical computer science.

there are many other models of classical computation, but it is out of scope of this thesis. Now, having learned about the classical models of computation, let us note down quantum models of computation.

- **Gate based Model:** This is the most widely used model of quantum computation. It represents computations as a sequence of quantum gates, which are analogous to classical logic gates. Quantum circuits operate on quantum bits, or qubits, which can exist in superpositions of 0 and 1, allowing for parallel computation and quantum entanglement.
- **Quantum Turing Machine:** The quantum Turing machine (QTM) is a theoretical model that extends the classical Turing machine to include quantum operations. QTM consists of an infinite tape and a quantum head that can read, write, and manipulate quantum states. It serves as a theoretical framework for studying the limits and capabilities of quantum computation.
- **Quantum Annealing:** Quantum annealing is a specific approach to solving optimization problems using quantum systems. It leverages the phenomenon of quantum tunneling to find the lowest energy state of a given problem's landscape. Quantum annealing machines, such as D-Wave systems, are designed to perform this type of computation.
- **Measurement-Based Quantum Computation:** In this model, quantum computations are carried out by applying a sequence of measurements to an entangled quantum

state, known as a cluster state. By performing measurements in a specific order, the computation unfolds deterministically. Measurement-based quantum computation has the advantage of being resilient to certain types of quantum errors.

For the simulation of EP dynamics in this chapter we will be focusing on the gate based model of quantum computation. In current day and age we are able to access quantum computing hardware through cloud. We will avoid the details of gate based model of quantum computation, and suggest the reader to refer to [155].

5.3 Simulating EP sensing dynamics

5.3.1 Single EP

In this Section, we show how to implement the different steps to simulate a non-unitary evolution based on a non-Hermitian Hamiltonian, as mentioned in the previous Section, using the IBM Q Experience. We will investigate two different Hamiltonians for EP sensing. We start with the following Hamiltonian:

$$NH_1 = \begin{pmatrix} 0 & 0.5 + \gamma \\ 0.5 - \gamma & 0 \end{pmatrix}, \quad (5.12)$$

where γ is the parameter that is to be estimated in this protocol. Therefore, the protocol in section 5.1 becomes more relevant when the non-unitary operation, that the state of the system is subjected to, is unknown, or in other words, the single-parameter Hamiltonian is rather unknown.

The matrix (5.12) is non-Hermitian as $NH_1 \neq (NH_1)^\dagger$. The eigenvectors of NH_1 are (after using normalization condition for bi-orthogonal systems: $\langle \phi | \chi \rangle = 1$) $|\phi_\pm\rangle = \frac{1}{\sqrt{2}} \left[\pm \frac{\sqrt{1-4\gamma^2}}{2\gamma-1}, 1 \right]^T$ and those of $(NH_1)^\dagger$ are $|\chi_\pm\rangle = \frac{1}{\sqrt{2}} \left[\mp \frac{\sqrt{1-4\gamma^2}}{2\gamma+1}, 1 \right]^T$, where T represents transposition. It should also be noted that $\langle \phi_\pm | \phi_\mp \rangle \neq 0$ unlike in the case of Hermitian operators (the same applies for eigenvectors of $(NH_1)^\dagger$, as well). However $\langle \phi_\pm | \chi_\mp \rangle = 0$. This is further elaborated in the section 1.3. We observe that this system exhibits the exceptional point degeneracy at $\gamma = 0.5$. Note that the eigenvalues of NH_1 are given by $\pm\sqrt{0.25 - \gamma^2}$.

The QFI for a single parameter γ in a bi-orthogonal system is defined as

$$QFI_\gamma = 4(\langle \partial_\gamma \tilde{\phi}_+ | \partial_\gamma \phi_+ \rangle - |\langle \partial_\gamma \tilde{\phi}_+ | \phi_+ \rangle|^2) = 4(\langle \partial_\gamma \chi_+ | \partial_\gamma \phi_+ \rangle - |\langle \partial_\gamma \chi_+ | \phi_+ \rangle|^2), \quad (5.13)$$

where $|\partial_\gamma \phi\rangle = \frac{\partial |\phi(\gamma)\rangle}{\partial \gamma}$ and $|\partial_\gamma \chi\rangle = \frac{\partial |\chi(\gamma)\rangle}{\partial \gamma}$. Note that this equation matches the QFI equation used in step (f) of section 5.1.

It can be calculated using (5.13) that for the Hamiltonian 5.12,

$$QFI_\gamma = 4/(4\gamma^2 - 1)^2. \quad (5.14)$$

We can easily see that the QFI_γ diverges at $\gamma = 0.5$, which is the same value of the parameter γ , at which the EP is attained in the system, Fig. 5.2. As mentioned in the Introduction, this divergence is achieved generally at EPs [64, 148], despite some converse result [55]. We

emphasize that at the EP degeneracies, the perturbed eigenvalues and eigenvectors must be expanded in terms of Newton-Puiseux series [64] with fractional exponents of the perturbation strengths rather than Taylor series, to get the required divergence [see chapter 3].

We have performed simulation of the above system using “state_vector simulator” [156] and compared its results with the theoretical result of the QFI_γ of the system. We show in Fig. 5.2 how $\log(QFI_\gamma)$ varies with γ . It can be seen that the QFI_γ indeed diverges at the EP $\gamma = 0.5$.

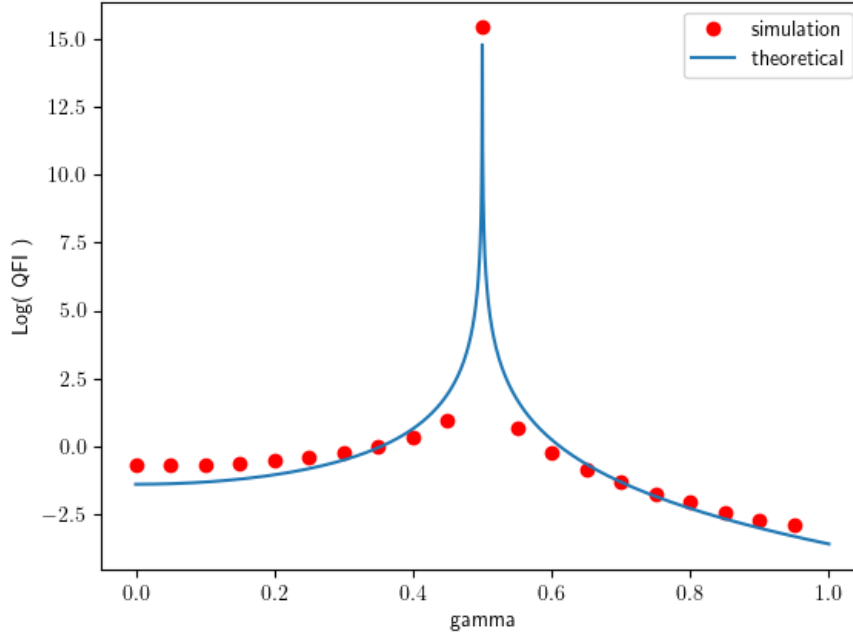


Figure 5.2: The variation of $\log(QFI_\gamma)$ with respect to γ for the Hamiltonian NH_1 (5.12). The QFI_γ diverges at the EP, which appears at $\gamma = 0.5$. Blue curve represents theoretical plot and red dots indicate simulation values at various γ values.

We next simulate the second Hamiltonian as in [55]:

$$NH_2 = \begin{pmatrix} \frac{1}{2}(\gamma - i\epsilon) & g \\ g & \frac{1}{2}(-\gamma + i\epsilon) \end{pmatrix}. \quad (5.15)$$

There exists an EP at $\gamma = 0$, when $g = |\epsilon|/2$. It can be seen that the QFI_γ diverges at $\gamma = 0$. The plot of $\log(QFI_\gamma)$ with respect to γ is given in Fig. 5.3. If we consider $\epsilon = 2$ and $g = 1$ and use the perturbation methods mentioned in [148] we find that $QFI_\gamma \approx \frac{1}{4\gamma^2}$. It diverges at $\gamma = 0$ which leads us to an EP of NH_2 .

The results for both the Hamiltonians (5.12) and (5.15) demonstrate the claim that the QFI_γ diverges at EPs.

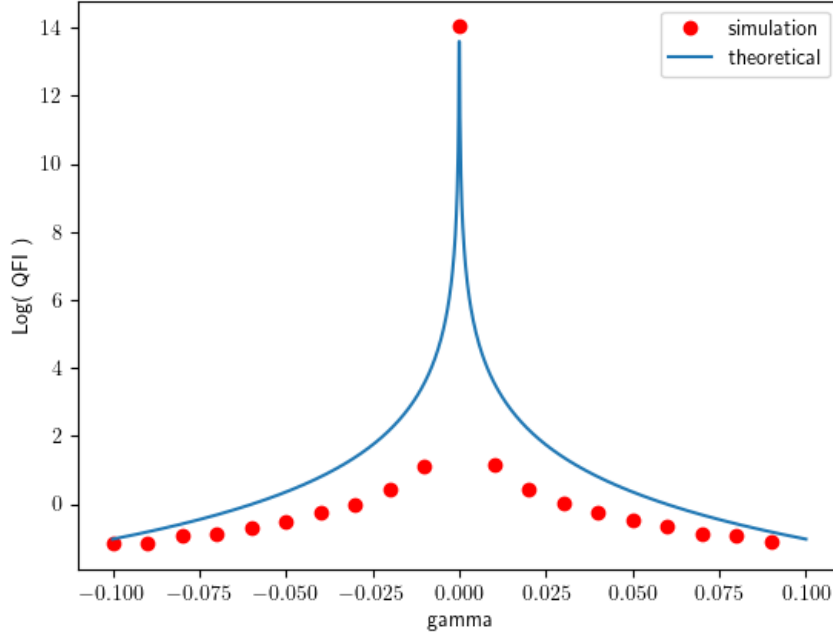


Figure 5.3: The variation of $\log(QFI)$ with respect to γ for the Hamiltonian NH_2 (5.15). The QFI diverges at the EP, which appears at $\gamma = 0$ when $g = |\epsilon|/2$. Blue curve represents theoretical plot and red dots indicate simulation values at various γ values.

5.3.2 Multiple EP

There are several articles which explore generation of multiple exceptional points [157, 158, 159]. Let us simulate a two-level system with multiple exceptional points. Consider the Hamiltonian

$$NH_3 = \begin{pmatrix} 1 & \sin(10\gamma\pi) \\ \cos(10\gamma\pi) & 1 \end{pmatrix}. \quad (5.16)$$

The eigenvalue of the system are $\lambda_{+,-} = \frac{1}{2}(2 \pm \sqrt{2\sin(20\pi\gamma)})$, the normalized eigenvectors of the system are $|\phi_{+,-}\rangle = \frac{1}{\sqrt{2}} \begin{pmatrix} \pm \frac{\sqrt{2}\sin(10\pi\gamma)}{\sqrt{\sin(20\pi\gamma)}} \\ 1 \end{pmatrix}$. The eigenvalues of NH_3^\dagger are complex conjugates and the normalized eigenvectors are $|\chi_{+,-}\rangle = \frac{1}{\sqrt{2}} \begin{pmatrix} \pm \frac{\sqrt{2}\cos(10\pi\gamma)}{\sqrt{\sin(20\pi\gamma)}} \\ 1 \end{pmatrix}$. The calculated QFI is thus

$$QFI_\gamma = \frac{200\pi^2}{\sin^2(20\pi\gamma)}. \quad (5.17)$$

The system is simulated and the QFI plotted in Figure 5.4. It can be seen that there are multiple EP points at $\gamma = a \times 0.05$ where $a \in I$.

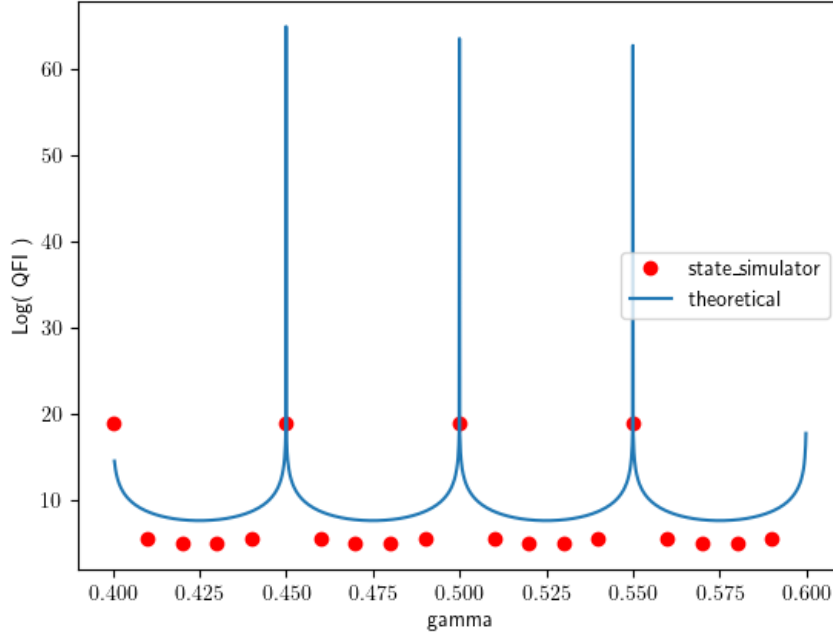


Figure 5.4: The variation of $\log(QFI)$ with respect to γ for the Hamiltonian NH_3 (5.16). The QFI diverges at the EP, which appears at $\gamma = 0.05a$, where the integer a varies from 8 to 12. Blue curve represents theoretical plot and red dots indicate simulation results or various values of γ .

5.4 Noise models on EP sensors

Even though the QFI diverges at EP, it still remains to be explored how noise affects the QFI . Let us consider various noise models and calculate the maximum QFI that can be attained for various parameters controlling the noise. In this Section, we will use the Hamiltonian 5.12.

Considering the amplitude damping noise that is parameterized with a decay probability b , a noiseless density matrix ρ transforms into the following matrix:

$$N_{AD}(\rho) = \begin{pmatrix} \rho_{00} + b\rho_{11} & \sqrt{1-b}\rho_{01} \\ \sqrt{1-b}\rho_{10} & (1-b)\rho_{11} \end{pmatrix}. \quad (5.18)$$

We show the variation of $\max[\log(QFI)]$ (i.e., the maximum of natural logarithm of QFI) with respect to the decay rate b at the EP $\gamma = 0.5$ for NH_1 (Fig. 5.5 (a)) and $\gamma = 0$ for NH_2 (Fig. 5.5 (b)). It can be observed that the $\max[\log(QFI)]$ remains significantly high for a wide range of b : $0 \leq b < 1$, except at $b = 1$, where the function suddenly drops to a negative value, i.e., where QFI becomes less than unity. Thus, $b = 1$ leads to a large upper bound of the error of parameter estimation [see Eq. (5.1)].

Next we consider the Pauli noise, which can be characterized by three types of errors, namely, the bit-flip, bit-phase-flip, and phase-flip errors, represented by the Pauli matrices

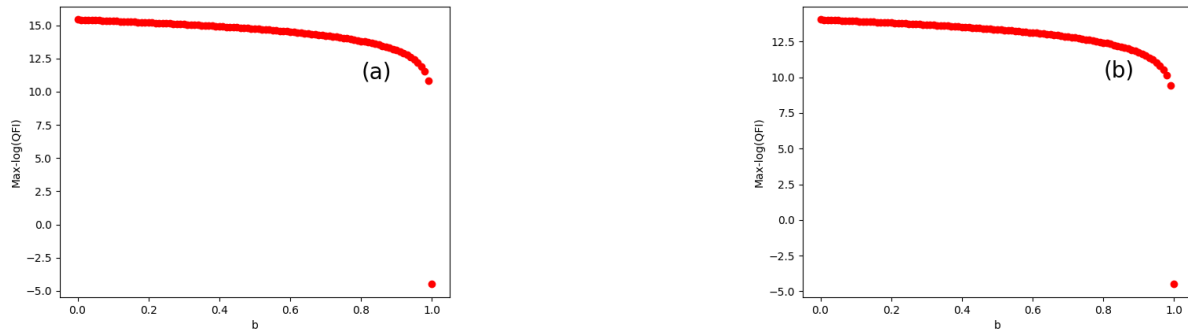


Figure 5.5: The variation of $\max[\log(QFI)]$ at EP with respect to the amplitude damping parameter b (a) for NH_1 and (b) for NH_2 .

X, Y, and Z, respectively. In presence of Pauli error, a noiseless density matrix ρ transforms into the following form:

$$N_{Pauli}(\rho) = (1 - p)\rho + p_1 X\rho X + p_2 Y\rho Y + p_3 Z\rho Z, \quad (5.19)$$

where p is the probability of no error, p_i ($i = 1, 2, 3$) is that of X, Y, and Z error, respectively, and the condition $\sum_{i=1}^3 p_i = p$ preserves the normalization of the density matrix.

We show in Fig. 5.6 how the $\max[\log(QFI)]$ varies with p , at the EP $\gamma = 0.5$ for NH_1 . We can clearly see from Fig. 5.6(a) that the bit-flip error affects the maximum achievable QFI to a large extent. The minimum value reached at $p = 0.5$ is 0. On the other hand, the Y and Z errors do not effect the QFI at all, as can be seen in Figs. 5.6(b) and (c). In the case of the equal probability $p/3$ of all three errors, however, the value of p is asymmetrically located at 0.75 in the range $[0,1]$, where the maximum value of the QFI becomes unity and its logarithm vanishes. For other values of p , in this case, the QFI can reach a much larger value leading to a far better EP-assisted sensing.

In Fig. 5.7, we show the variation of $\max[\log(QFI)]$ with p , at the EP $\gamma = 0$ for NH_2 . It is obvious from the Figs. 5.7(a) and (c) that the bit-flip and phase flip errors have a minimal effect on the maximum achievable QFI . Interestingly, unlike the case for NH_1 , the $\max[\log(QFI)]$ does not vanish for any p . In both these cases, the value of parameter p at which it reaches minima is 0.5, but in the case of NH_2 , it remains as high as 13.35. On the other hand, the Y error does not effect the QFI at all, as can be seen in Fig. 5.7(b). Therefore, our protocol stays robust against these errors. When all the three errors affect the system equally probably, the dependence of $\max[\log(QFI)]$ on p exhibits the similar behavior as in the case of NH_1 [see Fig. 5.7(d)].

Comparing Fig. 5.6 and 5.7 it can be deduced that in presence of noise with a parameter a , we need to choose the non-Hermitian system NH such that the $QFI_\gamma(a_0) \gg 0$, where a_0 is the value of the noise parameter at which the QFI reaches minima, and γ is the parameter to be estimated.

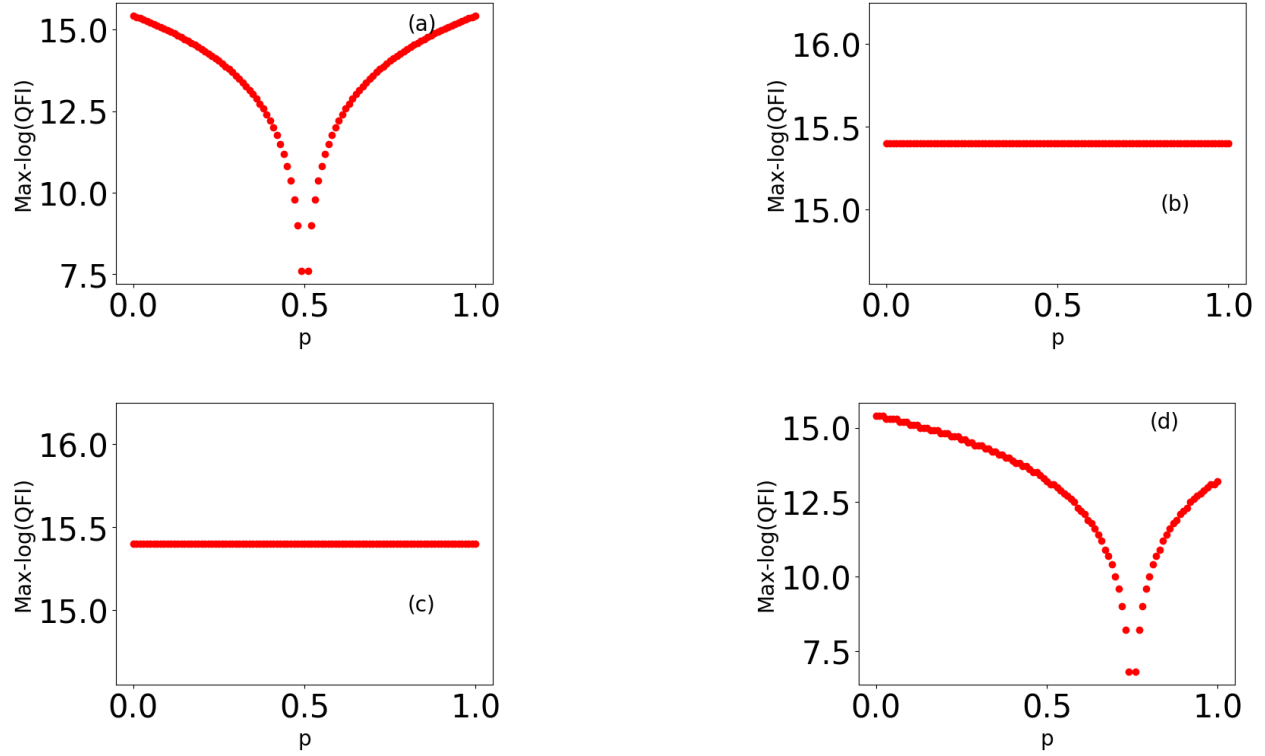


Figure 5.6: The variation of $\max[\log(QFI)]$ with respect to p for different Pauli errors for NH_1 . (a) Bit-Flip error: $p_1 = p, p_2 = 0, p_3 = 0$. (b) Bit-Phase-Flip error: $p_1 = 0, p_2 = p, p_3 = 0$. (c) Phase flip error: $p_1 = 0, p_2 = 0, p_3 = p$. (d) All errors with equal probability: $p_1 = p_2 = p_3 = p/3$.

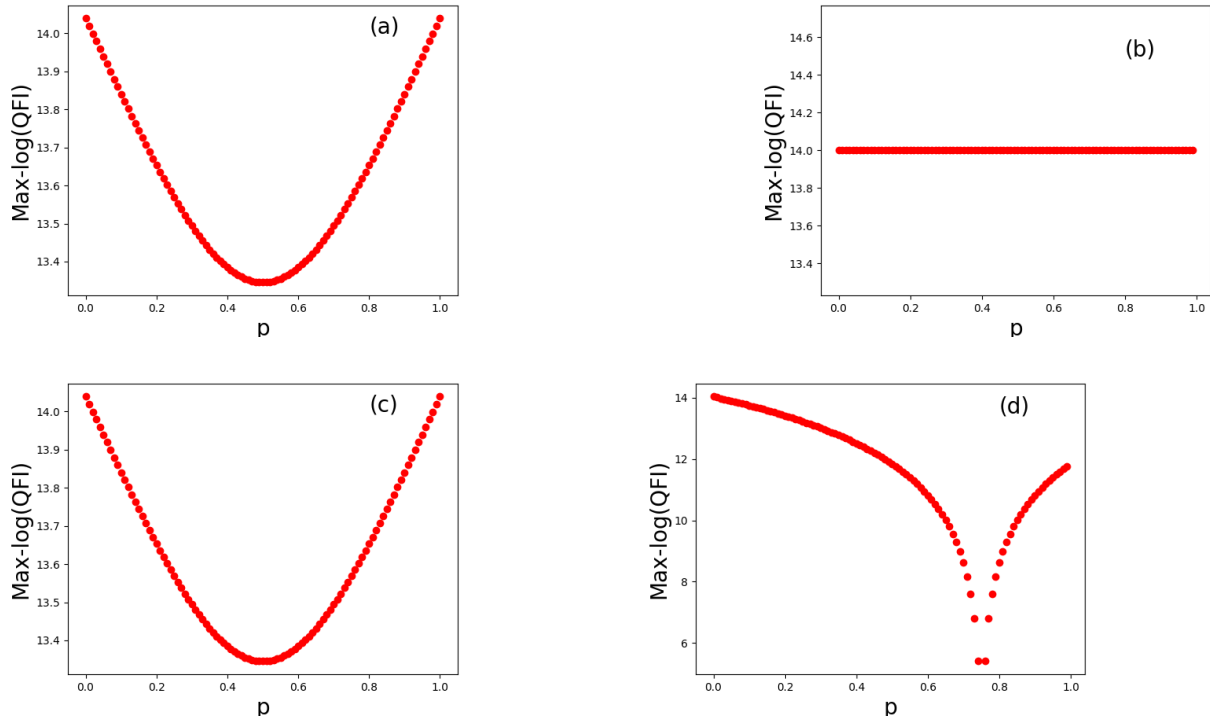


Figure 5.7: The variation of $\max[\log(QFI)]$ with respect to p for different Pauli errors for NH_2 . (a) Bit-Flip error: $p_1 = p, p_2 = 0, p_3 = 0$. (b) Bit-Phase-Flip error: $p_1 = 0, p_2 = p, p_3 = 0$. (c) Phase flip error: $p_1 = 0, p_2 = 0, p_3 = p$. (d) All errors with equal probability: $p_1 = p_2 = p_3 = p/3$.

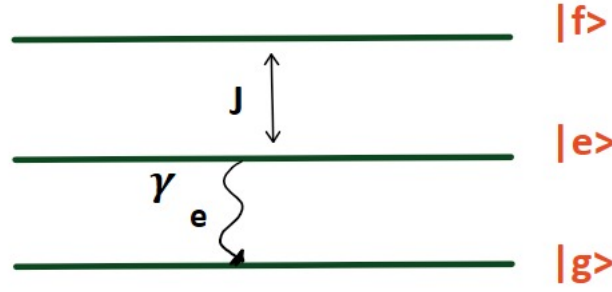


Figure 5.8: A three level system used to describe the relation between the non-unitary dynamics discussed in the thesis to the Lindbladian formalism. The effective hamiltonian of the two level sub-system (involving $|e\rangle$ and $|f\rangle$) is given by Eq.5.20. In the Lindblad formalism the evolution of the density state of the sub-system is given by Eq. 5.23.

5.5 Understanding the simulation from perspective of standard quantum formalisms

It is important to question how the description of these non-hermitian systems defined until now relate to standard formalism of Lindblad [160, 161] ? Are there some insights on the relation between these standard Lindblad formalisms to the work discussed in this thesis ? How is that, such non-unitary dynamics does not showcase mixing of the quantum states (i.e. loss of normalization) and why is a density matrix approach not a necessity in describing them ?

Let us understand this using a physical example as demonstrated in [43]. Consider a three level system with states $|g\rangle$, $|e\rangle$ and $|f\rangle$.

By focusing on the sub-system $|e\rangle, |f\rangle$ and the interaction of $|e\rangle$ with $|g\rangle$ as part of loss (Fig. 5.8). We propose that the effective hamiltonian (using heuristics) of this scenario is

$$H_{eff} = H_{bare} + H_{coupling} + H_{loss} = \Delta|e\rangle\langle e| + J(|e\rangle\langle f| + |f\rangle\langle e|) - i\frac{\gamma_e}{2}|e\rangle\langle e| \quad (5.20)$$

where H_{eff} is the effective non-unitary hamiltonian, γ_e is the occupation-number loss rate from state $|e\rangle$ to state $|g\rangle$, $\Delta = \omega_d - \omega_q$ (ω_d is driving frequency and ω_q is transition frequency between the states $|e\rangle$ and $|f\rangle$) is the detuning in the drive of the states $|e\rangle$ and $|f\rangle$ while J is the coupling strength between $|e\rangle$ and $|f\rangle$. Note, it is important to consider that the occupation-number loss rate from state $|f\rangle$ to $|e\rangle$ (γ_f) is such that $\gamma_e \gg \gamma_f$. This hamiltonian is non-unitary and has exceptional point at $\Delta = 0$ and $J = \gamma_e/4$.

Even after describing such an effective hamiltonian our description does not encompass the description of non-unitary evolution from one pure state to another as described by the quantum circuit in the general work on non-hermitian hamiltonians. When we evolve from one pure state to another the total population of system has to remain constant over time.

However, in our sub-system the population $P_e + P_f$ would not remain constant over time due to its interaction with the $|g\rangle$ (Infact $P_e + P_f + P_g$ will remain constant over time). However we can make the sum $P_e + P_f$ constant over time by adding an extra step of post-selection. Post-selection effectively normalizes the populations of the sub-system in consideration, s.t. $P_e^n + P_f^n$ always remains constant. Where

$$P_e^n = P_e / (P_e + P_f) \quad (5.21)$$

$$P_f^n = P_f / (P_e + P_f) \quad (5.22)$$

Using this extra step of post-selection we are able to transform from one pure state to another without mixing, even if the system is open as described above. We call this post-selection because in the post-selection process too, we keep the ancilla ($|g\rangle$) in a constant state by measuring it everytime and accepting the dynamics of the system only when it is in a particular state. This keeps the flow of probabilities (or population) out of the sub-system to ancilla at constant, in turn keeping the total populations in the subsystem constant. Compare this normalization of the population with the post-selection process in the quantum circuit in Sec. 5.5. In the circuit too, we effectively ignore the presence of ancilla by post-selection. Infact, such a wavefunction approach to such open quantum systems with post-selection has been described in [162, 163] (The post-selection process in the article is called as "gedanken measurement process" and the approach mentioned in the article is named as "Monte carlo wavefunction approach").

Now let us understand this from the perspective of Lindblad formalism. The time evolution of density matrix ($\rho_S(t)$) of the reduced 2 level system can be written as

$$\dot{\rho}_S(t) = -\frac{i}{\hbar}[H_c, \rho_S] + \sum_i \gamma_i \left(L_i \rho_S L_i^\dagger - \frac{1}{2} \{ L_i^\dagger L_i, \rho_S \} \right) = \mathcal{L} \rho_S(t) \quad (5.23)$$

where the total hamiltonian of the 3-level system is $H_T = H_S \otimes I_E + I_S \otimes H_E + \alpha H_I$. H_S denotes the density matrix of the 2 level system. Here $H_c = H_S + H_{LS}$ where H_{LS} is called as Lamb shift hamiltonian. Upon calculation with above considerations $H_c = J(|e\rangle\langle f| + |f\rangle\langle e|) - \frac{\Delta}{2}(|f\rangle\langle f| - |e\rangle\langle e|)$. Note that H_c is hermitian and called as free hamiltonian. The Lindblad dissipation operators are $L_e = \sqrt{\gamma_e}|g\rangle\langle e|$ and $L_f = \sqrt{\gamma_f}|e\rangle\langle f|$ accounting for energy decay from level $|e\rangle$ to $|g\rangle$ and from $|f\rangle$ to $|e\rangle$. This gives us

$$\dot{\rho}_{ff} = -iJ(\rho_{ef} - \rho_{fe}) - \gamma_f \rho_{ff} \quad (5.24)$$

$$\dot{\rho}_{ee} = iJ(\rho_{ef} - \rho_{fe}) - \gamma_e \rho_{ee} + \gamma_f \rho_{ff} \quad (5.25)$$

$$\dot{\rho}_{ef} = -iJ(\rho_{ff} - \rho_{ee}) - (\gamma_e + \gamma_f + 2i\Delta)/2 \rho_{ef} \quad (5.26)$$

$$\dot{\rho}_{fe} = iJ(\rho_{ff} - \rho_{ee}) - (\gamma_e + \gamma_f - 2i\Delta)/2 \rho_{fe} \quad (5.27)$$

$$(5.28)$$

Considering the system initialized in state $|f\rangle$ and in the limit of $\gamma_f \ll \gamma_e$ and considering $\Delta = 0$, the populations in levels e and f can be found by diagonalization are

$$P_e = \rho_{ee} = e^{-\gamma_e t/2} (J/\alpha)^2 \sin^2(\alpha t) \quad (5.29)$$

$$P_f = \rho_{ff} = e^{-\gamma_e t/2} (J/\alpha)^2 \cos^2(\alpha t - \theta) \quad (5.30)$$

where $\alpha = \sqrt{J^2 - (\gamma_e/4)^2}$ and $\theta = \arcsin(\gamma_e/4J)$. It can be checked that the sum of these is not equal to constant, i.e. the population is not normalized or dependent on the sub-system parameters and this description would lead to mixing of states. This is because the decay term from the reduced two-level system (γ_e) is not equal to zero. if it is zero than $\theta = 0$ as well as $e^{-\gamma_e t/2} = 1$. In that case $P_e + P_f = (J/\alpha)^2$. However, we can normalize these populations (even in the presence of the dissipation) by considering the equations Eq. 5.22 such that the total population of sub-system remains constant over time. This is equivalent to having a transformation from one pure state to another even when the system is non-unitary, without invoking the density matrix formalism and mixing of states. Such a normalization is nothing but equivalent to post-selection process as discussed in [43]. The population upon normalization is

$$P_e^n = \frac{P_e}{P_f + P_e} = \frac{\sin^2(\alpha t)}{\sin^2(\alpha t) + \cos^2(\alpha t - \theta)} \quad (5.31)$$

$$P_f^n = \frac{P_f}{P_f + P_e} = \frac{\cos^2(\alpha t - \theta)}{\sin^2(\alpha t) + \cos^2(\alpha t - \theta)} \quad (5.32)$$

These populations are found to be same as the populations found in the description of the subsystem using H_{eff} (Eq. 5.20) in [43]. Hence, this example gives an idea on connection between Lindbladian approach and the approach used in the research involved on non-unitary evolutions. The standard Lindbladian approach cannot explain these process involving post-selection. A Hybrid Louivillian formalism incorporating the post-selection process has been proposed recently [164] to incorporate the methods used by [43].

[43] mentions that post-selection is the only method known to achieve such non-unitary (and exceptional point) dynamics preserving the purity in quantum systems, but a general proof is lacking to legitimize this fact. In fact in later work by [165], a method is shown which circumvents the post-selection. However, this discussion is beyond the scope of this thesis, but is worthwhile exploring in future works using quantum circuits.

5.6 Limitations of ancilla-based method for quantum sensing

Let us now discuss the limitations in the ancilla-based method for EP sensing. In the following, we will also propose how one can ameliorate them.

First, we should mention the necessity to normalize the non-unitary operator to implement it on a quantum computer. As discussed in step (b) in section 5.1, the normalized non-unitary time evolution operator $NUTE_N$ is related to the original time evolution operator $NUTE$ as:

$$NUTE_N = \frac{1}{\max(\Sigma)} NUTE, \quad (5.33)$$

where $\max(\Sigma)$ is the maximum of the singular value of the matrix. This means the actual transformation is:

$$NUTE_N|\xi\rangle = |\phi''\rangle = \frac{1}{\max(\Sigma)}|\phi\rangle \xrightarrow{Norm} \frac{1}{\mathcal{N}}|\phi\rangle, \quad (5.34)$$

where $\frac{1}{\mathcal{N}}|\phi\rangle$ is the required state from the original non-unitary time evolution.

Second, the post-selection puts a resource overhead on the simulation of the system being studied. The probability of success of finding the ancilla to be in $|0\rangle$ state is uncontrollable, as it can be seen from the previous Section. For every unsuccessful attempt, the depth of the circuit is increased by a factor of 3. There are various methods to reduce the resource overhead, e.g., ancilla thermalization [166]. There are some proposals where non-unitary evolutions can be performed using dissipation engineering and without post-selection [167, 168]. However we believe that due to conservation of probability, post-selection cannot be avoided. A study of link between weak measurements and sensing at EPs of the non-Hermitian systems is promising [169, 170, 171, 172].

Third, note that these methods only apply to second-order exceptional point systems. For higher-dimensional systems including qutrits and qudits, the circuits need to be modified. Higher order EPs have been shown to have higher sensitivity and being more robust [42].

5.7 Conclusion

In this chapter, our focus was on simulating non-unitary dynamics on gate-based quantum computers, which typically operate using unitary dynamics. We began by exploring various gate-based quantum computing platforms that serve as the foundation for our simulations.

Next, we delved into simulating the dynamics of EP sensors. Initially, we examined systems with a single EP and then expanded our exploration to systems with multiple EPs. By studying these dynamics, we aimed to gain a deeper understanding of the behavior and properties of EPs in quantum systems.

To make our simulations more realistic, we introduced noise models into these systems. We investigated the effects of noise on the quantum Fisher information (QFI), which is a crucial metric for quantifying the performance of EP sensors. This analysis provided insights into how noise influences the accuracy and precision of EP sensor measurements.

Lastly, we discussed the limitations of the method used to generate non-unitary dynamics on gate-based quantum computers. We addressed the challenges and constraints associated with simulating non-unitary processes on platforms designed primarily for unitary computations. Understanding these limitations is essential for further advancing the field and developing more robust and efficient techniques for simulating non-unitary dynamics.

It will be interesting to compare the resources it would take to simulate the exceptional point quantum system using Quantum Monte Carlo techniques. Quantum Monte Carlo techniques use classical randomness to simulate quantum systems. There are few articles which employ these techniques to simulate exceptional point systems, however the simulations cannot be called as truly quantum as they do not employ quantum systems [173, 174]. However, such simulations are only useful as it is not feasible to use actual quantum systems for simulations. However, with the advent of cloud quantum computing the process of using

quantum systems for quantum simulations has become very easy. In fact our work is one of the few research articles which exploit the access to quantum systems through cloud.

Throughout this chapter, we gained valuable knowledge about simulating non-unitary dynamics on gate-based quantum computers, explored the behavior of EP sensors, investigated the impact of noise, and reflected on the limitations of the simulation method. This knowledge serves as a foundation for future research and development in the field of quantum simulations and non-unitary dynamics.

Chapter 6

Future Work and Conclusion

6.1 Future Work

6.1.1 Optomechanical Isolators

Let us explore a few avenues of research and problems in the field of developing optomechanical isolators.

Enhanced performance of optomechanical isolators is one avenue which needs to be explored. Researchers are continually working towards improving the performance of optomechanical isolators. This includes achieving higher isolation ratios, broader operating bandwidths, lower insertion losses, and reduced power consumption. Future developments may lead to optomechanical isolators with enhanced performance characteristics, making them more versatile and suitable for a wider range of applications.

Integration with other technologies is of utmost importance. Optomechanical isolators can be integrated with other photonic components and systems to create more advanced functionalities. For example, combining optomechanical isolators with photonic integrated circuits (PICs) can enable on-chip isolation and protection. Integration with other technologies like MEMS (Micro-Electro-Mechanical Systems) and nanophotonics may also open up new possibilities for optomechanical isolators.

Applications of OM isolators can also be explored. Optomechanical isolators may find applications in emerging fields such as quantum information processing and quantum communication. These areas require precise control over the transmission and isolation of individual photons. Optomechanical isolators could play a role in enabling efficient and reliable quantum information transfer.

6.1.2 Non-Hermitian quantum sensors

For the case of Non-Hermitian quantum sensors there are various problems which need to be addressed.

Non-Hermitian systems are also plagued with noise. By carefully engineering the non-Hermitian properties of a system, it may be possible to mitigate the effects of decoherence and environmental noise. Future directions could involve developing novel techniques to actively control and utilize the non-Hermitian features for noise reduction in quantum sensors.

Non-Hermitian quantum sensing techniques can potentially be applied to imaging and spectroscopy tasks. By exploiting the unique properties of non-Hermitian systems, it may be possible to achieve higher-resolution imaging or more precise spectroscopic measurements. Future directions may involve the development of non-Hermitian quantum sensors tailored specifically for imaging and spectroscopy applications. Hence, Quantum imaging and spectroscopy is another avenue to explore.

We had explored non-unitary quantum circuits in the thesis. There are some potential benefits of using such circuits for certain applications like creating Quantum neural networks (QNN) and also in the context of Abrams-Llyods concept of non-linear quantum computing. It will be worthwhile exploring these ideas. Exploring such non-unitary sensors may also lead to our understanding of non-unitary quantum gates.

The field has many avenues unexplored and it is worth exploring.

6.2 Conclusion of thesis

In Chapter 1 we discussed the mathematical preliminaries and the foundations required for understanding the thesis. Namely, we first discuss the Hermitian operators and their properties. Then it is contrasted with properties of Non-Hermitian diagonalizable and non-diagonalizable (defective) operators. Finally, we also made the case for exploring defective operators in physics which have still being largely ignored.

Chapter 2 explores what is non-reciprocity. Non-reciprocal systems allow light to flow in different directions, differently. Special cases of non-reciprocal systems are called as isolators, which allow light to flow in only one direction and not another. We first discuss the conventional method to achieve isolation, and then limitations in achieving them. We review various other methods to sort out these limitations, namely, optomechanical isolation. We also explore the issues plaguing these isolators.

Chapter 3 discusses the Non-Hermitian quantum sensors. Namely, the exceptional point quantum sensors. We first derive the eigenvalue sensitivity of a system at EP due to perturbation and contrast it with Hermitian degeneracy case. However, such a metric of performance cannot be used to know if a sensor is efficient. We discuss another metric known as Quantum Fisher Information (QFI) and discuss its relation to variance of estimation through Quantum Cramer Rao Bound (QCRB). Finally we lay down the various experimental demonstrations of exceptional points found in literature.

In Chapter 4 we present our work on tunable optomechanical isolators. Optomechanical isolators are limited by bandwidth of operation. Theory shows that the frequency at which isolation occurs is decided by the natural frequency of the mechanical isolator of the membrane in the optomechanical isolator. However this is fixed during fabrication and cannot be changed. We showcase that using quadratic optomechanical coupling and mechanical drive we can achieve tunability of isolation frequency. We finally discuss experimental proposals for realization of such a tunable isolation frequency optomechanical isolator.

Chapter 5 presents our work on simulation of exceptional point sensors on quantum computers. Most of the demonstrations of exceptional point sensors have been in classical optical regime. There are very few demonstrations of such systems in quantum regime. This also restricts us from exploiting various phenomenon like entanglement with exceptional point sensors. Our work enables us to realise these systems using non-unitary circuit model using ancilla and post-selection on cloud-based quantum computers like IBM Q Experience. We explore the effects on QFI around EP and showcase the divergence at EP. This is because the EPs are algebraic singularities in parameter space and lead to expansion of eigenvalues and eigenvectors in Puiseux series rather than Taylor series. We also explore the effects of noise at EPs. We also explore the systems with multiple EPs. We finally discuss the limitations of the methods discussed.

Chapter 7

Appendix

7.1 Code sample for simulating an exceptional point on IBM Q Experience Quantum Lab

Let us include the code samples for simulating exceptional point sensors and calculating QFI on IBM Q Experience. First we include the important libraries for proper functioning of the code.

```
1 import numpy as np
2
3 # Importing standard Qiskit libraries
4 from qiskit import QuantumCircuit, transpile, Aer, IBMQ, execute,
   QuantumRegister, ClassicalRegister
5 from qiskit.tools.jupyter import *
6 from qiskit.visualization import *
7 from ibm_quantum_widgets import *
8 from qiskit.providers.aer import QasmSimulator
9 from qiskit.extensions import UnitaryGate
10 from math import pow, pi, cos, sin
11 from cmath import exp, sqrt
12 from scipy import linalg
13 from scipy.linalg import svd, eig, norm
14 from numpy import array, polyfit, gradient, diff, abs
15 from cmath import sqrt
16 from qiskit.quantum_info import state_fidelity
17 import matplotlib.pyplot as plt
18
19 # Loading your IBM Quantum account(s)
20 provider = IBMQ.load_account()
```

Listing 7.1: Import required libraries

Next we define the parameter range and other important values

```
1 p=10 #number of points
2 bound1=0.3
3 bound2=0.7 #Bound around which the QFI needs to be sampled
4 nsteps=(bound2-bound1)/p #Number of steps between the bound
5 epsarr=[] #define the parameter array we use eps and gamma interchangeably
```

```

6 deps=0.0000001 #Amount of perturbation given equal to \delta \gamma in the
  thesis
7 print('Program has started')

```

Listing 7.2: Define values

We then define the Hamiltonian and create the gates required for the non-unitary circuit. The Hamiltonian used is as defined in Equation 5.12.

```

1 def gates(eps,j):
2     H=np.matrix([[0,0.5+eps],[0.5-eps,0]]) #Hamiltonian as discussed in
  thesis
3     if j==0:
4         H=H # Find H
5     #Find the time evolution matrix
6     timeev = np.matrix(linalg.expm(-1j*H))
7     #Normalize the time evolution by highest singular value
8     #Singular value decomposition
9     U, s, VT = np.linalg.svd(timeev)
10    Norm=1/s.max() #Frobenius normalizing tiem evolution matrix
11    Normtimeev=np.matrix(Norm*timeev)
12    U,s,VT=np.linalg.svd(Normtimeev)
13    I=np.matrix([[1,0],[0,1]])
14    UxI=np.kron(U, I)
15    VTxI=np.kron(VT,I)
16    #Define the unitary gates for U and V+ in Fig. 5.1 in thesis
17    UxI = UnitaryGate(UxI, label='U')
18    VTxI=UnitaryGate(VTxI, label='VT')
19    return UxI,s,VTxI,H;

```

Listing 7.3: Define hamiltonian and gates

Now we execute and find the fidelity between unperturbed and perturbed state around EP.

```

1 Fidarr=[] #Define Fidelity array
2 initialstatevectorNH=[] #Define array to enter initial state vector to the
  non-unitary circuit
3 cr=ClassicalRegister(2)
4 qr=QuantumRegister(2)
5 qc=QuantumCircuit(qr,cr)
6 for i in range(p):
7     eps=bound1+nsteps*i #Slowly increase the parameter at which QFI is to
  be evaluated
8     for j in range(2):
9         # Evaluate fidelity exactly at eps
10        if j==0:
11            U,s,VT, H=gates(eps,j)
12            #v1 is the set of eigenvalues and v2 is set of eigenvectors
13            v1,v2 = eig(H)
14            initialstatevectorNH=v2[:, 0]/norm(v2[:, 0])
15            qc.initialize([initialstatevectorNH[0],0,initialstatevectorNH
  [1],0])
16            #Create the C\Sigma gate as defined in Fig. 5.1 in thesis
17            Cs=array([[1,0,0,0],[0,-1,0,0],[0,0,s[1],sqrt(1-pow(s[1],2))
  ],[0,0,sqrt(1-pow(s[1],2)),-s[1]]])

```

```

18         Cs=UnitaryGate(Cs, label='Cs')
19         qc.append(VT,[0,1])
20         qc.append(Cs,[0,1])
21         qc.append(U,[0,1])
22         #Procedure for post-selection
23         qc.measure(0,0)
24         counts={'01': 1}
25         while counts == {'01': 1}:#Repeat until success
26     # choose the statevector simulator
27         simulator = Aer.get_backend('statevector_simulator')
28     # get the statevector
29         result = execute(qc, simulator).result()
30         statevector1 = result.get_statevector()
31         counts = result.get_counts(qc)
32     if j==1:
33         # Evaluate fidelity slightly perturbed from eps by deps
34     defined above
35         U,s,VT, H =gates(eps+deps,j)
36         #v3 is the set of eigenvalues and v4 is set of eigenvectors
37         v3,v4 = eig(H)
38         initialstatevectorNH2=v4[:, 0]/norm(v4[:, 0]) #Note the state
39     has changed to 0 instead of 1 in the AnotherEP case
40         qc.initialize([initialstatevectorNH2[0],0,
41     initialstatevectorNH2[1],0])
42         #Create the C\Sigma gate as defined in Fig. 5.1 in thesis
43         Cs=array([[1,0,0,0],[0,-1,0,0],[0,0,s[1],sqrt(1-pow(s[1],2))
44     ],[0,0,sqrt(1-pow(s[1],2)),-s[1]])
45         Cs=UnitaryGate(Cs, label='Cs')
46         qc.append(VT,[0,1])
47         qc.append(Cs,[0,1])
48         qc.append(U,[0,1])
49         #Procedure for post-selection
50         qc.measure(0,0)
51         counts={'01': 1}
52         while counts == {'01': 1}:#Repeat until success
53     # choose the statevector simulator
54         simulator = Aer.get_backend('statevector_simulator')
55     # get the statevector
56         result = execute(qc, simulator).result()
57         statevector2 = result.get_statevector()
58         counts = result.get_counts(qc)
59     Fid=state_fidelity(statevector2,statevector1) #Note this is the usual
60     fidelity of the Hermitian case compared to the Another EP, all the crux
61     lies in making statevector(1) to (0) for intialstatevector2.
62     epsarr.append(eps)
63     Fidarr.append(Fid)

```

Listing 7.4: Execute and find fidelity

Now we calculate Bures distance using the Fidelity values obtained from above experiment

```

1 #Calculate Bures distance
2 Fidarrrtwo=[]
3 Bd22=[]
4 Fidarrrtwo = [i * 2 for i in Fidarr]

```

```
5 Bd22 = [2 - i for i in Fidarrtwo]
```

Listing 7.5: Calculate Bures distance from Fidelity values

Now we calculate QFI using the Bures distance obtained from above code

```
1 #Quantum Fisher information
2 QFI=[]
3 QFI = [i * (1/(2*deps)**2) for i in Bd22]
```

Listing 7.6: Calculate QFI

Now the QFI is plotted with respect to the parameter to be estimated i.e. γ . Refer to chapter 5 for more information on theory. We then also calculate the theoretical value and plot them together.

```
1 #Theoretical QFI
2 plt.rcParams['text.usetex'] = True
3 x = np.linspace(0.4,0.6,3500)
4 y = 1/(8*(4*x**2-1)**2)
5
6 #Numerical QFI
7 plt.figure(facecolor='white')
8
9 fig2 = plt.plot(epsarr, np.log(QFI), 'o', color='r')
10 fig3 = plt.plot(x,np.log(y))
11
12 #naming x axis
13 plt.xlabel('gamma')
14 # naming the y axis
15 plt.ylabel('Log( QFI )')
16
17 #Plot legends
18 plt.legend(['state_simulator','theoretical'])
19 #NOTE THE DIVERGENCE IS VERY SENSITIVE SO CHOOSE x range etc above
   properly
20 # giving a title to my graph
21 plt.title('EP-Sensor')
22
23 # function to show the plot
24 plt.show()
```

Listing 7.7: Plot theoretical and experimentally obtained QFI

The plot obtained is as in Figure 5.2.

7.2 Code sample for understanding impact of noise on QFI at exceptional points on IBM Q Experience Quantum Lab

Let us discuss the code to add Amplitude damping noise (Equation 5.18) on EP sensor simulation. The system is same as considered in Equation 5.12.

We evaluate the QFI at EP. We have seen that in Figure 5.2 and Figure 5.3, QFI is maximum; hence we denote it by $\max[\log(QFI)]$. This $\max[\log(QFI)]$ is plotted with respect to the amplitude damping noise parameter b by the code.

```

1 import numpy as np
2
3 # Importing standard Qiskit libraries
4 from qiskit import QuantumCircuit, transpile, Aer, IBMQ, execute,
   QuantumRegister, ClassicalRegister
5 from qiskit.tools.jupyter import *
6 from qiskit.visualization import *
7 from ibm_quantum_widgets import *
8 from qiskit.providers.aer import QasmSimulator
9 from qiskit.extensions import UnitaryGate
10 from math import pow, pi, cos, sin
11 from cmath import exp, sqrt
12 from scipy import linalg
13 from scipy.linalg import svd, eig, norm
14 from numpy import array, polyfit, gradient, diff, abs
15 from cmath import sqrt
16 from qiskit.quantum_info import state_fidelity, DensityMatrix,
   partial_trace
17 import matplotlib.pyplot as plt
18
19 # Loading your IBM Quantum account(s)
20 provider = IBMQ.load_account()

```

Listing 7.8: Import required libraries

Now we write code to define gate for Hamiltonian (Equation 5.12) at EP.

```

1 #Hamiltonian at EP
2 H1=np.matrix([[0,0.5+eps],[0.5-eps,0]])
3 print(H1)
4 #Find the time evolution
5 timeev1 = np.matrix(linalg.expm(-1j*H1))
6 #Normalize the time evolution by highest singular value
7 #Singular value decomposition
8 U1, s1, VT1 = np.linalg.svd(timeev1)
9 Norm1=1/s1.max() #Frobenius normalizing tiem evolution matrix
10 Normtimeev1=np.matrix(Norm1*timeev1)
11 U1,s1,VT1=np.linalg.svd(Normtimeev1)
12 #Define the unitary gates for U and V+ in Fig. 5.1 in thesis
13 I=np.matrix([[1,0],[0,1]])
14 UxI1=np.kron(U1, I)
15 VTxI1=np.kron(VT1,I)
16 UxI1 = UnitaryGate(UxI1, label='U')
17 VTxI1=UnitaryGate(VTxI1, label='VT')
18 #Create the C\Sigma gate as defined in Fig. 5.1 in thesis
19 Cs1=array([[1,0,0,0],[0,1,0,0],[0,0,s1[1],sqrt(1-pow(s1[1],2))],[0,0,sqrt
   (1-pow(s1[1],2)),-s1[1]]])
20 Cs1=UnitaryGate(Cs1, label='Cs1')

```

Listing 7.9: Code to define gates at EP of the hamiltonian

Now we write code to define gate for hamiltonian (Equation 5.12) slightly perturbed from EP.

```

1 #Hamiltonian slightly perturbed from EP
2 H2=np.matrix([[0,0.5+(eps+deps)],[0.5-(eps+deps),0]])
3 print(H2)
4     #Find the time evolution
5 timeev2 = np.matrix(linalg.expm(-1j*H2))
6 #     print("timeev = ", timeev)
7     #Normalize the time evolution by highest singular value
8     #Singular value decomposition
9 U2, s2, VT2 = np.linalg.svd(timeev2)
10 Norm2=1/s2.max() #Check eq(46) of "Non-Normal Hamiltonian dynamics...."
    Nakagawa
11 Normtimeev2=np.matrix(Norm2*timeev2)
12 #     print("NormTimeev = ", Normtimeev)
13 U2,s2,VT2=np.linalg.svd(Normtimeev2) #Here Vt is v dagger itself unlike in
    Mathematica, note the mathematica and this will not match as U and V
    are not unique
14     #print("s = ",s)
15     #print("U = ", U)
16     #print("VT = ",VT)
17 I=np.matrix([[1,0],[0,1]])
18 UxI2=np.kron(U2, I)
19 VTxI2=np.kron(VT2,I)
20 UxI2 = UnitaryGate(UxI2, label='U')
21 VTxI2=UnitaryGate(VTxI2, label='VT')
22 Cs2=array([[1,0,0,0],[0,1,0,0],[0,0,s2[1],sqrt(1-pow(s2[1],2))],[0,0,sqrt
    (1-pow(s2[1],2)),-s2[1]]])
23 Cs2=UnitaryGate(Cs2, label='Cs2')

```

Listing 7.10: Code to define gates at a value slightly perturbed from EP of the hamiltonian

Now we create a circuit for the first case discussed above, i.e. Hamiltonian at EP.

```

1 # Create circuit for system at EP
2 qc=QuantumCircuit(2,2)
3 v1,v2 = eig(H1)
4 initialstatevectorNH1=v2[:, 0]/norm(v2[:, 0])
5 qc.initialize([initialstatevectorNH1[0],0,initialstatevectorNH1[1],0])
6 qc.append(VTxI1,[0,1])
7 qc.append(Cs1,[0,1])
8 qc.append(UxI1,[0,1])
9 qc.measure(0,0)
10 counts={'01': 1}
11 while counts == {'01': 1}:#Repeat until success
12     # choose the statevector simulator
13     simulator = Aer.get_backend('statevector_simulator')
14     # get the statevector
15     result = execute(qc, simulator).result()
16     statevector1 = result.get_statevector()
17     counts = result.get_counts(qc)
18 #     print(counts)
19 if counts == {'00': 1}:
20     print(statevector1)

```

Listing 7.11: Code to create circuit at EP of the hamiltonian

Now we create a circuit for the second case discussed above, i.e. Hamiltonian at value slightly perturbed from EP.

```

1 # Create circuit for system at slightly perturbed from EP
2 qc2=QuantumCircuit(2,2)
3 w1,w2 = eig(H2)
4 initialstatevectorNH2=w2[:, 0]/norm(w2[:, 0])
5 qc2.initialize([initialstatevectorNH2[0],0,initialstatevectorNH2[1],0])
6 qc2.append(VTxI2,[0,1])
7 qc2.append(Cs2,[0,1])
8 qc2.append(UxI2,[0,1])
9 qc2.measure(0,0)
10 counts2={'01': 1}
11 while counts2 == {'01': 1}:#Repeat until success
12     # choose the statevector simulator
13     simulator2 = Aer.get_backend('statevector_simulator')
14     # get the statevector
15     result2 = execute(qc2, simulator2).result()
16     statevector2 = result2.get_statevector()
17     counts2 = result2.get_counts(qc2)
18 #     print(counts)
19     if counts2 == {'00': 1}:
20         print(statevector2)

```

Listing 7.12: Code to create circuit at value slightly perturbed from EP of the Hamiltonian

We obtain the density matrices, then calculate the $\max[\log(QFI)]$ after adding noise through Equation 5.18 with noise parameter b .

```

1 #Obtain density matrix of the system at EP
2 Dm1=np.matrix(partial_trace(DensityMatrix(statevector1),[0]))
3 print(Dm1)
4
5 #Obtain density matrix of the system slightly perturbed from EP
6 Dm2=np.matrix(partial_trace(DensityMatrix(statevector2),[0]))
7 print(Dm2)
8
9 #Adding Noise and embedding it in QFI
10 QFIarr=[]
11 gammaarr=[]
12 for i in range(101):
13     gamma=0.01*i #Decay probability
14     NDm1=np.matrix([[Dm1[0,0]+gamma*Dm1[1,1],sqrt(1-gamma)*Dm1[0,1]],
15                     [(1-gamma)*Dm1[1,0],(1-gamma)*Dm1[1,1]])
16     NDm2=np.matrix([[Dm2[0,0]+gamma*Dm2[1,1],sqrt(1-gamma)*Dm2[0,1]],
17                     [(1-gamma)*Dm2[1,0],(1-gamma)*Dm2[1,1]])
18     Fid=state_fidelity(NDm1,NDm2)
19     Bd=2-2*np.sqrt(Fid)
20     QFI=Bd/(2*deps**2)
21     print(QFI)
22     QFIarr.append(QFI)
23     gammaarr.append(gamma)

```

Listing 7.13: Obtaining $\max[\log(QFI)]$

Finally plot the $\max[\log(QFI)]$ v/s the amplitude noise parameter b

```
1 #Plot the MAX[QFI] i.e. QFI at EP for various values of noise plotted on x
  -axis
2 plt.figure(facecolor='white')
3
4 fig2 = plt.plot(gammaarr, np.log(QFIarr), 'o', color='red')
5
6
7 # naming the x axis
8 plt.xlabel('b')
9 # naming the y axis
10 plt.ylabel('Max-log(QFI)')
11
12 plt.text(0.8, 10, '(a)', fontsize = 20)
13 plt.savefig('AD')
14
15 # function to show the plot
16 plt.show()
```

Listing 7.14: Plot the result

The plot is as obtained in Figure 5.5.

Bibliography

- [1] X-W. Xu and Y. Li. Optical nonreciprocity and optomechanical circulator in three-mode optomechanical systems. *Physical Review A*, 91:053854, 2015.
- [2] Serge Lang. *Introduction to linear algebra*. Springer Science & Business Media, 2012.
- [3] Sheldon Axler. *Linear algebra done right*. Springer Science & Business Media, 1997.
- [4] Robert R Stoll. *Linear algebra and matrix theory*. Courier Corporation, 2013.
- [5] WD Heiss. Exceptional points of non-hermitian operators. *Journal of Physics A: Mathematical and General*, 37(6):2455, 2004.
- [6] WD Heiss. The physics of exceptional points. *Journal of Physics A: Mathematical and Theoretical*, 45(44):444016, 2012.
- [7] Michael V Berry. Physics of nonhermitian degeneracies. *Czechoslovak journal of physics*, 54(10):1039–1047, 2004.
- [8] Richard Bronson (Auth.). *Matrix Methods. An Introduction*. Elsevier Inc, Academic Press Inc, 1969.
- [9] Sheldon Axler. *Linear Algebra Done Right*. Undergraduate texts in mathematics. Springer, 2nd ed edition, 1997.
- [10] Steve Bellenot. Applied linear algebra ii. <https://www.math.fsu.edu/~bellenot/class/s06/1a2/>, April 2013.
- [11] Nimrod Moiseyev. *Non-Hermitian quantum mechanics*. Cambridge University Press, 2011.
- [12] Ali Mostafazadeh. Pseudo-hermitian representation of quantum mechanics. *International Journal of Geometric Methods in Modern Physics*, 7(07):1191–1306, 2010.
- [13] Yuto Ashida, Zongping Gong, and Masahito Ueda. Non-hermitian physics. *Advances in Physics*, 69(3):249–435, 2020.
- [14] Carl M Bender. Making sense of non-hermitian hamiltonians. *Reports on Progress in Physics*, 70(6):947, 2007.

- [15] Dirk Jalas, Alexander Petrov, Manfred Eich, Wolfgang Freude, Shanhui Fan, Zongfu Yu, Roel Baets, Miloš Popović, Andrea Melloni, John D Joannopoulos, et al. What is—and what is not—an optical isolator. *Nature Photonics*, 7(8):579–582, 2013.
- [16] Christophe Caloz, Andrea Alu, Sergei Tretyakov, Dimitrios Sounas, Karim Achouri, and Zoé-Lise Deck-Léger. Electromagnetic nonreciprocity. *Physical Review Applied*, 10(4):047001, 2018.
- [17] Mário G Silveirinha. Time-reversal symmetry in antenna theory. *Symmetry*, 11(4):486, 2019.
- [18] Anatoliĭ Konstantinovich Zvezdin and Viacheslav Alekseevich Kotov. *Modern magneto-optics and magneto-optical materials*. CRC Press, 1997.
- [19] David M Pozar. *Microwave engineering*. John wiley & sons, 2011.
- [20] Enze Zhang, Xian Xu, Yi-Chao Zou, Linfeng Ai, Xiang Dong, Ce Huang, Pengliang Leng, Shanshan Liu, Yuda Zhang, Zehao Jia, et al. Nonreciprocal superconducting nbse2 antenna. *Nature communications*, 11(1):5634, 2020.
- [21] Ala Eldin Omer, Afsaneh Hojjati-Firoozabadi, Suren Gigoyan, Safieddin Safavi-Naeini, and George Shaker. Non-reciprocal whispering-gallery-mode resonator for sensitive blood glucose monitoring. *IEEE Transactions on Instrumentation and Measurement*, 71:1–12, 2022.
- [22] Weijia Yang, Peter G Kazansky, and Yuri P Svirko. Non-reciprocal ultrafast laser writing. *Nature Photonics*, 2(2):99–104, 2008.
- [23] R Sumukh Nandan, Shailesh Srivastava, and R Gowrishankar. Non-reciprocal biasing for performance enhancement of the resonant fiber gyroscope with ‘reflector’ using in-line faraday rotators: Design, analysis and characterization. *Optical Fiber Technology*, 53:102038, 2019.
- [24] Yuefeng Qi, Xin Zhang, Yantao Wang, Mingjun Wang, Zimeng Liu, Chenbo Gong, and Yanyan Liu. Application of a novel spatial non-reciprocal phase modulator in fiber optic gyroscope. *Optical Fiber Technology*, 58:102258, 2020.
- [25] Charles A Downing and David Zueco. Non-reciprocal population dynamics in a quantum trimer. *Proceedings of the Royal Society A*, 477(2255):20210507, 2021.
- [26] Amarendra K Sarma and Sampreet Kalita. Tutorial: Cavity quantum optomechanics. *arXiv preprint arXiv:2211.02596*, 2022.
- [27] Markus Aspelmeyer, Tobias J Kippenberg, and Florian Marquardt. Cavity optomechanics. *Reviews of Modern Physics*, 86(4):1391, 2014.
- [28] C. W. Gardiner and M. J. Collett. Input and output in damped quantum systems: Quantum stochastic differential equations and the master equation. *Physical Review A*, 31:3761–3774, 1985.

- [29] Freek Ruesink, Mohammad-Ali Miri, Andrea Alù, and Ewold Verhagen. Nonreciprocity and magnetic-free isolation based on optomechanical interactions. *Nature Communications*, 7:13662, 2016.
- [30] J. Rao, C. Yu, Y. Zhao, Y-S. Gui, X. Fan, D. Xue, and C-M. Hu. Level attraction and level repulsion of magnon coupled with a cavity anti-resonance. *New Journal of Physics*, 2019.
- [31] Somayyeh Belbasi, M Ebrahim Foulaadvand, and Yong S Joe. Anti-resonance in a one-dimensional chain of driven coupled oscillators. *American Journal of Physics*, 82(1):32–38, 2014.
- [32] S J M. Habraken, K. Stannigel, M D. Lukin, P. Zoller, and P Rabl. Continuous mode cooling and phonon routers for phononic quantum networks. *New Journal of Physics*, 14:115004, 2012.
- [33] Martino De Carlo, Francesco De Leonardis, Richard A Soref, Luigi Colatorti, and Vittorio MN Passaro. Non-hermitian sensing in photonics and electronics: A review. *Sensors*, 22(11):3977, 2022.
- [34] Wenkui Ding, Xiaoguang Wang, and Shu Chen. Fundamental sensitivity limits for non-hermitian quantum sensors. *arXiv preprint arXiv:2304.08374*, 2023.
- [35] Yaoming Chu, Yu Liu, Haibin Liu, and Jianming Cai. Quantum sensing with a single-qubit pseudo-hermitian system. *Physical Review Letters*, 124(2):020501, 2020.
- [36] Florian Koch and Jan Carl Budich. Quantum non-hermitian topological sensors. *Physical Review Research*, 4(1):013113, 2022.
- [37] Jan Wiersig. Review of exceptional point-based sensors. *Photonics Research*, 8(9):1457–1467, 2020.
- [38] Jan Wiersig. Sensors operating at exceptional points: General theory. *Physical review A*, 93(3):033809, 2016.
- [39] Bo Peng, Şahin Kaya Özdemir, Fuchuan Lei, Faraz Monifi, Mariagiovanna Gianfreda, Gui Lu Long, Shanhui Fan, Franco Nori, Carl M Bender, and Lan Yang. Parity–time-symmetric whispering-gallery microcavities. *Nature Physics*, 10(5):394–398, 2014.
- [40] Mohammad-Ali Miri and Andrea Alù. Exceptional points in optics and photonics. *Science*, 363(6422):eaar7709, 2019.
- [41] Şahin Kaya Özdemir, Stefan Rotter, Franco Nori, and L Yang. Parity–time symmetry and exceptional points in photonics. *Nature Materials*, 18(8):783–798, 2019.
- [42] Hossein Hodaei, Absar U Hassan, Steffen Wittek, Hipolito Garcia-Gracia, Ramy El-Ganainy, Demetrios N Christodoulides, and Mercedeh Khajavikhan. Enhanced sensitivity at higher-order exceptional points. *Nature*, 548(7666):187–191, 2017.

- [43] M Naghiloo, M Abbasi, Yogesh N Joglekar, and KW Murch. Quantum state tomography across the exceptional point in a single dissipative qubit. *Nature Physics*, 15(12):1232–1236, 2019.
- [44] Aashish A. McDonald, Alexander; Clerk. Exponentially-enhanced quantum sensing with non-hermitian lattice dynamics. *Nature Communications*, 11:5382, 2020.
- [45] Qi Zhong. *Physics and applications of exceptional points*. PhD thesis, Michigan Technological University, 2019.
- [46] Weijian Chen, Şahin Kaya Özdemir, Guangming Zhao, Jan Wiersig, and Lan Yang. Exceptional points enhance sensing in an optical microcavity. *Nature*, 548(7666):192–196, 2017.
- [47] Han Zhao, Zhaowei Chen, Ruogang Zhao, and Liang Feng. Exceptional point engineered glass slide for microscopic thermal mapping. *Nature communications*, 9(1):1764, 2018.
- [48] Maryam Sakhdari, Mehdi Hajizadegan, Yue Li, Mark Ming-Cheng Cheng, Jonathan CH Hung, and Pai-Yen Chen. Ultrasensitive, parity–time-symmetric wireless reactive and resistive sensors. *IEEE Sensors Journal*, 18(23):9548–9555, 2018.
- [49] Pai-Yen Chen, Maryam Sakhdari, Mehdi Hajizadegan, Qingsong Cui, Mark Ming-Cheng Cheng, Ramy El-Ganainy, and Andrea Alù. Generalized parity–time symmetry condition for enhanced sensor telemetry. *Nature Electronics*, 1(5):297–304, 2018.
- [50] Zhenya Dong, Zhipeng Li, Fengyuan Yang, Cheng-Wei Qiu, and John S Ho. Sensitive readout of implantable microsensors using a wireless system locked to an exceptional point. *Nature Electronics*, 2(8):335–342, 2019.
- [51] Chao Zeng, Yong Sun, Guo Li, Yunhui Li, Haitao Jiang, Yaping Yang, and Hong Chen. Enhanced sensitivity at high-order exceptional points in a passive wireless sensing system. *Optics express*, 27(20):27562–27572, 2019.
- [52] Mohammad P Hokmabadi, Alexander Schumer, Demetrios N Christodoulides, and Mercedeh Khajavikhan. Non-hermitian ring laser gyroscopes with enhanced sagnac sensitivity. *Nature*, 576(7785):70–74, 2019.
- [53] Yu-Hung Lai, Yu-Kun Lu, Myoung-Gyun Suh, Zhiquan Yuan, and Kerry Vahala. Observation of the exceptional-point-enhanced sagnac effect. *Nature*, 576(7785):65–69, 2019.
- [54] Hoi-Kwan Lau and Aashish A Clerk. Fundamental limits and non-reciprocal approaches in non-hermitian quantum sensing. *Nature Communications*, 9(1):4320, 2018.
- [55] Chong Chen, Liang Jin, and Ren-Bao Liu. Sensitivity of parameter estimation near the exceptional point of a non-hermitian system. *New Journal of Physics*, 21(8):083002, 2019.

- [56] Mengzhen Zhang, William Sweeney, Chia Wei Hsu, Lan Yang, AD Stone, and Liang Jiang. Quantum noise theory of exceptional point amplifying sensors. *Physical Review Letters*, 123(18):180501, 2019.
- [57] Matteo GA Paris. Quantum estimation for quantum technology. *International Journal of Quantum Information*, 7(supp01):125–137, 2009.
- [58] Samuel L Braunstein and Carlton M Caves. Statistical distance and the geometry of quantum states. *Physical Review Letters*, 72(22):3439, 1994.
- [59] Jing Liu, Haidong Yuan, Xiao-Ming Lu, and Xiaoguang Wang. Quantum fisher information matrix and multiparameter estimation. *Journal of Physics A: Mathematical and Theoretical*, 53(2):023001, 2020.
- [60] Jing Liu, Heng-Na Xiong, Fei Song, and Xiaoguang Wang. Fidelity susceptibility and quantum fisher information for density operators with arbitrary ranks. *Physica A: Statistical Mechanics and its Applications*, 410:167–173, 2014.
- [61] Carl W. Helstrom (Eds.). *Quantum Detection and Estimation Theory*. Mathematics in Science and Engineering 123. Elsevier, Academic Press, 1976.
- [62] Zhicheng Xiao, Huanan Li, Tsampikos Kottos, and Andrea Alù. Enhanced sensing and nondegraded thermal noise performance based on p t-symmetric electronic circuits with a sixth-order exceptional point. *Physical Review Letters*, 123(21):213901, 2019.
- [63] W. Langbein. No exceptional precision of exceptional-point sensors. *Physical Review A*, 98:023805, 2018.
- [64] Tosio Kato. *Perturbation theory for linear operators*, volume 132. Springer Science & Business Media, 2013.
- [65] Alexei A. Mailybaev Alexander P. SeyraFnian. *Multiparameter Stability Theory with Mechanical Applications*. Series on Stability, Vibration and Control of Systems, Series a Vol. 13. World Scientific Publishing Company, 2004.
- [66] Guo-Qing Qin, Ran-Ran Xie, Hao Zhang, Yun-Qi Hu, Min Wang, Gui-Qin Li, Haitan Xu, Fuchuan Lei, Dong Ruan, and Gui-Lu Long. Experimental realization of sensitivity enhancement and suppression with exceptional surfaces. *Laser & Photonics Reviews*, 15(5):2000569, 2021.
- [67] Jun-Hee Park, Abdoulaye Ndao, Wei Cai, Liyi Hsu, Ashok Kodigala, Thomas Lepetit, Yu-Hwa Lo, and Boubacar Kanté. Symmetry-breaking-induced plasmonic exceptional points and nanoscale sensing. *Nature Physics*, 16(4):462–468, 2020.
- [68] Zhipeng Li, Chenhui Li, Ze Xiong, Guoqiang Xu, Yongtai Raymond Wang, Xi Tian, Xin Yang, Zhu Liu, Qihang Zeng, Rongzhou Lin, et al. Stochastic exceptional points for noise-assisted sensing. *Physical Review Letters*, 130(22):227201, 2023.

- [69] Q Zhong, Jinhan Ren, Mercedeh Khajavikhan, Demetrios N Christodoulides, ŞK Özdemir, and Ramy El-Ganainy. Sensing with exceptional surfaces in order to combine sensitivity with robustness. *Physical review letters*, 122(15):153902, 2019.
- [70] Wenxiu Li, Hao Zhang, Peng Han, Xiaoyang Chang, Shuo Jiang, Yang Zhou, Anping Huang, and Zhisong Xiao. Real frequency splitting indirectly coupled anti-parity-time symmetric nanoparticle sensor. *Journal of Applied Physics*, 128(13):134503, 2020.
- [71] Huilai Zhang, Ran Huang, Sheng-Dian Zhang, Ying Li, Cheng-Wei Qiu, Franco Nori, and Hui Jing. Breaking anti-pt symmetry by spinning a resonator. *Nano Letters*, 20(10):7594–7599, 2020.
- [72] P Djorwe, Yan Pennec, and Bahram Djafari-Rouhani. Exceptional point enhances sensitivity of optomechanical mass sensors. *Physical Review Applied*, 12(2):024002, 2019.
- [73] C. Caloz, A. Alu, S. Tretyakov, D. Sounas, K. Achouri, and Z.L.Deck-Leger. Electromagnetic nonreciprocity. *Physical Review Applied*, 10:047001, 2018.
- [74] D. Jalas, A. Petrov, M. Eich, W. Freude, S. Fan, Z. Yu, R. Baets, M. Popović, A. Melloni, J. D. Joannopoulos, M. Vanwolleghem, C. R. Doerr, and H. Renner. What is — and what is not — an optical isolator. *Nature Photonics*, 7:579–582, 2013.
- [75] Bahaa E. A. Saleh and Malvin Carl Teich. *Fundamentals of photonics*. Wiley Series in Pure and Applied Optics. WILEY, 2ed., wiley edition, 2007.
- [76] Michael Fleischhauer, Atac Imamoglu, and Jonathan. P. Marangos. Electromagnetically induced transparency: Optics in coherent media. *Review of Modern Physics*, 77:633–673, 2005.
- [77] C. L. Garrido Alzar, M. A. G. Martinez, and P. Nussenzveig. Classical analog of electromagnetically induced transparency. *American Journal of Physics*, 70:37, 2002.
- [78] Hao Xiong and Ying Wu. Fundamentals and applications of optomechanically induced transparency. *Applied Physics Reviews*, 5:031305, 2018.
- [79] A. M. Akulshin, S. Barreiro, and A. Lezama. Electromagnetically induced absorption and transparency due to resonant two-field excitation of quasidegenerate levels in rb vapor. *Physical Review A*, 57:2996–3002, 1998.
- [80] A. M. Lezama, S. Barreiro, and A. M. Akulshin. Electromagnetically induced absorption. *Physical Review A*, 59:4732–4735, 1999.
- [81] A. V. Taichenachev, A. M. Tumaikin, and V. I. Yudin. Electromagnetically induced absorption in a four-state system. *Physical Review A*, 61:011802(R), 1999.
- [82] A. H. Safavi-Naeini, T. P. Mayer Alegre, J. Chan, M. Eichenfield, M. Winger, Q. Lin, J. T. Hill, D. E. Chang, and O. Painter. Electromagnetically induced transparency and slow light with optomechanics. *Nature*, 472:69–73, 2011.

- [83] Kenan Qu and G. S. Agarwal. Phonon-mediated electromagnetically induced absorption in hybrid opto-electromechanical systems. *Physical Review A*, 87(3):031802(R), 2013.
- [84] Fredrik Hocke, Xiaoqing Zhou, Albert Schliesser, Tobias J Kippenberg, Hans Huebl, and Rudolf Gross. Electromechanically induced absorption in a circuit nano-electromechanical system. *New Journal of Physics*, 14(12):123037, 2012.
- [85] V. Singh, S. J. Bosman, B. H. Schneider, Y. M. Blanter, A. Castellanos-Gomez, and G. A. Steele. Optomechanical coupling between a multilayer graphene mechanical resonator and a superconducting microwave cavity. *Nature Nanotechnology*, 9:820–824, 2014.
- [86] W. Z. Jia, L. F. Wei, Yong Li, and Y. X. Liu. Phase-dependent optical response properties in an optomechanical system by coherently driving the mechanical resonator. *Physical Review A*, 91:043843, 2015.
- [87] Gang Wang, Yu-Sheng Wang, Emily Kay Huang, Weilun Hung, Kai-Lin Chao, Ping-Yeh Wu, Yi-Hsin Chen, and Ite A. Yu. Ultranarrow-bandwidth filter based on a thermal eit medium. *Scientific Reports*, 8:7959, 2018.
- [88] Siva Shakthi A., Anjali B. Yelkar, and Ravi Pant. Analogue of electromagnetically induced absorption in the microwave domain using stimulated brillouin scattering. *Communications Physics*, 3:109, 2020.
- [89] Fredrik Hocke, Xiaoqing Zhou, Albert Schliesser, Tobias J Kippenberg, Hans Huebl, and Rudolf Gross. Electromechanically induced absorption in a circuit nano-electromechanical system. *New Journal of Physics*, 14:123037, 2012.
- [90] S. Rajasekar and M. A. F. Sanjuán. *Nonlinear Resonances, Chap. 14*. Springer series in synergetics.; Springer complexity. Springer, 1st ed. edition, 2016.
- [91] Ewold Verhagen and Andrea Alù. Optomechanical nonreciprocity. *Nature Physics*, 13:922–924, 2017.
- [92] A. Metelmann and A.A. Clerk. Nonreciprocal photon transmission and amplification via reservoir engineering. *Physical Review X*, 5:021025, 2015.
- [93] M-A. Miri, F. Ruesink, E. Verhagen, and A. Alù. Optical nonreciprocity based on optomechanical coupling. *Physical Review Applied*, 7:064014, 2017.
- [94] David M. Pozar. *Microwave Engineering*, pages 272–277. John Wiley and Sons. Inc, 4th edition, 2012.
- [95] J. D. Thompson, B. M. Zwickl, A. M. Jayich, Florian Marquardt, S. M. Girvin, and J. G. E. Harris. Strong dispersive coupling of a high-finesse cavity to a micromechanical membrane. *Nature*, 452:72–75, 2008.

- [96] Luca Dellantonio, Oleksandr Kyriienko, Florian Marquardt, and Anders S. Sørensen. Quantum nondemolition measurement of mechanical motion quanta. *Nature Communications*, 9:3621, 2018.
- [97] Guolong Li, Xiao Xiao, Yong Li, and Xiaoguang Wang. Tunable optical nonreciprocity and a phonon-photon router in an optomechanical system with coupled mechanical and optical modes. *Physical Review A*, 97:023801, 2018.
- [98] Mohammad Hafezi and Peter Rabl. Optomechanically induced non-reciprocity in microring resonators. *Optics Express*, 20:7672, 2012.
- [99] M. Schmidt, S. Kessler, V. Peano, O. Painter, and F. Marquardt. Optomechanical creation of magnetic fields for photons on a lattice. *Optica*, 2:635, 2015.
- [100] Xun-Wei Xu, Yong Li, Ai-Xi Chen, and Yu-xi Liu. Nonreciprocal conversion between microwave and optical photons in electro-optomechanical systems. *Physical Review A*, 93:023827, 2016.
- [101] A. Metelmann and A. A. Clerk. Nonreciprocal quantum interactions and devices via autonomous feedforward. *Physical Review A*, 95:013837, 2017.
- [102] Lin Tian and Zhen Li. Nonreciprocal quantum-state conversion between microwave and optical photons. *Physical Review A*, 96:013808, 2017.
- [103] Zhen Shen, Yan-Lei Zhang, Yuan Chen, Chang-Ling Zou, Yun-Feng Xiao, Xu-Bo Zou, Fang-Wen Sun, Guang-Can Guo, and Chun-Hua Dong. Experimental realization of optomechanically induced non-reciprocity. *Nature Photonics*, 2016.
- [104] Zhen Shen, Yan-Lei Zhang, Yuan Chen, Fang-Wen Sun, Xu-Bo Zou, Guang-Can Guo, Chang-Ling Zou, and Chun-Hua Dong. Reconfigurable optomechanical circulator and directional amplifier. *Nature Communications*, 9:1797, 2018.
- [105] Freek Ruesink, John P. Mathew, Mohammad-Ali Miri, Andrea Alu, and Ewold Verhagen. Optical circulation in a multimode optomechanical resonator. *Nature Communications*, 9:1798, 2018.
- [106] K. Fang, J. Luo, A. Metelmann, Matthew H. Matheny, F. Marquardt, A. A. Clerk, and O. Painter. Generalized non-reciprocity in an optomechanical circuit via synthetic magnetism and reservoir engineering. *Nature Physics*, 2017.
- [107] N. R. Bernier, L. D. Tóth, A. Koottandavida, M. A. Ioannou, D. Malz, A. Nunnenkamp, A. K. Feofanov, and T. J. Kippenberg. Nonreciprocal reconfigurable microwave optomechanical circuit. *Nature Communications*, 8:604, 2017.
- [108] G. A. Peterson, F. Lecocq, K. Cicak, R. W. Simmonds, J. Aumentado, and J. D. Teufel. Demonstration of efficient nonreciprocity in a microwave optomechanical circuit. *Physical Review X*, 7:031001, 2017.
- [109] S. Barzanjeh, M. Wulf, M. Peruzzo, M. Kalaei, P. B. Dieterle, O. Painter, and J. M. Fink. Mechanical on-chip microwave circulator. *Nature Communications*, 8:953, 2017.

- [110] J. C. Sankey, C. Yang, B. M. Zwickl, A. M. Jayich, and J. G. E. Harris. Strong and tunable nonlinear optomechanical coupling in a low-loss system. *Nature Physics*, 6:707–712, 2010.
- [111] Sumei Huang and G. S. Agarwal. Electromagnetically induced transparency from two-phonon processes in quadratically coupled membranes. *Phys. Rev. A*, 83:023823, Feb 2011.
- [112] M. Bhattacharya, H. Uys, and P. Meystre. Optomechanical trapping and cooling of partially reflective mirrors. *Phys. Rev. A*, 77:033819, Mar 2008.
- [113] A M Jayich, J C Sankey, B M Zwickl, C Yang, J D Thompson, S M Girvin, A. A. Clerk, F Marquardt, and J G E Harris. Dispersive optomechanics: a membrane inside a cavity. *New Journal of Physics*, 10:095008, 2008.
- [114] B. D. Hauer, A. Metelmann, and J. P. Davis. Phonon quantum nondemolition measurements in nonlinearly coupled optomechanical cavities. *Physical Review A*, 98:043804, 2018.
- [115] Florian Marquardt, Joe P. Chen, A. A. Clerk, and S. M. Girvin. Quantum theory of cavity-assisted sideband cooling of mechanical motion. *Physical Review Letters*, 99:093902, 2007.
- [116] Ryuichi Ohta, Loïc Herpin, Victor M Bastidas, Takehiko Tawara, Hiroshi Yamaguchi, and Hajime Okamoto. Rare-earth-mediated optomechanical system in the reversed dissipation regime. *Physical Review Letters*, 126(4):047404, 2021.
- [117] Laszlo Daniel Toth, Nathan Rafaël Bernier, Andreas Nunnenkamp, AK Feofanov, and TJ Kippenberg. A dissipative quantum reservoir for microwave light using a mechanical oscillator. *Nature Physics*, 13(8):787–793, 2017.
- [118] A. Nunnenkamp, V. Sudhir, A. K. Feofanov, A. Roulet, and T. J. Kippenberg. Quantum-limited amplification and parametric instability in the reversed dissipation regime of cavity optomechanics. *Phys. Rev. Lett.*, 113:023604, Jul 2014.
- [119] Jae Hoon Lee and H. Seok. Quantum reservoir engineering through quadratic optomechanical interaction in the reversed dissipation regime. *Physical Review A*, 97:013805, 2018.
- [120] Linran. Fan, King Y. Fong, Menno. Poot, and Hong X. Tang. Cascaded optical transparency in multimode-cavity optomechanical systems. *Nature Communications*, 6:5850, 2015.
- [121] D. Bothner, S. Yanai, A. Iniguez-Rabago, M. Yuan, Ya. M. Blanter, and G. A. Steele. Cavity electromechanics with parametric mechanical driving. *Nature Communications*, 11:1589, 2020.
- [122] Joerg Bochmann, Amit Vainsencher, David D Awschalom, and Andrew N Cleland. Nanomechanical coupling between microwave and optical photons. *Nature Physics*, 9(11):712–716, 2013.

- [123] Aaron D O’Connell, Max Hofheinz, Markus Ansmann, Radoslaw C Bialczak, Mike Lenander, Erik Lucero, Matthew Neeley, Daniel Sank, H Wang, Ms Weides, et al. Quantum ground state and single-phonon control of a mechanical resonator. *Nature*, 464(7289):697–703, 2010.
- [124] Hajime Okamoto, Adrien Gourgout, Chia-Yuan Chang, Koji Onomitsu, Imran Mahboob, Edward Yi Chang, and Hiroshi Yamaguchi. Coherent phonon manipulation in coupled mechanical resonators. *Nature Physics*, 9:598–598, 2013.
- [125] T. Faust, J. Rieger, M. J. Seitner, J. P. Kotthaus, and E. M. Weig. Coherent control of a classical nanomechanical two-level system. *Nature Physics*, 9:485–488, 2013.
- [126] Hao Fu, Zhi-cheng Gong, Tian-hua Mao, Chang-pu Sun, Su Yi, Yong Li, and Geng-yu Cao. Classical analog of Stückelberg interferometry in a two-coupled-cantilever-based optomechanical system. *Physical Review A*, 94:043855, 2016.
- [127] Y. Li, Y. Y. Huang, X. Z. Zhang, and L. Tian. Optical directional amplification in a three-mode optomechanical system. *Optics Express*, 25:18907, 2017.
- [128] Jinyong Ma, Cai You, Liu-Gang Si, Hao Xiong, Jiahua Li, Xiaoxue Yang, and Ying Wu. Optomechanically induced transparency in the presence of an external time-harmonic-driving force. *Scientific Reports*, 5:11278, 2015.
- [129] Xun-Wei Xu and Yong Li. Controllable optical output fields from an optomechanical system with mechanical driving. *Physical Review A*, 92:023855, 2015.
- [130] Kexun Yan, Yongchao Zhang, Yuanshun Cui, and Cheng Jiang. Controllable optical response in a quadratically coupled optomechanical system with mechanical driving. *Optics Communications*, 475:126249, 2020.
- [131] Liu-Gang Si, Hao Xiong, M. Suhail Zubairy, and Ying Wu. Optomechanically induced opacity and amplification in a quadratically coupled optomechanical system. *Physical Review A*, 95:033803, 2017.
- [132] Shaopeng Liu, Wen-Xing Yang, Tao Shui, Zhonghu Zhu, and Ai-Xi Chen. Tunable two-phonon higher-order sideband amplification in a quadratically coupled optomechanical system. *Scientific Reports*, 7:17637, 2017.
- [133] Yu-Ming Xiao, Jun-Hao Liu, Qin Wu, Ya-Fei Yu, and Zhi-Ming Zhang. Optical non-reciprocity in a piezo-optomechanical system. *Chinese Physics B*, 2020.
- [134] Hefeng Wang, S. Ashhab, and Franco Nori. Quantum algorithm for simulating the dynamics of an open quantum system. *Phys. Rev. A*, 83:062317, Jun 2011.
- [135] Shi-Jie Wei, Dong Ruan, and Gui-Lu Long. Duality quantum algorithm efficiently simulates open quantum systems. *Scientific Reports*, 6(1):30727, 2016.
- [136] Chao Zheng. Universal quantum simulation of single-qubit nonunitary operators using duality quantum algorithm. *Scientific Reports*, 11(1):3960, 2021.

- [137] Seth Lloyd. Universal quantum simulators. *Science*, 273(5278):1073–1078, 1996.
- [138] Nishanth Baskaran, Abhishek Singh Rawat, Dibyajyoti Chakravarti, Akshaya Jayashankar, K Sugisaki, D Mukherjee, and VS Prasanna. Adapting the hhl algorithm to near-term quantum computing: application to non-unitary quantum many-body theory. *arXiv preprint arXiv:2212.14781*, 2022.
- [139] Hamza Jnane, Nicolas P. D. Sawaya, Borja Peropadre, Alan Aspuru-Guzik, Raul Garcia-Patron, and Joonsuk Huh. Analog quantum simulation of non-Condon effects in molecular spectroscopy. *ACS Photonics*, 8:7, 2021.
- [140] Francesco Benfenati, Guglielmo Mazzola, Chiara Capecchi, Panagiotis Kl Barkoutsos, Pauline J Ollitrault, Ivano Tavernelli, and Leonardo Guidoni. Improved accuracy on noisy devices by nonunitary variational quantum eigensolver for chemistry applications. *Journal of Chemical Theory and Computation*, 17(7):3946–3954, 2021.
- [141] Daniel S Abrams and Seth Lloyd. Nonlinear quantum mechanics implies polynomial-time solution for np-complete and # p problems. *Physical Review Letters*, 81(18):3992, 1998.
- [142] Shu Xu, Jörg Schmiedmayer, and Barry C Sanders. Nonlinear quantum gates for a bose-einstein condensate. *Physical Review Research*, 4(2):023071, 2022.
- [143] Iris Cong, Soonwon Choi, and Mikhail D Lukin. Quantum convolutional neural networks. *Nature Physics*, 15(12):1273–1278, 2019.
- [144] Kerstin Beer, Daniel List, Gabriel Müller, Tobias J Osborne, and Christian Struckmann. Training quantum neural networks on nisc devices. *arXiv preprint arXiv:2104.06081*, 2021.
- [145] Kaitlin Gili, Mykolas Sveistrys, and Chris Ballance. Introducing nonlinear activations into quantum generative models. *Physical Review A*, 107(1):012406, 2023.
- [146] Maria Schuld, Ilya Sinayskiy, and Francesco Petruccione. The quest for a quantum neural network. *Quantum Information Processing*, 13:2567–2586, 2014.
- [147] Carl M Bender and Stefan Boettcher. Real spectra in non-hermitian hamiltonians having p t symmetry. *Physical Review Letters*, 80(24):5243, 1998.
- [148] Dorje C Brody and Eva-Maria Graefe. Information geometry of complex hamiltonians and exceptional points. *Entropy*, 15(9):3361–3378, 2013.
- [149] Géza Tóth and Florian Fröwis. Uncertainty relations with the variance and the quantum fisher information based on convex decompositions of density matrices. *Physical Review Research*, 4(1):013075, 2022.
- [150] Shunlong Luo. Quantum fisher information and uncertainty relations. *Letters in Mathematical Physics*, 53:243–251, 2000.

- [151] Robert Duggan, Sander A Mann, and Andrea Alu. Limitations of sensing at an exceptional point. *ACS Photonics*, 9(5):1554–1566, 2022.
- [152] Liangyu Ding, Kaiye Shi, Qiuxin Zhang, Danna Shen, Xiang Zhang, and Wei Zhang. Experimental determination of p t-symmetric exceptional points in a single trapped ion. *Physical Review Letters*, 126(8):083604, 2021.
- [153] Hiroaki Terashima and Masahito Ueda. Nonunitary quantum circuit. *International Journal of Quantum Information*, 3(04):633–647, 2005.
- [154] Harry Buhrman, Richard Cleve, John Watrous, and Ronald De Wolf. Quantum fingerprinting. *Physical Review Letters*, 87(16):167902, 2001.
- [155] IBM. Qiskit textbook. <https://qiskit.org/learn/>.
- [156] Qiskit documentation for state_vector simulator. https://qiskit.org/documentation/stubs/qiskit_aer.StatevectorSimulator.html. Accessed: 2023-03-27.
- [157] Daniël; Waalkens Holger Pap, Eric J.; Boer. Non-abelian nature of systems with multiple exceptional points. *Physical Review A*, 98:023818, 2018.
- [158] Jung-Wan; Kim Sang Wook; Chung Yunchul Lee, Soo-Young; Ryu. Geometric phase around multiple exceptional points. *Physical Review A*, 85, 2012.
- [159] Guancong; Xiao-Meng; Zhang Z.Q.; Chan C.T. Ding, Kun; Ma. Emergence, coalescence, and topological properties of multiple exceptional points and their experimental realization. *Physical Review X*, 6:021007, 2016.
- [160] Heinz-Peter Breuer and Francesco Petruccione. *The theory of open quantum systems*. Oxford University Press, USA, 2002.
- [161] Daniel Manzano. A short introduction to the lindblad master equation. *Aip Advances*, 10(2), 2020.
- [162] Jean Dalibard, Yvan Castin, and Klaus Mølmer. Wave-function approach to dissipative processes in quantum optics. *Physical review letters*, 68(5):580, 1992.
- [163] Klaus Mølmer, Yvan Castin, and Jean Dalibard. Monte carlo wave-function method in quantum optics. *JOSA B*, 10(3):524–538, 1993.
- [164] Fabrizio Minganti, Adam Miranowicz, Ravindra W Chhajlany, Ievgen I Arkhipov, and Franco Nori. Hybrid-liouvillian formalism connecting exceptional points of non-hermitian hamiltonians and liouvillians via postselection of quantum trajectories. *Physical Review A*, 101(6):062112, 2020.
- [165] Yu-Xin Wang and AA Clerk. Non-hermitian dynamics without dissipation in quantum systems. *Physical Review A*, 99(6):063834, 2019.

- [166] Lewis Wright, Fergus Barratt, James Dborin, George H Booth, and Andrew G Green. Automatic post-selection by ancillae thermalization. *Physical Review Research*, 3(3):033151, 2021.
- [167] Elias Zapusek, Alisa Javadi, and Florentin Reiter. Nonunitary gate operations by dissipation engineering. *Quantum Science and Technology*, 8(1):015001, 2022.
- [168] Gaurav Nirala, Surya Narayan Sahoo, Arun K Pati, and Urbasi Sinha. Measuring average of non-hermitian operator with weak value in a mach-zehnder interferometer. *Physical Review A*, 99(2):022111, 2019.
- [169] Yakir Aharonov, David Z Albert, and Lev Vaidman. How the result of a measurement of a component of the spin of a spin-1/2 particle can turn out to be 100. *Physical Review Letters*, 60(14):1351, 1988.
- [170] Saki Tanaka and Naoki Yamamoto. Information amplification via postselection: A parameter-estimation perspective. *Physical Review A*, 88(4):042116, 2013.
- [171] John E Gray and Allen D Parks. The post-selection probability current and its implications. In *Quantum Information and Computation VII*, volume 7342, pages 107–116. SPIE, 2009.
- [172] Alastair A Abbott, Ralph Silva, Julian Wechs, Nicolas Brunner, and Cyril Branciard. Anomalous weak values without post-selection. *Quantum*, 3:194, 2019.
- [173] Xue-Jia Yu, Zhiming Pan, Limei Xu, and Zi-Xiang Li. Non-hermitian strongly interacting dirac fermions: a quantum monte-carlo study. *arXiv preprint arXiv:2302.10115*, 2023.
- [174] Tomoya Hayata and Arata Yamamoto. Non-hermitian hubbard model without the sign problem. *Physical Review B*, 104(12):125102, 2021.